Concept Study of a High-Speed, Vertical Take-Off and Landing Aircraft

By

Christopher Eden Mesrobian

Thesis submitted to the faculty of the Virginia Polytechnic Institute and State University in partial fulfillment of the requirements for the degree of

Master of Science
In
Engineering Mechanics

Committee Members:

Dr. Demetri Telionis
Dr. Saad Ragab
Dr. Muhammad Hajj

June 12, 2009
Blacksburg, Virginia

Keywords: DiscRotor, VTOL, Circular Wing, Disc-Wing, Wind Tunnel, Velocity Measurements, Hover Tests

Concept Study of a High-Speed, Vertical Take-Off and Landing Aircraft

Christopher Eden Mesrobian

ABSTRACT

The purpose of the study was to evaluate the merits of the DiscRotor concept that combine the features of a retractable rotor system for vertical take-off and landing (VTOL) with an integral, circular wing for high-speed flight. Tests were conducted to generate basic aerodynamic characteristics of the DiscRotor in hover and in fixed-wing flight.

To assess the DiscRotor during hover, small scale tests were conducted on a 3ft diameter rotor without the presence of a fuselage. A "hover rig" was constructed capable of rotating the model rotor at speeds up to 3,500 RPM to reach tip speeds of 500fps. Thrust and torque generated by the rotating model were measured via a two-component load cell, and time averaged values were obtained for various speeds and pitch angles. It has been shown that the DiscRotor will perform well in hover. Ground Effects in hover were examined by simulating the ground with a movable, solid wall. The thrust was found to increase by 50% compared to the ground-independent case. Pressure distributions were measured on the ground and disc surfaces. Velocity measurements examined the flow field downstream of the rotor by traversing a seven hole velocity probe. A wake behind the rotor was shown to contract due to a low pressure region that develops downstream of the disc.

Wind tunnel experimentation was also performed to examine the fixed wing flight of the DiscRotor. These experiments were performed in the VA Tech 6'X6' Stability Tunnel. A model of the fuselage and a circular wing was fabricated based upon an initial sizing study completed by our partners at Boeing. Forces were directly measured via a six degree of freedom load cell, or balance, for free stream velocities up to 200fps. Reynolds numbers of 2 and 0.5 million have been investigated for multiple angles of attack. Low lift-to-drag ratios were found placing high power requirements for the DiscRotor during fixed-wing flight. By traversing a seven-hole velocity probe, velocities in a 2-D grid perpendicular to the flow were measured on the model. The strengths of shed vortices from the model were calculated. A method to improve fixed-wing performance was considered where two blades were extended from the disc. An increase of 0.17 in the C_L was measured due to the interaction between the disc and blades.

This research utilized a wide range of experiments, with the aim of generating basic aerodynamic characteristics of the DiscRotor. A substantial amount of quantitative data was collected that could not be included in this document. Results aided in the initial designs of this aircraft for the purpose of evaluating the merit of the DiscRotor concept.

TABLE OF CONTENTS

TABLE OF FIGURES

LIST OF TABLES

1. Background and Introduction

1-1: Motivation

There has never been an aircraft successfully created that has vertical takeoff and landing (VTOL) capability with the benefits of a high speed cruise of a fixed-wing aircraft. The application of such an aircraft can be applied to both military and civilian purposes. Much of the focus and funding of this research has been driven by military applications, specifically Combat Search and Rescue (CSAR) missions. A short description of these applications is given to provide the motivation and purpose for the current study.

The capability of VTOL comes at a price such as increased mechanical complexity, increased weight and the susceptibility of rotor and wing to exhibit various aeroelastic problems (Leishman). Despite its shortcomings, the VTOL capability is essential in some applications where high forward flight speeds would be desired.

1-1.1: Search and Rescue Missions

The search for and rescue of personnel in hostile territory, i.e. the Combat Search and Rescue mission (CSAR) is a vital military air mission. This mission requires rapid deployment, vertical takeoff and landing (VTOL) capability, long range, extended loiter and high maneuverability. Speed is crucial to the survival of the wounded and to undetected passage through enemy territory. The success of these CSAR missions is dependent upon the capabilities of aircraft.

The current CSAR platform, the UH-60 Blackhawk, has a mission cruise speed less than 150 knots (UH-60A Blackhawk). As a conventional helicopter, it has the speed-limiting and detectability issues of rotating blades, but has fairly benign hover downwash characteristics due to its relatively low disc-loading. These downwash characteristics allow personnel to operate underneath the aircraft during takeoff or landing; an essential for performing CSAR missions.

Mission speed may be increased and acoustic detectability reduced by configuring an advanced CSAR as a tiltrotor, like the V-22, which cruises at about 230 knots, due to the more efficient propulsion afforded by its tilting proprotors (Boeing V-22 Osprey Backgrounder). However, the

disc-loading of the tiltrotor is almost double that of a helicopter, reducing hover efficiency and resulting in increased downwash velocities that subtract from personnel rescue operations.

A speed capability of 400-500 knots combined with efficient hover and acceptable groundwash characteristics would be desirable in a future CSAR aircraft, where speed is crucial to the survival of wounded personnel. This speed range is presently beyond the capability of the conventional tiltrotor and the helicopter. Additionally, the noise and radar signature of aircraft that utilize rotor blades, limits the ability to remain undetected.

Thus, a new aircraft concept is required to enable the development of a superior high-speed CSAR aircraft having a low likelihood of detection and efficient helicopter-like hover capabilities. Such an aircraft would be designed to cruise without the use of rotors, yet would still be capable of efficiently taking off and landing vertically.

1-1.2: Emergency Response Applications

Both civilian and military rescue missions require rapid response to be successful. Aircraft used for rescue applications require VTOL capability to reach remote areas because landing strips are not available. Helicopters are the only current suitable aircraft for such operations, but are unable to reach high speeds. An aircraft with the ability to reach speeds twice as high as helicopters would reduce the response time of EMS personnel. A few minutes in response time can determine the difference between life and death during a stroke or heart attack.

A standard lift off time for an EMS response helicopter, such as the Dauphin N2, is seven minutes which does not include the transit time during flight. The cruising or maximum flight speed is usually between 120 and 160 knots. In rural areas, much more distance must be covered to reach patients and the response time depends more upon the aircraft's maximum speed. To increase the response time, the in-transit or flight time would have to be decreased by increasing aircraft speed.

1-2: Existing Aircraft

Conventional fixed-wing aircraft, such as a commercial jet, generate lift by forward movement of the entire aircraft. Wings fixed in relation to the fuselage generated the lifting force to achieve

flight. Commercial jets are characterized by high cruising speed and high efficiency in flight. For this reason, fixed-wing aircraft remain the most widely used aircraft to date.

Conventional rotary aircraft, such as helicopters, generated lift by rotating multiple blades connected to a central shaft turned by an engine. As the rotational speed increases the blades generated lift to achieve flight. To maneuver the helicopter, cyclic pitch is applied to the blades creating a component of the lift in the desired direction. Helicopters are considered the most efficient VTOL aircraft to date because of the relatively low disc loading.

Other than conventional fixed-wing and rotary aircraft, numerous concepts have been conceived dating back 40 to 50 years. Figure 1-1 depicts the various types of Vertical and Short Take-Off and Landing (VSTOL) aircraft which have been tested over the past 45 years. All were developed with the intention of going into production, but only the Harrier, Joint Strike Fighter (JSF) and V-22 Osprey have led to the operational aircraft.

Figure 1-1 has been nicknamed the "VSTOL Wheel of Mis-Fortune" for almost all of the concepts have failed due to one reason or another. Still, it successfully illustrates the breadth of VSTOL concepts which have been attempted over the years. The center of the circle depicts the Joint Strike Fighter (JSF) Program (under which the Lockheed Martin X-35 was developed). The inner most ring separates concepts by the methods used to power the aircraft. The second ring further separates the concepts by lifting mechanisms. For brevity, all the building knowledge behind all of the concepts depicted in Figure 1-1 is not elaborated upon in this document. For further information, interested readers are guided to the article by Michael Hirschberg, *An Overview of the History of Vertical and/or Short Take-Off and Landing (V/STOL) Aircraft*.

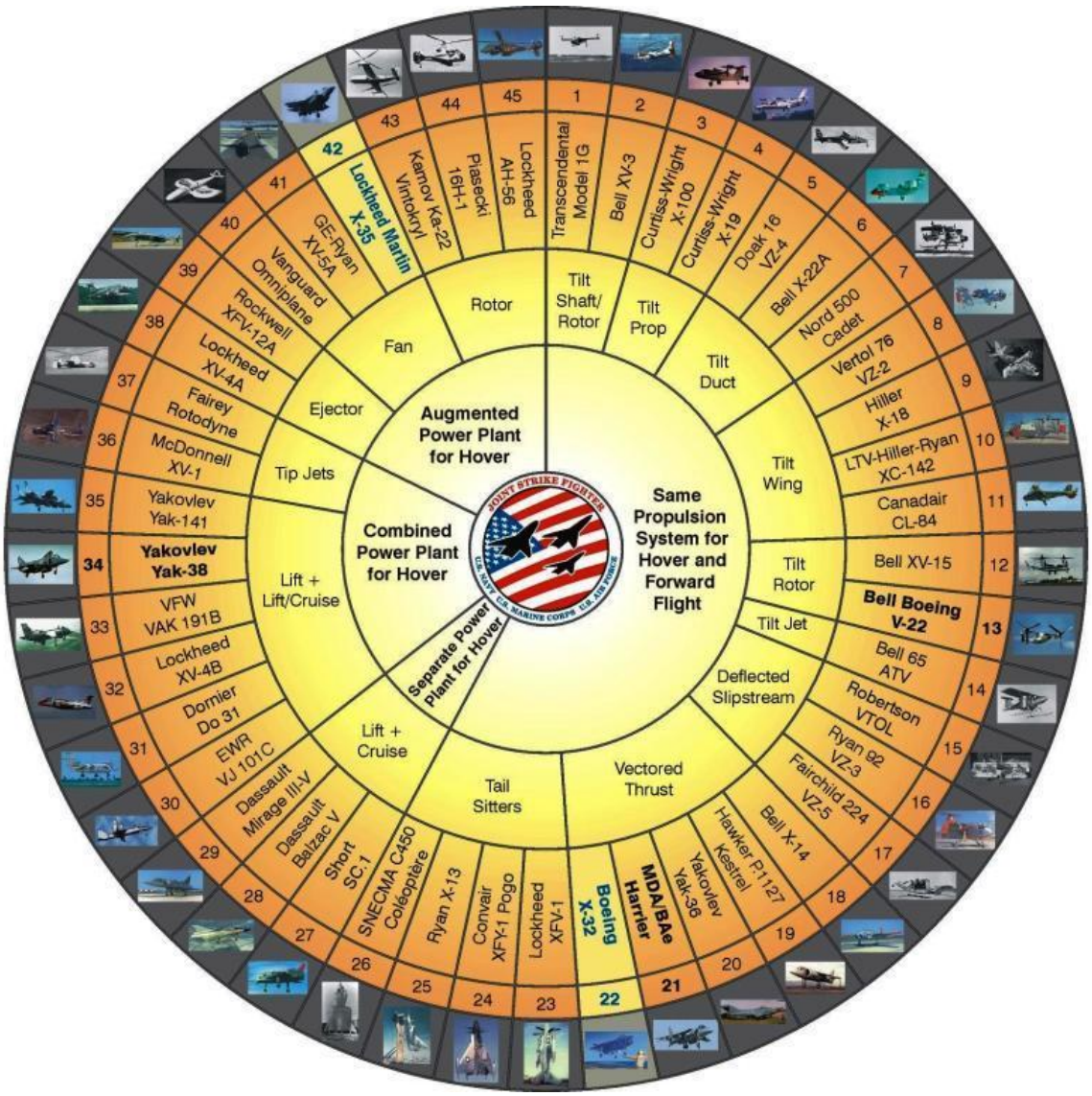

Figure 1-1: VSTOL Wheel of Mis-Fortune
VSTOL aircraft concepts tested over the past 45 years. (VSTOL Wheel of Mis-Fortune)

1-2.1: Tilt Rotor: Osprey v-22

The V-22 Osprey has the ability to take-off and land vertically with two rotors oriented vertically. As forward speed increases, the wing tip-mounted rotors are progressively titled to convert the aircraft into a configuration similar to a fixed-wing, turboprop airplane. Osprey combines the vertical takeoff, or hover, and landing capabilities of a helicopter with the forward speed of a fixed wing aircraft. The engines and propellers of the V-22 Osprey tilt up to form the rotors for vertical flight and tilt forward to create propulsion for fast forward flight (Leishman). These characteristics create the vertical performance of a helicopter with the speed and range of a fixed wing aircraft.

Figure 1-2: Photos of V-22 Osprey
From left to right, during hover (Espinoza) and high-speed flight (Darcy).

The practical uses of the Osprey include military applications. It can carry 24 combat troops, or up to 20,000 pounds of internal cargo or 15,000 pounds of external cargo, at twice the speed of a helicopter. The V-22 is the only vertical platform capable of rapid self-deployment to any theater of operation worldwide (V-22 Osprey Pocket Guide). Despite its many advantages, the V-22 Osprey is still limited in forward speed due to the tip-mounted rotors used for both hover and forward flight. For this reason, the tilt-rotor concept will always be limited in its maximum forward velocity.

1-2.2: M-85 Concept

In the mid 1980s, there was a revival of interest in rotorcraft concepts that combine helicopter attributes with high cruise speed capabilities. This interest has driven investigations into multiple aircraft concepts over the years. In the mid 1980s, there was much interest to develop low downwash, high speed rotorcraft concepts (Talbot, Phillips and Totah). A relevant concept to the

current study is the stopped rotor design (M-85) and was the subject of studies performed at NASA Ames Research Center.

The concept is shown in Figure 1-3 and was derived as an approach to enable smooth, stable conversion between fixed-wing and hover-flight modes, while retaining the hover and low-speed flight characteristics of a low disk loading helicopter. The name, M-85, reflects the high-speed goal of 0.85 Mach number at high altitude. Emphasis has been placed on an efficient high-speed cruise and then efficient hover. An initial analysis on the M-85 concept is reported in NASA Technical Memorandum 102871, *Introduction of the M-85 High-Speed Rotorcraft Concept* by Robert Stroub.

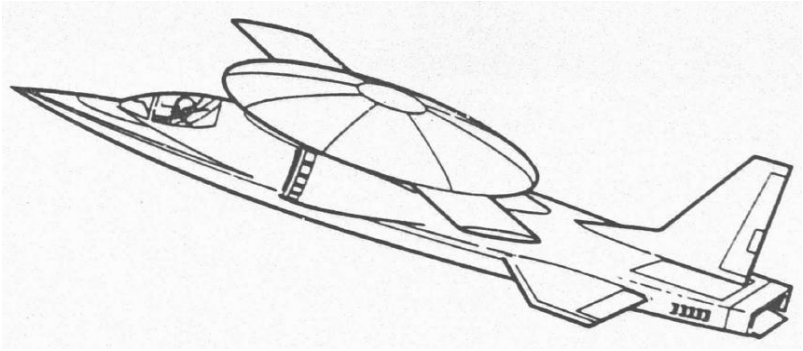

Figure 1-3: Stopped Rotor or M-85 Conceptual Drawing. (Swanson and Stroub)

The M-85 incorporated features such as:

- Generate lift by rotating a large-diameter hub fairing from which rotor blades would protrude for hover and vertical take-off.
- Create lift by stopping of hub fairing rotation for fixed-wing flight. Blades could be deployed from the disc during fixed-wing flight as shown in Figure 1-3.
- Ability to reverse the conversion process to change from fixed-wing to rotary-wing configuration for very low-speed flight and for hover and vertical landing.

The objective of an aircraft with quiet, efficient hover capability and an efficient high-speed cruise capability may be achievable with the M-85 high-speed rotorcraft concept.

1-2.2.1: M-85 Fixed Wing Results

A low-speed wind tunnel test was completed by Swanson and Stroub in support of the design study performed on the stopped rotor concept. The purpose of this test was to evaluate the fixed-wing aerodynamics and compare three different cruise configurations. The results are presented in paper AIAA-1992-1067-859. The most efficient flight, i.e. highest L/D ratio, was achieved by extending two rotor blades from the stopped disc. During testing, it was noted that the horizontal tail position with respect to the disc was inadequate and required further study. In short, only a limited number of geometric configurations were tested, and additional tests would be required for a full evaluation of the stopped rotor concept.

1-2.2.2: M-85 Hover Results

Hover characteristics are discussed in the NASA Technical Memorandum 102871 by Robert Stroub, *Introduction to the M-85 High-Speed Rotorcraft Concept*. It also discusses other technologies pertinent to the M-85 concept such as passively controlling in-plane vibration during starting and stopping of the rotor system, aircraft control system, and rotor drive technologies.

As stated in the report, hover power is expected to be no greater than 25% more than hover power for a conventional rotor. This 25% power increment was determined from small-scale model hover tests. A free-pitching blade control technique is presented as a method of producing sufficient pitch and roll moments about the aircraft center of gravity for aircraft control while inherently suppressing wake and gust-induced oscillatory vertical loads. (Stroub)

1-3: DiscRotor Concept

The DiscRotor aircraft has been proposed to meet the requirements for an advanced VTOL aircraft. Figure 1-4 is an artistic impression of the DiscRotor aircraft shown from the port side. This concept combines the payload-efficient features of rotor blades for vertical take-off and landing with an integral, circular, fixed-wing for high-speed flight. Propulsion is not yet defined but would most likely be provided by either a tail-mounted ducted propeller or side-mounted turbofans. Various configurations of this concept would provide high speed with low observables (LO) by eliminating rotor drag, signature, and rotor/body interactions.

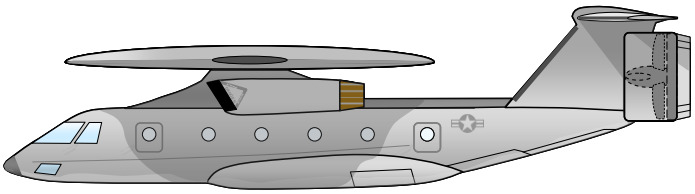

Figure 1-4: Artistic Impression of DiscRotor configuration.

The principal advantage of the DiscRotor is the combination of low-speed VTOL and high-speed fixed-wing operation with the ability to smoothly morph from helicopter flight to high-speed flight.

Hover flight and fixed-wing flight are the two main flight configurations for the DiscRotor. These are shown in Figure 1-5.

1) **Hover:** A set of blades are extended from the periphery of the disc. The disc and blades rotate together generating lift where the blades are the main lifting bodies. Low-speed maneuvers may be performed by utilizing cyclic pitch on the blades.
2) **Fixed-Wing Flight (a.k.a. High-Speed Flight):** There are two possible configurations for this mode of flight. Both configurations are studied in this effort.
    a. **Retracted Blades:** The blades will be fully retracted leaving only the disc wetted. The disc will stop rotating, i.e. fixed in relation to the fuselage. For the purposes of this study, no rotation of the disc during high-speed flight will be considered. The circular-disc wing will act as a low-aspect wing to generate the required lift.
    b. **Cruise (two extended blades):** In an effort to increase the efficiency of the disc-wing, two blades may be extended from the periphery of the disc opposite each other. The required lift will be generated by the disc-wing and blades together. Benefits will be realized due to the aerodynamics of formation of flight. The disc-wing shall be stopped and remain fixed in relation to the fuselage.

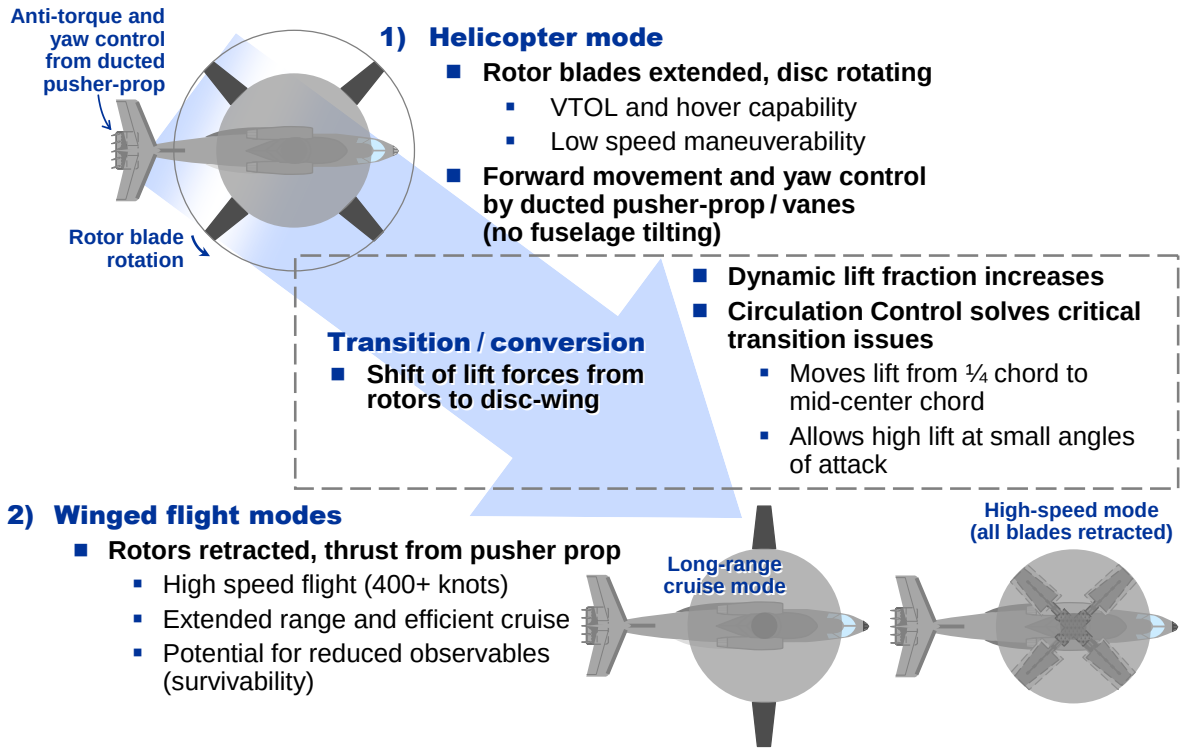

Figure 1-5: Diagram of the DiscRotor's Flight Modes.

1-3.1: Transition during flight

The DiscRotor will experience a period transition from hover to fixed-wing flight. This transition is critical to the DiscRotor's success, though it accounts for a relatively short period of flight time. Hover and high-speed flight will compose the majority of the flight time, and therefore, will be the focus of this study. Transition between modes will be re-examined in following efforts by the Boeing-VA Tech Team.

1-3.2: Benefits of concept

As mentioned, the principal advantage of the configuration comes from the combination of VTOL and high-speed operability while being able to smoothly morph from hover to high-speed flight. The concept embodies the best attributes of the lifting efficiency of helicopters with the high-speed, high-altitude capability of a fixed-wing aircraft.

The DiscRotor provides significant improvements in capability compared to current rotorcraft technology. It is expected the DiscRotor may be capable of dash speeds of 400+ knots in high-

speed flight modes. Some of the major performance attributes expected from this unique combination of helicopter and fixed-wing capability are:

- Rotor downwash in hover will be confined to the annulus between the edge of the disc wing and the tips of the blades. Beneath the wing and near a fuselage-mounted rescue hoist, the air velocity should be very low. Consequently operation of the rescue hoist, recovery of crew, stretchers, and other equipment is expected to be simplified.
- Hover download on the fuselage should be very low since the annular downwash will wet only the narrower nose and tail sections rather than the entire aircraft. For helicopters or tilt-rotors such download losses can amount to between 3% and 10% of rotor thrust.
- In high-speed mode, the retraction and stowage of the blades within the circular wing will offer low radar and acoustic signature capability to the aircraft.

Figure 1-6 compares the estimated cruise speed capability of this new concept aircraft with that of existing VTOL-capable platforms. It is estimated that the DiscRotor will cruise at speeds in excess of 400 knots, nearly three times as fast as the UH-60 when loaded with a full complement of personnel and equipment, and almost twice as fast as the V-22 Osprey.

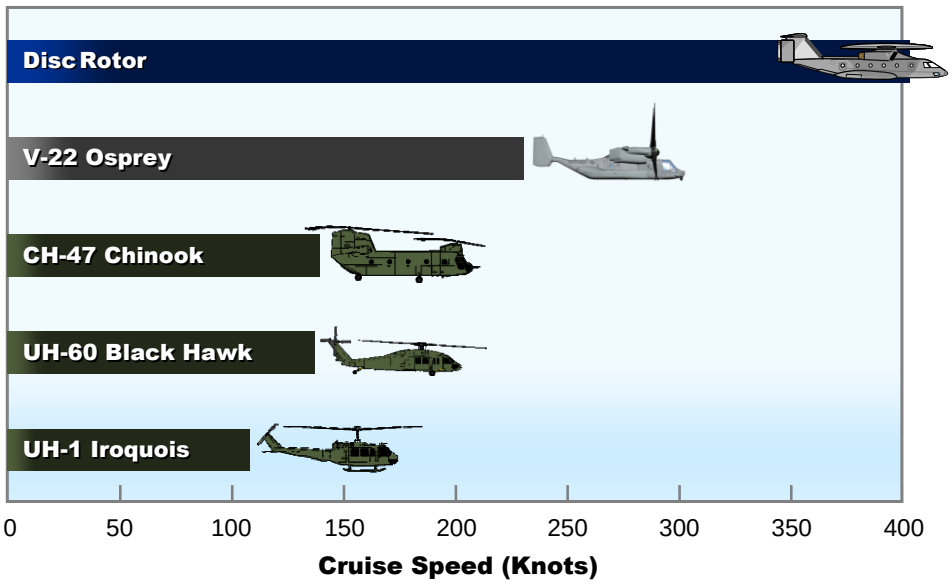

Figure 1-6: DiscRotor Speed Capability Compared to Other Rotorcraft.

1-3.3: Initial Sizing

As a starting point for analysis and design, an initial sizing study was conducted by partners from the Boeing Corporation. The decisions were guided by engineering principles, past research, existing aircraft and experience. The sizing study is summarized in Figure 1-7. These results were used in defining and fabricating generic models used in experimentation and numerical study.

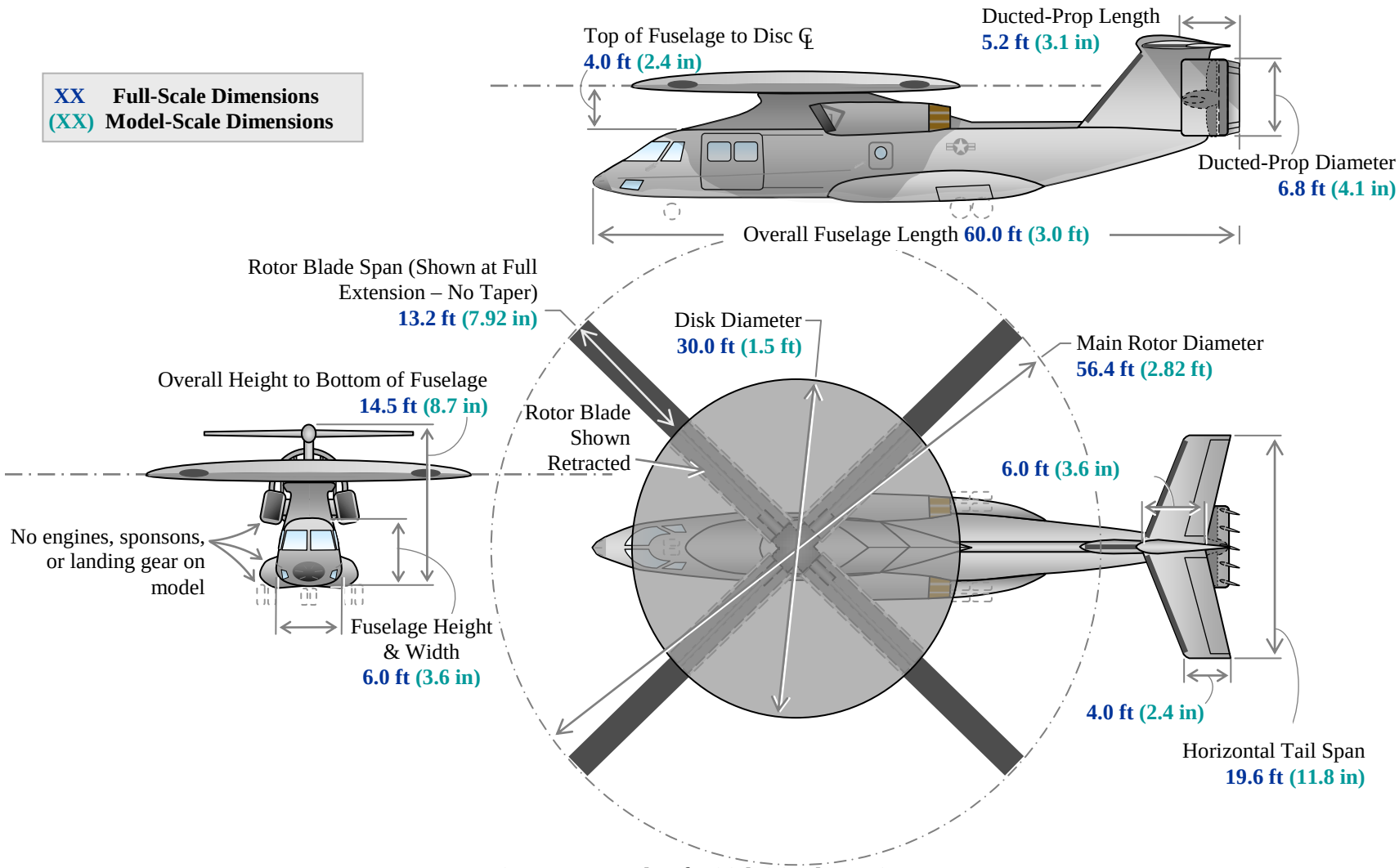

Figure 1-7: Results of Initial sizing by Boeing. Model dimensions are for a 1:20 scaled model.

1-4: Technological Issues

Combing VTOL and high speed into an aircraft is a challenging task. The overall objective of the Boeing/VA Tech program was to identify Critical Technical Risks and develop a Risk Reduction Plan to manage these risks. To support these tasks, a limited assessment of the basic aeromechanics of the concept was conducted using fundamental analyses, wind tunnel model testing and hover testing. The later chapters will describe the fundamental analysis and testing performed to support the Boeing/VA Tech team.

As identified during the work performed by Boeing/VA Tech, the principal DiscRotor critical technology and design issues are:

a. Transition / Conversion Dynamics
b. Vehicle Control Strategies
c. Rotor Blade Extension / Retraction
d. Propulsion System
e. Ground Effects

A. Transition / Conversion Dynamics: The DiscRotor will transition from hover to fixed-wing flight while in the air. This transition, or conversion, is difficult to achieve. Controls will be needed to manage longitudinal trim changes as the center of lift moves from the disc center (hover and low speed) to near the disc quarter-chord in the high-speed mode of flight.

Although transition is a critical technological and design issue, it will not be considered in the current study. It will be considered in future studies.

B. Vehicle Control Strategies: There must be the appropriate control mechanisms and control surfaces in order for a pilot to control an aircraft. This includes pitch, yaw, and roll control, and stability of the vehicle, the configuration and size of the tail, and the placement of the wing. During high-speed flight, control surfaces must be adequately arranged to allow a manageable level of control for DiscRotor pilots.

A series of fundamental scale-model wind tunnel tests was performed to investigate the aerodynamics of the circular wing mounted above a fuselage body. The flow field behind the wing/fuselage was examined. These wind tunnel experiments will provide necessary information for CFD validation and for design analysis of the control surfaces.

C. Rotor Blade Extension / Retraction: The aircraft must extend and retract the blades from the disc edges during hover while providing cyclic and collective blade pitch. This will add complexity to the design of the DiscRotor. Also, blade deployment/retraction mechanisms are essential components of the aircraft which cannot fail during flight. Therefore, the DiscRotor requires additional reliability and design considerations for an acceptable design.

Design issues are not addressed in this thesis and were investigated by Boeing. Results from hover testing were implemented into the design stages of the rotor's blade retraction system.

D. Propulsion System Concepts. A circular wing used for fixed-wing flight will generate a relatively large drag force. The DiscRotor will require a powerful propulsion system in order to overcome the inadvertent penalties of drag forces. It must be capable of powering the aircraft during hover and high-speed flight. Therefore, a propulsion system should be efficient at low and high advance rations. Risks and technical challenges of propulsion systems were evaluated by Boeing.

This thesis will not address this issue, however, the results from wind-tunnel testing and analysis were directly implemented into Boeing's early design stages.

E. Ground Effects. When operating close to the ground, there are significant changes in aircraft forces and moments. In some previous VSTOL aircraft these changes were considerable. The DiscRotor will be different from a conventional helicopter in that it will have an *annular* wake from the rotating blades. This wake may cause fluctuating pressures on the under-surface of the disc-wing and fuselage that will generate corresponding changes in forces and moments, requiring corrective control in order to trim.

Ground effects were a major focus of the current work. Hover analysis was performed to directly measure the ground effects on a small-scale rotor.

1-5: Document organization

The previous introduction provided a background of the DiscRotor concept to show that the DiscRotor is a novel aircraft concept, and to create some understanding of the technical issues for the DiscRotor. The following chapters provide the analysis and results from multiple experiments performed on the Virginia Tech Campus as part of the DiscRotor - Phase 0 Project. The results have been used in the design and analysis of the DiscRotor concept.

The general equipment and facilities utilized during the experimentation are described in detail in Chapter 2. It is intended to provide the essential background knowledge on the systems, useful for understanding of all the experiments performed. Specific setup and procedures for each test will be explained in Chapters 3 and 4. Readers are encouraged to read Chapter 2, however, those who already posses a firm understanding of the facilities and equipment may skip to Chapter 3.

The experiments have been divided into two main groups related to the flight modes of the DiscRotor concept. Each group is described in separate chapters. This organization is intended to facilitate publication of the chapters independently.

Chapter 3: Wind Tunnel Experiments (High-speed Flight). Wind tunnel experiments were performed on a small scale model designed to the dimensions shown in Figure 1-7. A balance, or six D.O.F. load cell, was used to measure the forces generated by the model when exposed to high wind velocities. By similitude, the forces can be calculated for the full-sized DiscRotor aircraft for design purposes.

Additionally, air velocity vectors downstream of the model were directly measured via a seven-hole velocity probe. These velocity measurements generate large amounts of data that were used as inputs into the early design of the DiscRotor aircraft and provided a fundamental understanding of the disc-wing's aerodynamics.

The procedures and results of the Wind Tunnel Experiments are described in Chapter 3.

Chapter 4: Hover Experiments (Hover Flight). This chapter describes all experimentation that relate to the hover flight mode of the DiscRotor helicopter. A "hover rig" was designed and constructed to facilitate direct measurement of the thrust and torque generated by a small-scale rotor with similar dimensions to Figure 1-7. Ground effects were investigated by utilizing a movable wall to simulate the ground. The results of hover experiments were applied to the design of the DiscRotor aircraft by Boeing.

Air velocities downstream of the rotor were measured to provide a greater understanding of the fundamental rotor aerodynamics.

The procedures and results of the Hover Experiments are described in Chapter 4.

2. Instrumentation and Facilities

In this chapter, the supporting facilities and instruments are described in detail. They were utilized in multiple experiments during this investigation but are not a major focus of any particular test. Individual experiment setup and procedures are explained in later chapters. This format was chosen to reduce repetition in the presentation of this work.

2-1: Facilities

Wind tunnel experiments were performed in the ESM Fluids Tunnel and the VA Tech Stability Tunnel. These tunnels are utilized in Chapter 3. To perform hover analysis, a "hover rig" was designed and constructed in the ESM Fluids lab as a task of this work. The hover rig is used exclusively for the work described in Chapter 4.

2-1.1: ESM Wind Tunnel

The ESM wind tunnel is an open-circuit, low-speed tunnel constructed in 1983. There have been minor modifications and improvements since construction. Figure 2-1 shows a schematic of the wind tunnel. Flow is "sucked" into the settling chamber, through the test section and finally through the fan. To reduce the turbulence level, one honeycomb and four nylon-conditioning screens are included in the settling chamber. A five-to-one contraction follows the settling chamber. The test section dimensions are 20 in x 20 in x 50 in (51 cm x 51 cm x 125 cm) and include a removable Plexiglas wall for easy access and monitoring during tests.

The tunnel is powered by a 15 hp motor. Free stream velocity in the tunnel is controlled by adjusting the drive pulleys at the motor. It can achieve free-stream velocities from 4 m/s to 35 m/s. The turbulence level does not exceed 0.51% at a free-stream velocity of 10 m/s, except for regions very near the tunnel walls. The flow across the test section has a velocity variation of less than 2.5% (Rulan).

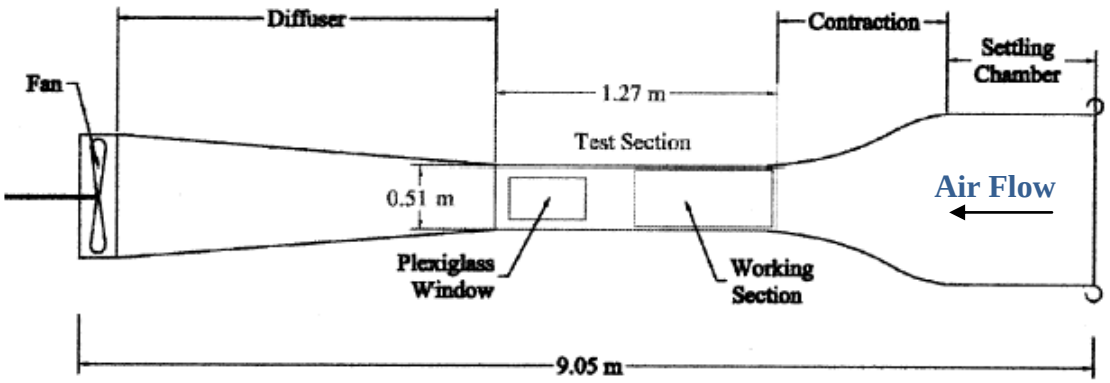

Figure 2-1: ESM Wind Tunnel Schematic (Rulan)

2-1.2: VA Tech Stability Tunnel

The Virginia Tech Stability wind tunnel is a continuous, closed-loop subsonic wind tunnel. The maximum achievable flow speed is 275 ft/s (83.8 m/s) in a 6-foot by 6-foot by 25-foot (1.83m x 1.83m x 7.62m) test section. This facility was constructed by NASA (previously NACA) in 1940 at the present site of NASA Langley Research Center, and was used mostly in the determination of aerodynamic stability derivatives. In 1959, the tunnel was moved to Virginia Tech Blacksburg Campus where it has since been located outside of Randolph Hall.

Figure 2-2 shows a schematic of the Stability tunnel. The settling chamber has a contraction ratio of 9 to 1 and is equipped with seven anti-turbulence screens. This combination provides an extremely smooth flow in the test section. The turbulence levels vary from 0.018% to 0.5% and flow angularities are limited to 2° maximum. The settling chamber is 3m long and the diffuser has an angle of 3°. The ambient temperature and pressure in the test section is nearly equal to the ambient outdoor conditions due to the presence of a heat exchanger. During testing the control room is maintained at the same static pressure as the test section. The tunnel fan has a 14-foot (4.27m) diameter and is driven by a 600 hp motor that provides a maximum speed of 230 ft/sec and a Reynolds number per foot up to 1.4×10^6 in a normal 6’ x 6’ configuration (Devenport, Mason and Oetjens).

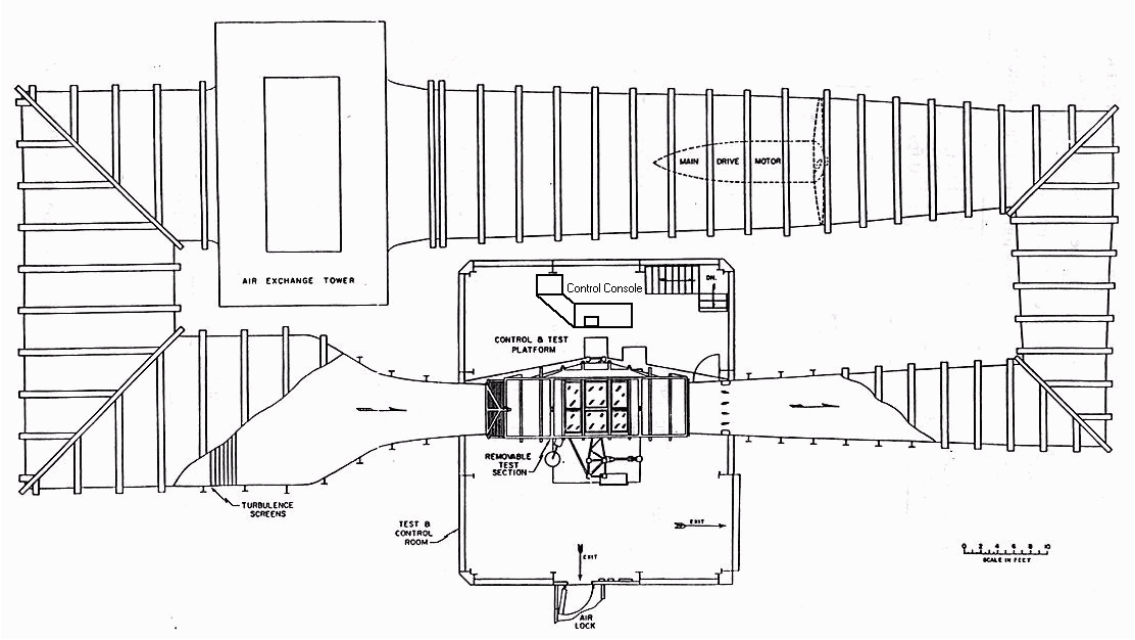

Figure 2-2: Stability tunnel schematic (Devenport, Mason and Oetjens)

2-2: Equipment

Multiple types of instruments were utilized to carry out the array of experiments performed during this work. Such items include load cells, balances, pressure transducers, a velocity probe, and feedback control devices. In many instances, the same instrument was utilized in multiple tests. For this reason, the supporting equipment is described in detail in this chapter to avoid repetition. Reference may be made to this chapter for detailed information on specific equipment.

2-2.1: FF-11VT Balance

The FF-11VT Balance is a custom manufactured load cell, or balance, that will directly measure six degrees of freedom (three forces, three moments) at about a single reference point. Each load is measured by an independent channel comprised of a full bridge. The internal strain gages of this unit are arranged such that the interaction effects are less than 1% of the full load. As a result, the forces and moments can be directly recorded, which can reduce the post-processing of the data and increase accuracy.

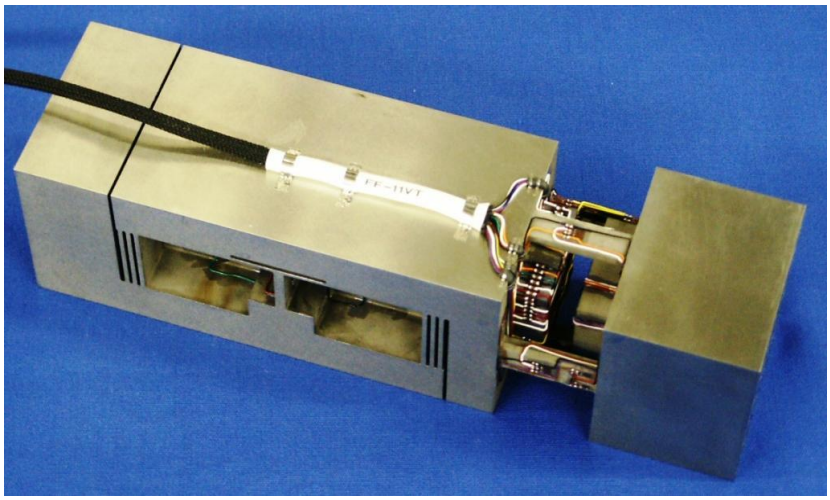

Figure 2-3: FF-11VT Balance

Signal conditioning for each channel was performed by a National Instruments Data Acquisition System. The exact system depends upon the location of each experiment being performed. An extensive calibration was performed for the balance by the manufactures (Spiers). Selected components of this calibration and detailed drawings are included in the Appendix. The calibration was verified before recording data during tests with a weight and pulley system.

2-2.2: Velocity Probe System

A velocity measurement probe can be a convenient way to obtain time averaged information about a flow field. A seven-hole probe, produced by the Aeroprobe Corporation was used to perform velocity measurements. Multi-hole probes can measure all three components of the velocity, the total pressure, and the static pressure at any given point.

The probe is constructed from several different machined parts and then assembled by Aeroprobe. Figure 2-4 shows the external geometry and components of the probe. The probe tip is made from brass, and has seven holes drilled into it. The probe used for this research has a tip with a conical shape and a diameter of 1/8”. The first extension is the same diameter as the probe tip and its length is approximately 20 probe tip diameters long. To increase the overall length of the entire probe, a ferrule and second extension was added. The diameter of the second extension is about 1.5 times that of the tip. The overall length of the seven-hole probe used is 6”. At the end of the probe, there is a brass mount. The shape of the mount is hexagonal, which allows it to be mounted into a collar with the same shape cutout, and then secured with a

setscrew. Each of the holes in the probe tip leads to a stainless steel tube, with its inside diameter matching the diameter of the holes. As the probe shaft diameter increases, each tube is telescoped into a larger tube, which finally protrudes from the back of the mount, and enables the connection of flexible Tygon tubing. Each connection is soldered and tested for strength and leakage. The final assembly is also tested for pressure "cross-talk", i.e. pneumatic communication between two or more probe holes and their associated tubing. Figure 2-5 presents structural details of a typical probe tip and sample dimensions for a 0.125" (1/8") tip diameter probe tip.

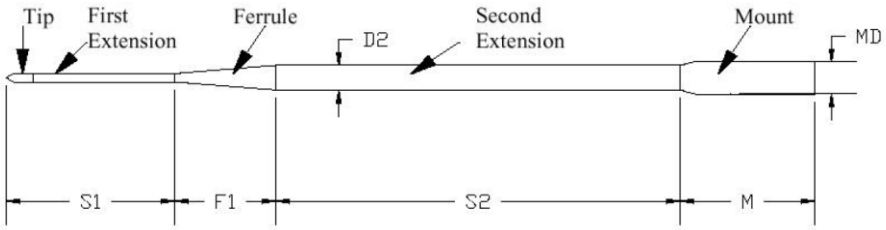

Figure 2-4: Geometry of a typical seven-hole probe. (Aeroprobe Corporation).

Because no two probes are identical after fabrication, and because small amounts of damage can occur to the probe over time, it must be cleaned and calibrated to provide accurate results. The probe was cleaned before any tests were run by pouring isopropyl alcohol through the ports and then drying the entire probe. Next, the calibration procedure was performed by placing the probe into a known flow field and rotating the probe through many different angles while acquiring data.

The principle idea of the probe's operation is the following: The pressure over a bluff body is the highest at the stagnation point and lowest near separation. If the flow direction forms small angles with the axis of the probe (below 2°), the center hole registers the highest pressure. If, however, the flow is steeply inclined with respect to the probe then one of the peripheral holes on the windward side of the probe tip registers the highest pressure, while on the leeward side of the probe, the flow is separated. The pressure information provided by the three holes in the separated region is not used. Using this method of calibration allows the instrument to measure the direction and the magnitude of the velocity (Aeroprobe Corporation).

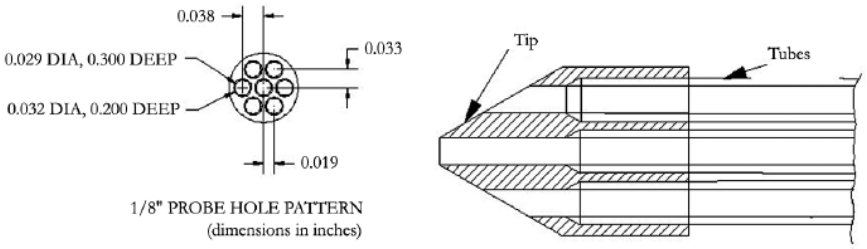

Figure 2-5: Typical Tip Geometry of a Seven-Hole Velocity Probe (Aeroprobe Corporation).

To obtain actual velocities with the probe, several pieces of equipment must be used in addition to the probe itself. Tygon tubing was attached to the leads of the probe. The tubing was then connected to an Electro-Static Pressure Transducer (ESP) manufactured by Pressure Systems (model ESP-32HD). The ESP is a compact device containing multiple pressure transducers; each transducer converts an applied pressure to a voltage. ESP used contains 32 separate ports, each with a usable pressure range of ±10" of water. The first seven ports were connected to the seven Tygon tube leads from the probe. The eighth port on the ESP was connected to the total pressure side of the wind tunnel Pitot tube. This enabled the measurement and recording of the wind tunnel velocity at the same instant data were recorded from the probe (Aeroprobe Corporation).

An Aeroprobe Main Unit was used to interface the ESP with the data acquisition board in the computer. The Main Unit includes hardware that interfaces with the ESP, and motor controllers to drive the stepper motors used for the 3-axis probe traversing scales. The traversing system consists of three-axis motorized traversing scales with the probe mounted to the z-axis. The scales allowed the probe to be moved to the desired locations in the flow field.

This system was used to measure flow fields in multiple experiments. The Aeroprobe system provides a high degree of accuracy and flexibility to meet multiple experiment requirements.

3. Fixed Wing Flight

A circular wing, or disc, is the primary lifting surface of the DiscRotor aircraft during high-speed flight (approx. 400knots). During the high-speed flight, the disc will be fixed (i.e. not rotating) at some height above the fuselage. The disc is a low-aspect-ratio wing, which is known to be relatively inefficient lifting surfaces. There are multiple methods to improve the performance of a circular wing such as circulation control (Imber and Rogers). Only one method to improve performance is considered where "blades" are added to the tips of the disc in the spanwise direction. This method was chosen based upon results from experiments on VTOL aircraft concepts with similar wing shapes (Swanson and Stroub).

Blades will be similar to Reverse Velocity Rotors (RVRs). RVRs have symmetric airfoil shapes and therefore have identical lifting characteristics when oriented at 0^o or 180^o to the free stream (Van Riper). Experimental models where blades are extended will have rounded leading and trailing edges.

The underlining purpose of these experiments was conducted to aid in the development of the DiscRotor concept. Much of the model's geometry and dimensions were based upon work performed in tangent with the Boeing Corporation. Requirements of the design analysis included information about the aerodynamic forces generated by a circular-shaped wing, including the wake behind a circular wing when a fuselage and tail is present. The aim here is not the design of the actual aircraft, but rather to provide the required information for the design and analysis of the DiscRotor concept.

A series of experiments have been performed. They are separated into two groups: force measurements and wake measurements. Two Reynolds numbers near 0.5 and 2 million were considered for tests. Focus will be given to the experiments at the higher Reynolds number.

3-1: Experiment Setup

An initial sizing study performed on the DiscRotor concept by Boeing Corporation. A generic model was then defined to study the fundamental aerodynamics. The model wing can be

described as a flat, circular surface with a thickness ratio of 6%. Edges were rounded at a constant radius with a curvature of 3% such that there is a smooth junction at the top and bottom surfaces. No camber is present in the disc or blades. A fuselage was not considered in the low Reynolds number tests but a generic fuselage is present in all tests at the higher Reynolds number. Unless otherwise noted, the diameter of the wing is used as the reference length even when blades are considered.

3-1.1: High Reynolds Number

Higher Reynolds numbers were achieved in the Virginia Tech Stability wind tunnel which is a continuous, closed-loop subsonic wind tunnel. In this tunnel, free-stream wing speeds up to 200 fps (60m/s) were reached in a 6 ft by 6 ft test section. A combination of settling screens and a large contraction ratio provides an extremely smooth flow in the test section. The tunnel is equipped with a "sting" on which the model was mounted, capable of pitching from -8º to 22º. The model was maintained at the center of test section during all tests. Refer to Chapter 2 for more detail on the Stability Tunnel.

The fuselage body has a 3.6" x 3.6" cross section and a total length of nearly three feet. There is 2.4" gap between the bottom of the disc and the top of the fuselage. The disc has a radius of 9" and a thickness of ¾".

If present, two blades were extended from the disc in the spanwise direction. Various blade lengths and chords were tested, with the length is defined as the distance from the edge of the disc to the tip of the blade. The same model was tested in both force and velocity measurements which are further described in sections 3-2: and 3-3: .

Figure 3-2 shows the generic model placed upon the sting.

The fuselage was built around the FF-11VT balance, which is an internal six degree of freedom load cell, and the aerodynamic forces could be directly measured. With this instrument, interaction and nonlinearities effects have been shown to be negligible (Spiers). See Chapter 2 for additional information on the FF-11VT balance. The balance was rigidly connected to the sting and the fuselage was connected to its opposite end. The fuselage only made contact with a

single surface of the balance. Loads were measured over five seconds and an average was obtained.

To extract useful information about the wake behind the model, the velocities in a two-dimensional plane were measured experimentally using a seven-hole probe. This probe measures the three components of the velocity, the total pressure, and the static pressure at the tip of the probe. The probe tip is made from brass, and has seven holes drilled into it. The probe used for this research had a tip with a conical shape and a diameter of 1/8". The pressures are measured from each hole and the flow properties are calculated. The pressures are measured by a high-density ESP scanner. The velocity probe is designed and calibrated by Aeroprobe Corporation. The required instrumentation and programming were also purchased from Aeroprobe Corporation. See Chapter 2 for additional information on the seven-hole probe.

The velocity probe was displaced in a two dimensional plane that was perpendicular to the free stream. This placement was completed by mounting the probe onto a computer-controlled traversing system powered by two stepper motors. The traversing controller was integrated with the velocity probe software. For each point in the grid, two seconds of data are obtained and time-averaged velocity vectors are recorded.

Exploiting symmetry, only half of the model's wake was considered. Slightly less than three inches near the spanwise center of the model could not be measured by the velocity probe. This was due to the presence of the sting used to mount the model. This is not a concern as the flow in this region is predictable and is recorded in the lower Reynolds number experiments.

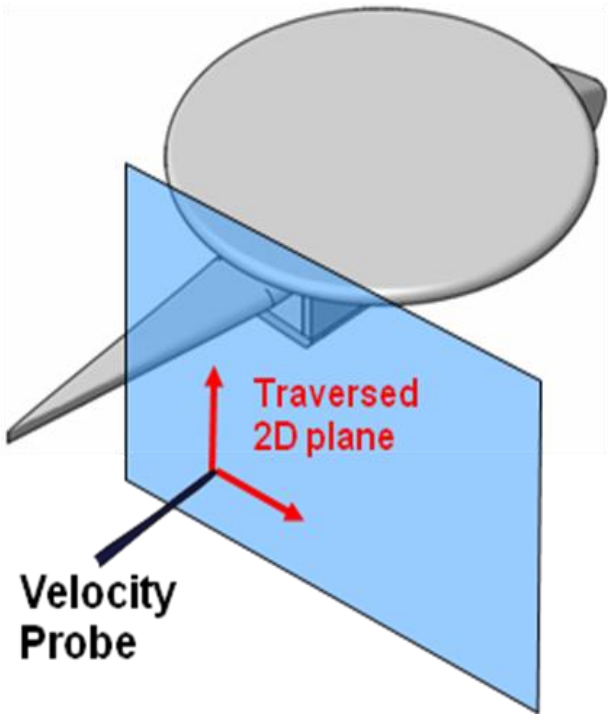

Figure 3-1: Sample Plane Traversed by the Seven-Hole Probe
The blades or sting are not shown.

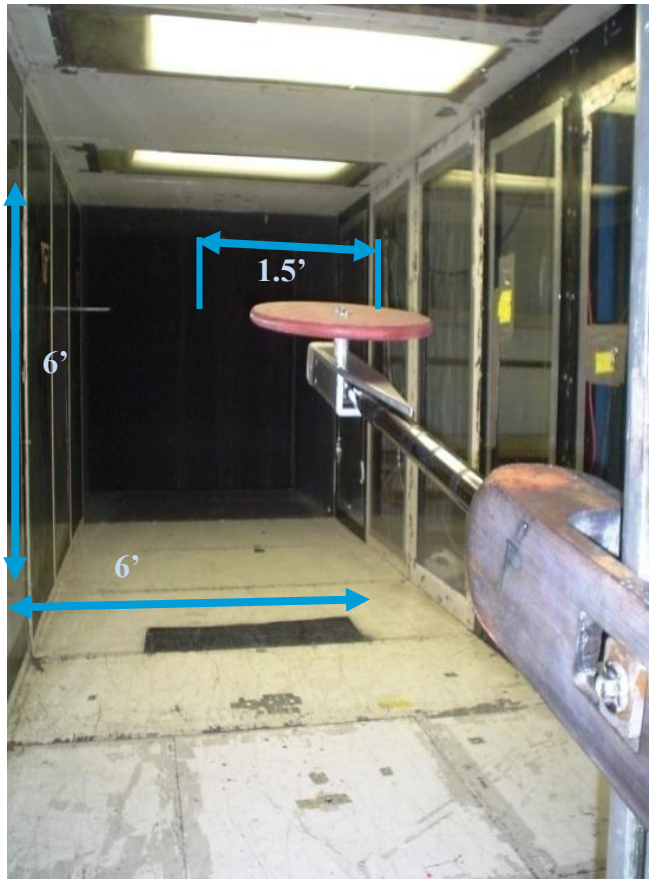

Figure 3-2: Model Mounted on Sting in VA Tech Stability Tunnel

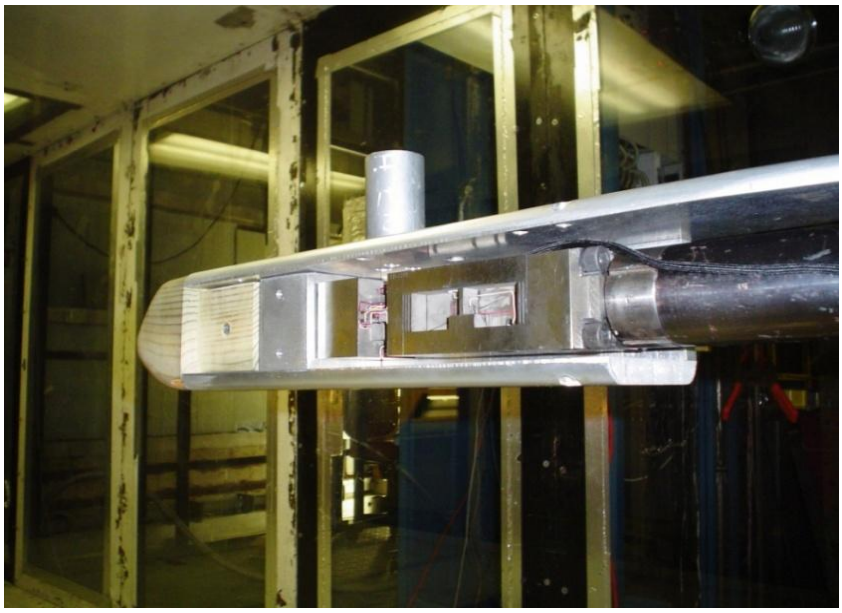

Figure 3-3: Mounted FF-11VT inside Fuselage Model.
The disc and side of fuselage not shown.

3-1.2: Low Reynolds Number

A similar disc with a diameter of 12 in and 1 in thick was tested at a Reynolds number near 0.5 million. Force measurements were performed in the Open-Jet tunnel in the AOE department at Virginia Tech. This tunnel is a continuous circuit where the test section is a circular cross-section with a 3 ft diameter. Much of the experimental setup was similar to the higher Reynolds number tests. A "sting" was placed in the rear of the test section that was capable of reaching angles of attack up to 30 degrees. The GA-10 was placed at the end of the sting to which the disc was firmly attached at the center of the disc at a smaller 6 D.O.F. balance. The balance protruded nearly 3/8 of an inch on the pressure side of the wing due to the disc thickness. This protrusion was only over a small part of the wing and is not believed to have any significant impact on the results. Lift, drag and pitch were measured at angles of attack in one degree increments between 0^{o} and 30^{o}. The model mounted in the tunnel is shown in Figure 3-4.

Low Reynolds number velocity measurements were performed in the ESM wind tunnel which is an open-circuit, low-speed tunnel. The square test section is 20 in by 20 in. This reduced test section size placed constraints on the experiment model. The model was "split" into two pieces at its mid-span and a wall was placed in the tunnel to enforce a symmetry condition at the wing. A traversing system was placed into the tunnel and average velocities in a 2D grid perpendicular to the flow were obtained. The full test apparatus without the tunnel wall is shown in Figure 3-5.

Figure 3-4: Low Reynolds Test with Blades Extended in Open-Jet Tunnel.

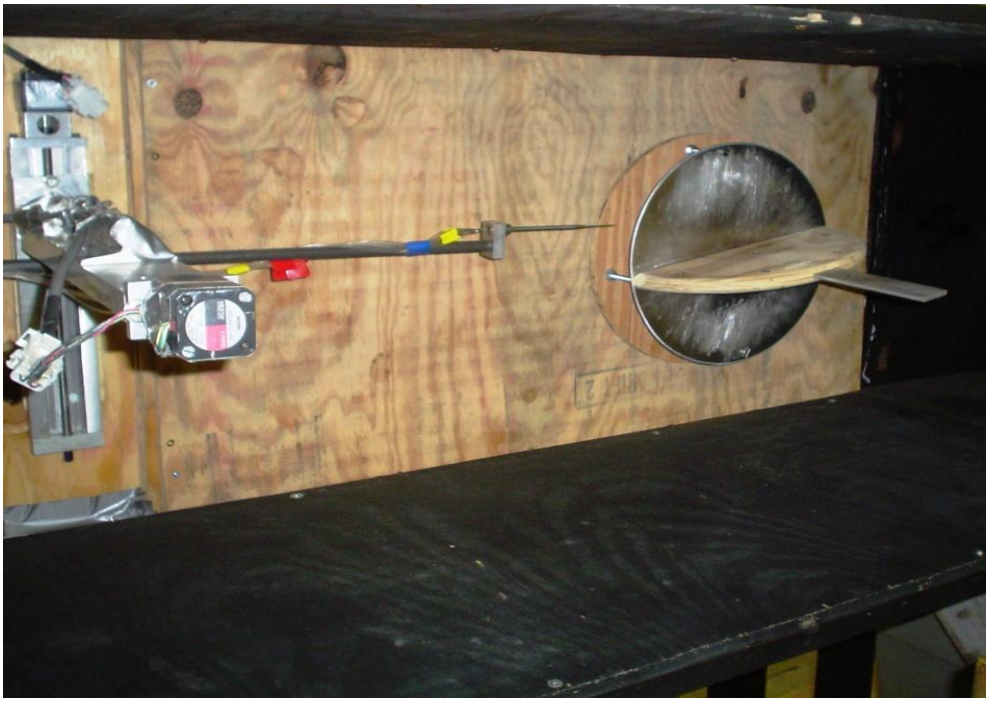

Figure 3-5: Low Reynolds number tests in ESM tunnel. Flow from right to left.

3-2: Force Measurements

Aerodynamic forces were measured for a circular wing described in the previous section. The Reynolds number, blade lengths, angle of attack and fuselage were all varied in the experiments. Lift and Drag coefficients as well as the L/D ratio were computed for angles of attack from 0º to 20º. Only the most relevant data are shown. Additional data can be found in the Appendix.

The normal and tangential forces (with respect to the disc) are recorded by the balance. These forces are resolved into the Lift and Drag forces based upon the angle of attack. The forces measured during tests are presented in Figure 3-6 to Figure 3-9. The surface area used to calculate the coefficients has been adjusted for the increased area when blades are present.

The presence of the fuselage produces negative lift at a zero angle of attack, which explains the negative Lift generated at zero angle of attack in Figure 3-6. At most angles of attack, the forces generated by the disc are significantly greater than the forces generated by the fuselage. However, at a zero angle of attack, the disc does not generate a normal force, which results in greater forces generated from the fuselage compared to the disc. Information on the fuselage can be found in the Appendix. From the force measurements, the Lift over Drag (L/D) ratios are calculated for each angle and presented in Figure 3-7.

The linear fit of the Lift coefficient in Figure 3-6 suggests that the flow did not experience separation in the range of angles of attack. This conclusion is proposed due to the shape of the L/D curve. The general shape of the L/D ratio is characteristic of low aspect wings, which indicates that the disc acted as a poorer lifting surface compared to conventional, higher-aspect ratio wings.

The blade extensions lead to significant increases in the lift coefficient and some increases to the drag coefficient. The addition of blades increases the planform area of the wing, but the reference area is adjusted accordingly when reducing the forces. When blades are added to the disc, the effective aspect ratio of the wing increases and causes a more efficient lift production. The maximum L/D ratio is nearly 4.5 at an AOA of 5º with the presence of blades. A notable

change in the Lift coefficient derivative with respect to the angle of attack occurred at the same angle of attack as the maximum L/D ratio.

Similar results were obtained at a Reynolds number of 0.5 and are plotted in Figure 3-8 and Figure 3-9. Plots of the Lift coefficients have similar slopes with respect to the angle of attack. There is also slight change in the slope which occurs near 6º with blades added. This change was noted at both Reynolds numbers. The Drag coefficients differ where the lower Re case indicates a much higher drag at all angles. Therefore, the magnitudes of the L/D ratios do not match but maxima occur at the same angles of attack.

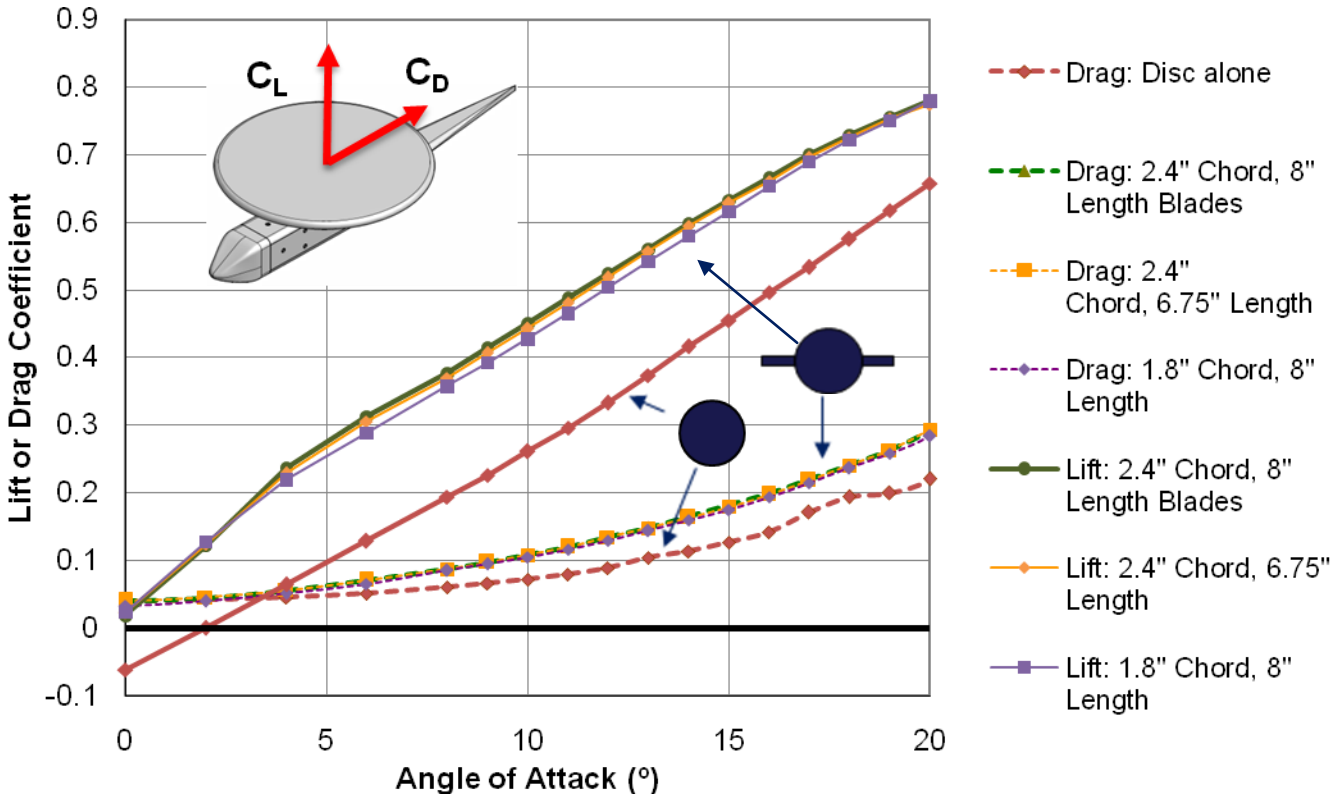

Figure 3-6: Lift and Drag Coefficients, Re= $2x10^6$. Reference area adjusted for blade extensions.

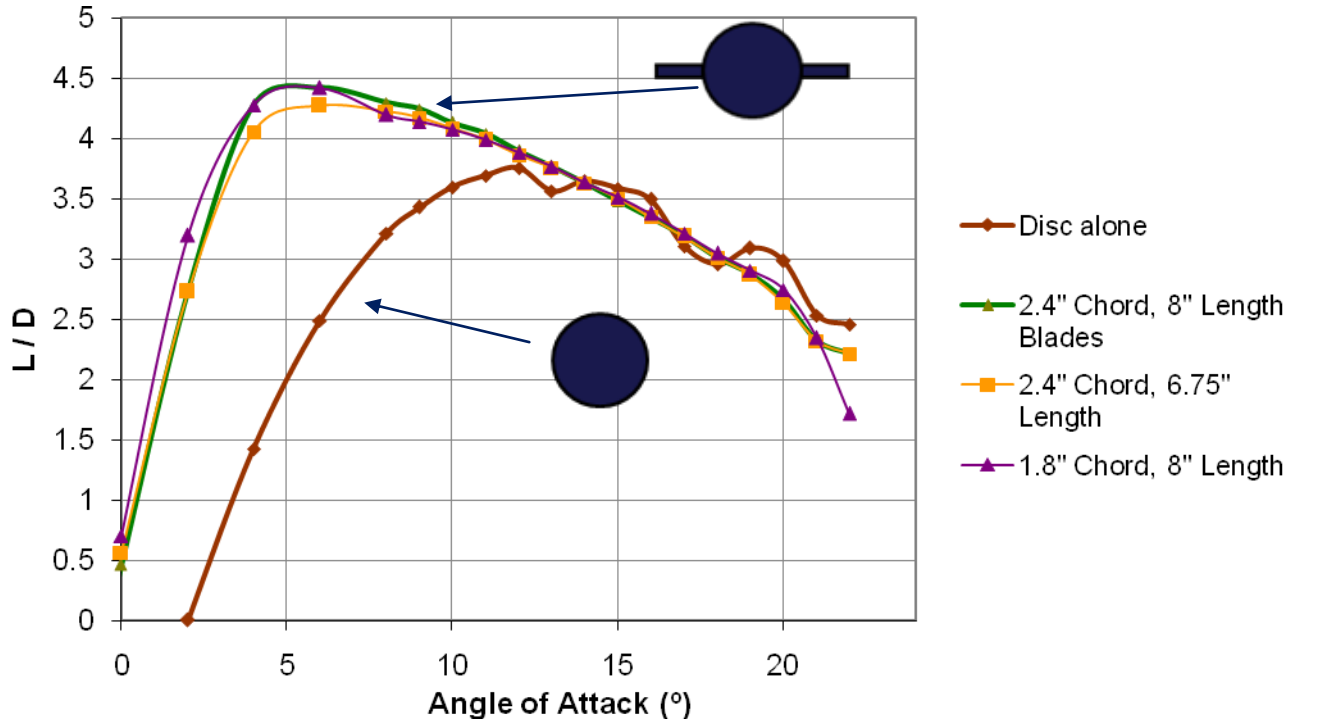

Figure 3-7: Lift over Drag ratio, Re= $2x10^6$.

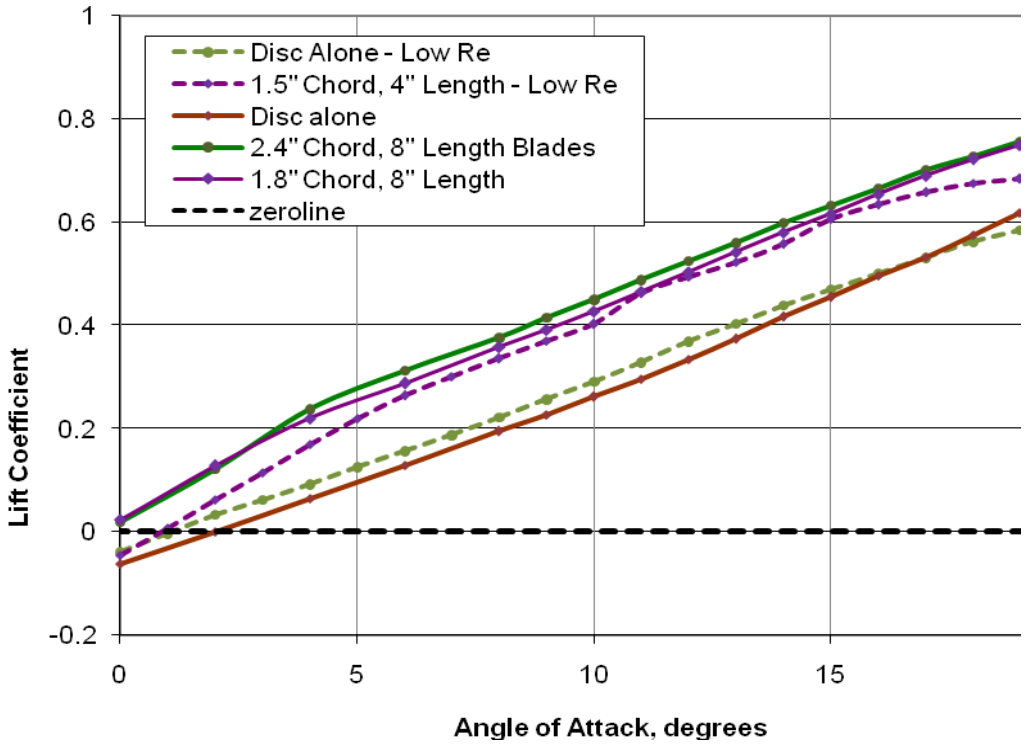

Figure 3-8: Lift Coefficients, Re= 0.5×10^6.
Reference area adjusted for blade extensions if present.

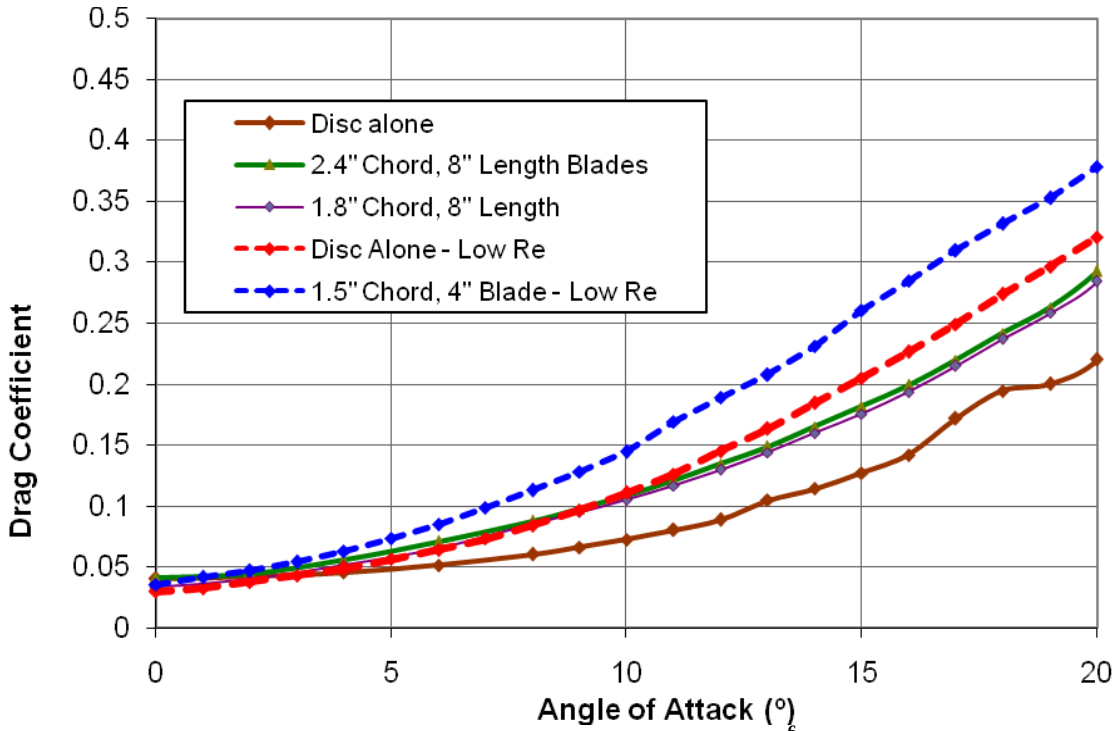

Figure 3-9: Drag Coefficients, Re= 0.5×10^6.
Reference area adjusted for blade extensions if present.

3-3: Velocity Measurements

Velocities were recorded in planes perpendicular to the flow at multiple distances downstream of the disc for three angles of attack. Tests were conducted with and without blades extended from the model to examine their effect. Only one size of the blades was considered at each Reynolds number due to the time restraints required to perform these tests. At the low and high Re the blades were 1.5" chord & 4" length and 2.4" chord & 8" length, respectively. An extensive amount of data was recorded during the velocity measurements and only the high Reynolds number at 10^{o} will be shown in this section as an example. The entirety of the results may be found in the Appendix.

3-3.1: Vector Fields

To first visualize the experimental data, the spanwise (y-axis) and vertical velocities (z-axis) are plotted as vectors in the plane perpendicular to the free stream and referred to as the vector field (Figure 3-10). The free stream and disc radius have been used to nondimensionalize the velocity and positions, respectively. Therefore, the horizontal and vertical axes are reduced by the radius of the disc (i.e. y/R and z/R, respectively). The center plane of the disc has been projected into the plots to give a point of reference. The thickness of the disc is not visible in Figure 3-10 through Figure 3-15, the appearance is solely due to the angle of attack. Also, note that the fuselage is not shown but was present during tests.

When performing experiments, errors may occur which cause the results to show a few "bad vectors." These vectors are known to be incorrect by inspection and identified by sharp discontinuities in the vector field. The causes of these vectors are often hard to identify for they seem to occur randomly. Increasing the record length used to obtain an average will minimize, but not eliminate, their presence. This solution, however, is not always practical as it significantly increases the total time required to perform an entire test. A record length of two seconds was used and was greater than required for the identification of any periodicity in the flow.

From these vector fields, we can see a vortex located near the tip of the disc. The core appears as an area of low velocity in a small area surrounded by vectors in a counter-clockwise direction.

Velocity inboard of the vortex (toward the center of the wing) is directed downward and directed upward outboard of the vortex. In a very simple description, the flow behind the circular wing appears as a “horseshoe” vortex where the wing is represented by a single vortex line. Where the vortex tube intersects the plane appears as the tip vortex. A vortex would create velocities in a clockwise direction if measurements had been taken on the opposite side of the wing.

The vector field becomes more complex when blades are added to the model as seen in Figure 3-11. There are two vortices present and are located near the blade and disc tip. Where applicable, the vortex near the disc tip is referred to as vortex 1 and vortex 2 refers to the one at the tip of the blade. Both generate counter-clockwise velocity vectors. Inboard of the disc there is still a strong downwash, and the area outboard of the blade experiences upwash. The blade will experience upwash along the majority of its span due to the vortex created by the disc. If we were to analyze the disc and blade independently from one another, we would not be able to capture this effect.

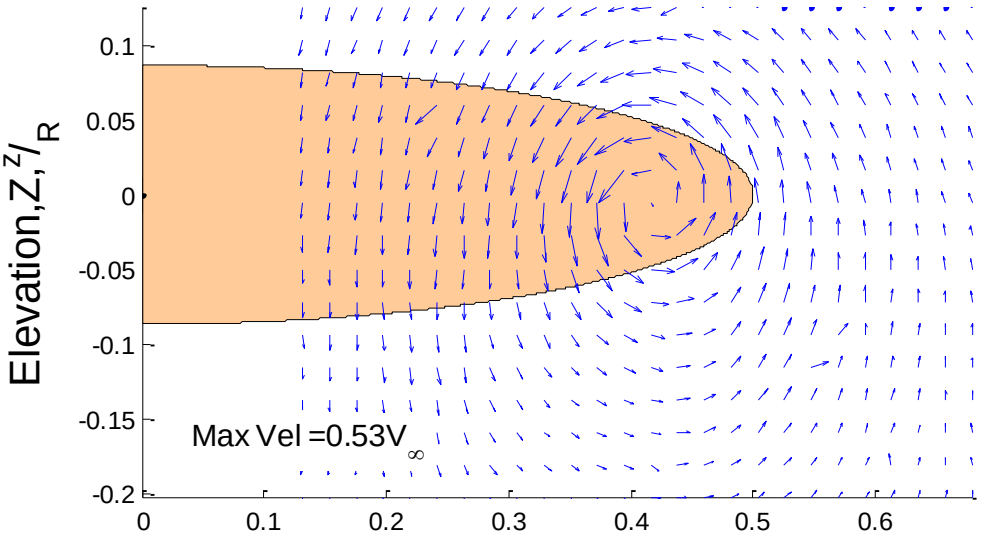

Figure 3-10: In-plane Velocities for Disc without Blades, Re 2x10^6, AOA 10°. Measurements at One Disc Radius Downstream of Trailing Edge.

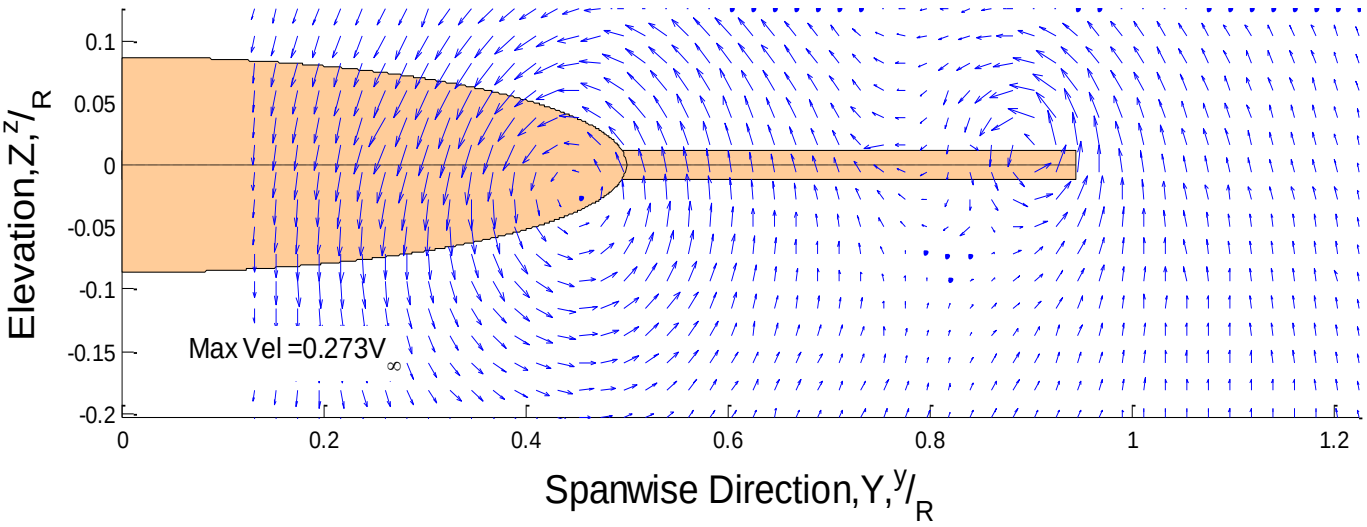

Figure 3-11: In-plane Velocities for Disc with Blades, Re 2x10^6, AOA 10°. Measurements at One Disc Radius Downstream of Trailing Edge. Blades have 2.4 in Chord and 8 in length.

3-3.2: Momentum contours

The above vector fields only show two components of velocity, the components in the yz plane. The third component, that is perpendicular to the measurement plane, is relevant for design purposes. We define a momentum ratio as the magnitude of velocity at a point divided by the free stream velocity. This ratio is calculated at every point in the vector field and the contours of similar values are plotted in the plane. A value of 1 would correspond to a velocity equal to the free stream. Values lower than 1 indicates that the momentum has changed, and is not uniformly parallel to the free-stream velocity.

A momentum contour plot is shown in Figure 3-12 for the 10º case without blades. There are two regions in which the flow experiences momentum loss. In the figure, there is a circular shape which corresponds to the vortex created by the disc. Inside a vortex, the velocities are very high however the viscous effects will be magnified as well. By one diameter downstream, there will be a loss of energy cause by this phenomenon. The second region of loss (and much larger) occurs below the disc where the maximum will occur near the center in the spanwise direction. Again, this is caused by the nonideal conditions of viscosity caused by the tangential force along the disc's surface.

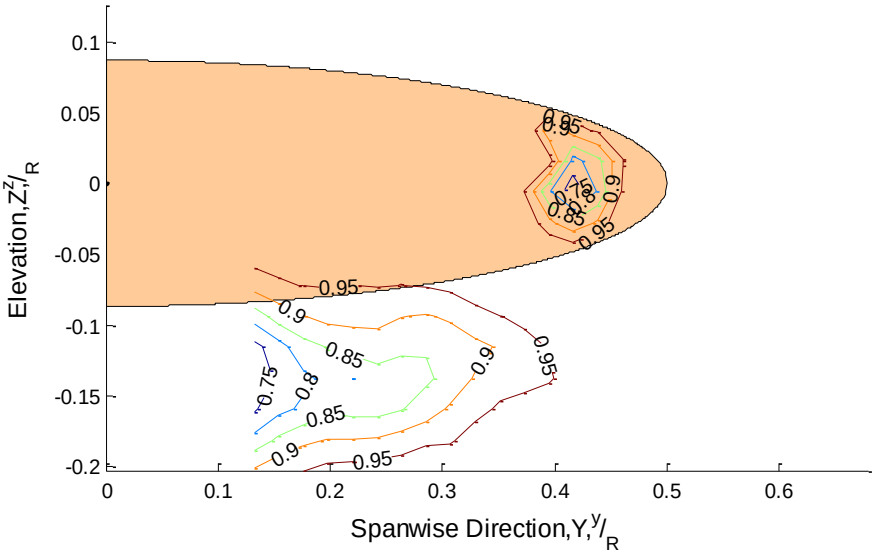

Figure 3-12: Momentum Contours, Disc Without Blades, 10º AOA, Re 2x106. Measurements at One Disc Radius Downstream of Trailing Edge.

When blades are added, the two regions are present but generally more difficult to interpret. The momentum contours join together to form a curved region following the lower trailing edge of

the disc. Very little loss occurs behind the blades compared to the loss from the disc. This is expected because the blades have smaller chords and thinner than the disc, therefore, less frictional losses will occur. Because of the restrictions for mounting of the model, the maximum momentum loss near the center of the disc was not able to be measured at the higher Reynolds numbers. The flow behind the midspan of the disc was measured at the lower Reynolds number included in the Appendix.

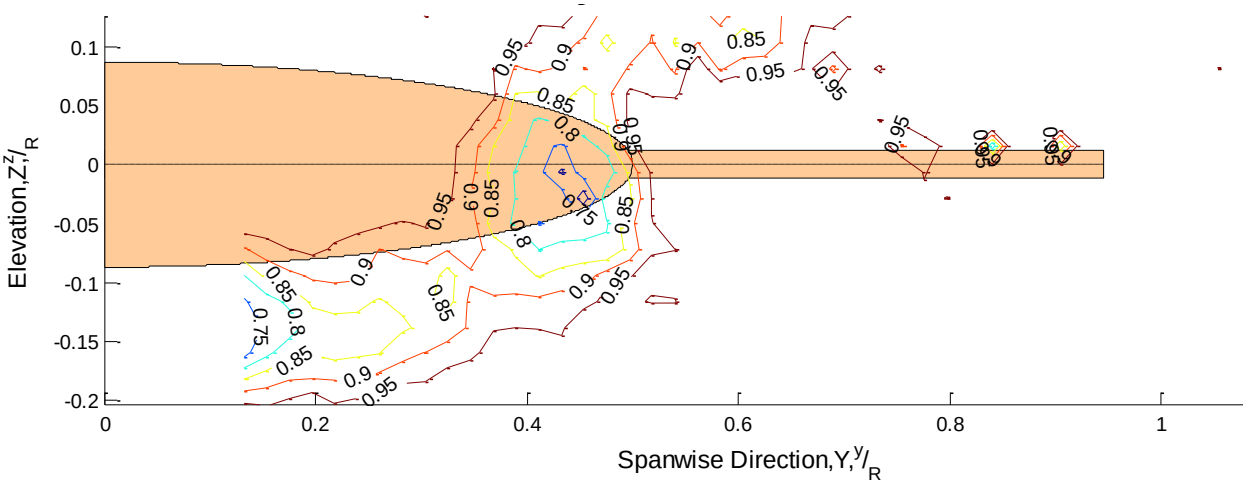

Figure 3-13: Momentum Contour plot for 10º AOA with blades. Re= 2 million

3-3.3: Vortex Strengths

To numerically describe the features of the flow, the strength of the tip vortex is calculated in three ways which yield similar results. The first uses a line integral around a closed curve capturing the vortex core. The circulation strength is defined as

$$\Gamma = \oint \vec{V} \cdot d\vec{r}$$

where Γ is the circulation, $\vec{V}$ is the measured velocity field and $d\vec{r}$ is the line segment along the curve encapsulating the tip vortex. This equation is discretized and the integral is evaluated a rectangular curve shown as a red dotted line in Figure 3-14.

In the second method, we first calculate the vorticity at each point where the vorticity is defined as

$$\vec{\zeta} = \vec{\nabla} \times \vec{V} \qquad \text{and} \qquad \Gamma = \iint \vec{\nabla} \times \vec{V}\, \mathbf{dA}$$

where $\vec{\zeta}$ is the vorticity as a point, $\vec{\nabla}$ is a vector of partial derivatives in their respective directions and $\mathbf{dA}$ is an infinitesimal area element. The area of integration is the same as the area enclosed by the curve defined for the line integral. For presentation and comparison purposes, the vorticity is calculated at every point then divided by the maximum value of vorticity in the flow. A value of 1 refers to the maximum value of vorticity (at a point) found in the flow. Finally, the strength of the vortex is found by a summation over the area enclosed by the same curve defined from the line integral calculation.

These two methods of calculating the circulation are not independent as they are related with Stokes' theorem and both values of the circulation should be equal. The difference is how the circulation is calculated numerically. By properly defining the curve for integration, the two ways of computing the circulation will yield nearly identical results which differ by less than 3% for the sample set shown. In almost all cases, matching results were obtained by defining a curve of integration that best coincides with the 0.05 vorticity contour. In this way, the proper curve is defined and can be checked for all data sets.

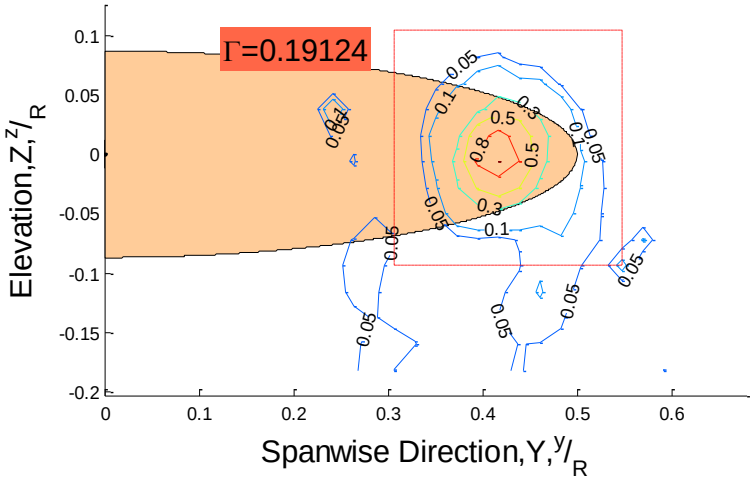

Figure 3-14: Vorticity Contours, 10° AOA, One Radius from Trailing Edge, Re = 2x10^6. Dotted Red Line Shows Curve of Integration.

As a third method of determining the vortex strength, the flow field is fitted to the Oseen vortex model which includes a viscous damping term where the tangential velocity is given by

$$V_\theta = \frac{\Gamma}{2\pi r}\left[1 - e^{-\left(\frac{r}{2B}\right)^2}\right]$$

where V_θ is the tangential velocity at some point, r is the distance from the vortex center to the point, Γ is the strength and B is the viscous term. When comparing the ideal and real vortex models, the strength should be independent of the method of calculation. A nonlinear, least squares regression method is applied to the flow field to compute the position, strength and viscous terms. An initial "guess" is required for this regression where results from either of the first two methods are used to determine appropriate initial values. Details can be found in the appendix. This final method produces the most detailed description of the tip vortices and results of all tests are included in Table 3-1and Table 3-2.

Using the three methods described, the vortex strengths were determined experimentally. When comparing the vortex strengths from each method, only a 5% variation was found. Therefore, only the fitted data to the real Oseen vortex model is presented in this section in Table 3-1 and Table 3-2. The vortex strength has been reduced by dividing by the disc diameter and the free stream velocity.

Table 3-1: Vortex calculations for Re = 0.5 x10^6 and 6" disc radius.

AOA	Blade Info.	Dist. Downstream	Vortex 1				Vortex 2			
			Span. Pos	height	Γ	B	Span. Pos	height	Γ	B
2	None	1 disc radius	0.3360	-0.0856	0.0485	0.0103	N/A	N/A	N/A	N/A
6	None	1 disc radius	0.3750	-0.0864	0.1132	0.0146	N/A	N/A	N/A	N/A
10	None	1 disc radius	0.3931	-0.0974	0.2216	0.0371	N/A	N/A	N/A	N/A
6	1.5"ch, 4"length	1 disc radius	0.3878	-0.1119	0.1016	0.0393	0.9540	-0.0618	0.1272	0.0700
10	1.5"ch, 4"length	1 disc radius	0.4170	-0.0966	0.1965	0.0503	0.9246	-0.0558	0.0737	0.0169

Table 3-2: Vortex calculations for Re = 2 x10^6 and 9" disc radius.

AOA	Blade Info.	Dist. Downstream	Vortex 1				Vortex 2			
			Span. Pos	height	Γ	B	Span. Pos	height	Γ	B
8	None	1 disc radius	0.4077	-0.0409	0.1547	0.0260	-	-	-	-
10	None	1 disc radius	0.4204	-0.0072	0.2008	0.0262	-	-	-	-
15	None	1 disc radius	0.3993	-0.0402	0.2888	0.0340	-	-	-	-
10	None	1"behind trailing edge	0.4356	-0.0282	0.1971	0.0287	-	-	-	-
8	2.4"ch, 8"length	1 disc radius	0.4235	-0.0688	0.1602	0.0443	0.8908	-0.0174	0.0485	-0.0112
10	2.4"ch, 8"length	1 disc radius	0.4404	-0.0332	0.2169	0.0529	0.9034	0.0117	0.0596	0.0087
15	2.4"ch, 8"length	1 disc radius	0.4198	-0.0452	0.2828	0.0507	0.8921	-0.0092	0.0686	-0.0080
10	2.4"ch, 8"length	1"behind trailing edge	0.4647	-0.0437	0.1997	0.0414	0.9290	-0.0129	0.0591	0.0086
10	2.4"ch, 8"length	2 disc radius	0.4113	-0.0728	0.2394	0.0753	0.8794	0.0304	0.0403	0.0091

3-3.4: Downwash

The interest in the wake behind the circular wing has been driven by a need to quantify the downwash for practical design purposes such as the effect on any rear-mounted control surfaces. Because of its low aspect ratio, the tip vortices shed from the circular wing are close together causing a large downwash compared to standard wings. The assumption of uniform downwash is not valid over the entire wing. Nearly uniform downwash is shown over half of the wing (centered at the midspan) but large gradients exist for locations that are 25% from the wing tips. Once outside the tip vortex, there is a strong upwash.

When blades are added to the model, the vortex shed near the junction of the blade and wing causes a large upwash on the blade. This interaction causes the blades to generate more efficiently (i.e. higher L/D). The upwash along the blades will transition to downwash in the spanwise direction due to the second vortex shed at the tip of the blade.

All three components of velocity have been shown in the vector and momentum plots above, however, it is difficult to present the information in a meaningful way for use in the design of an aircraft. Two types of figures are used to describe the downwash in the wake where the same information is presented in Figure 3-15. One figure plots the downwash as various contours in

the 2D plane. This shows that the downwash varies with in the spanwise direction and in elevation. The uniform downwash assumption is not appropriate for the entire wing. The second method plots the downwash along a line in the spanwise direction. Different elevations are plotted in the same figure. For a specific elevation, the assumption of uniform downwash across the entire span is not appropriate.

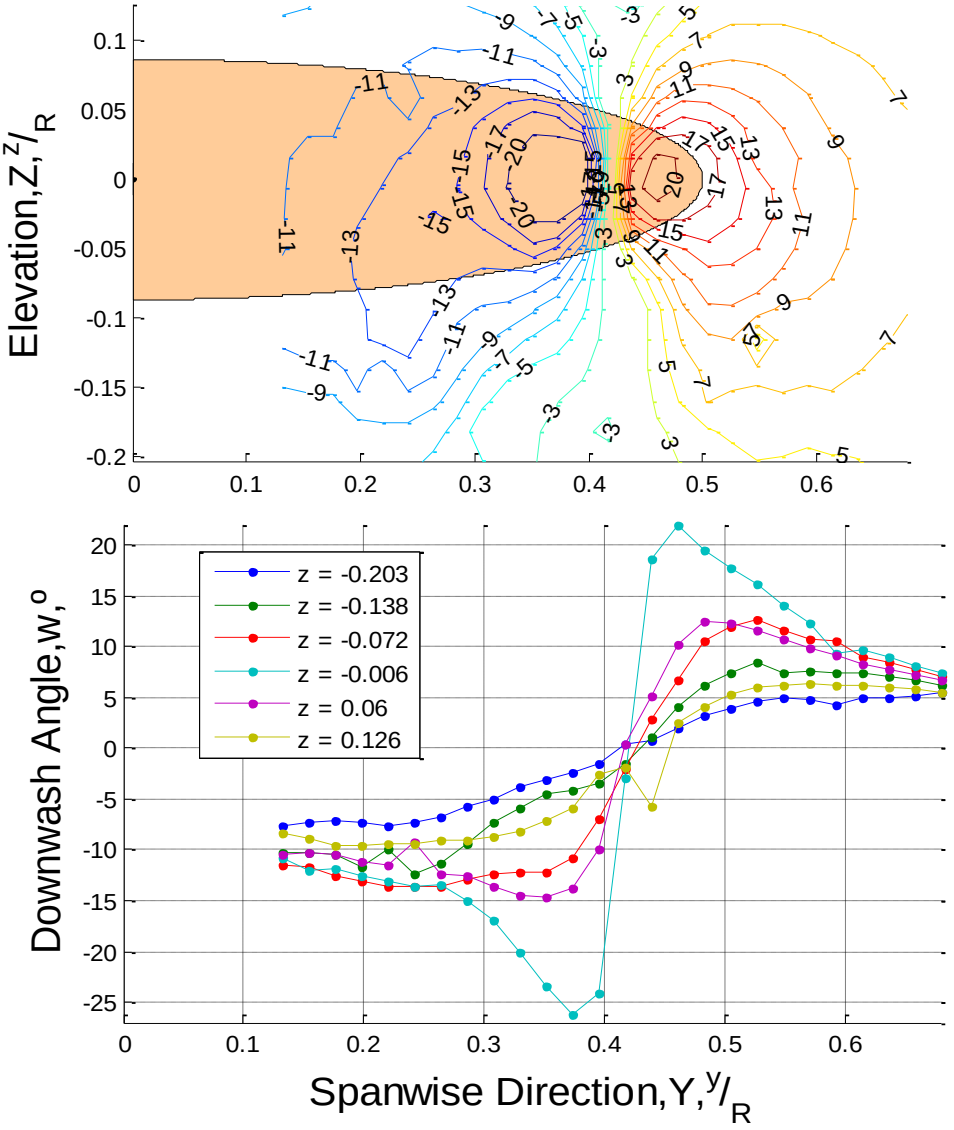

Figure 3-15: Downwash Contours (top) and Downwash Profiles (bottom). One Disc Radius Downstream, 10° AOA, Re = 2x10^6.

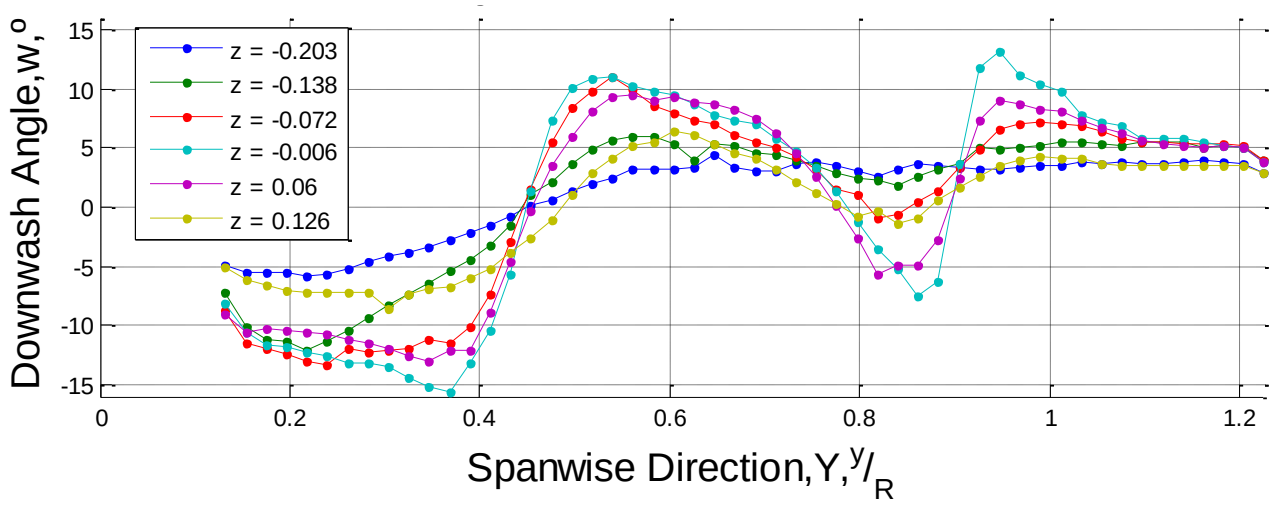

Figure 3-16: Downwash profiles, Blades, 10° AOA, One radius downstream, Re = 2x10^6.

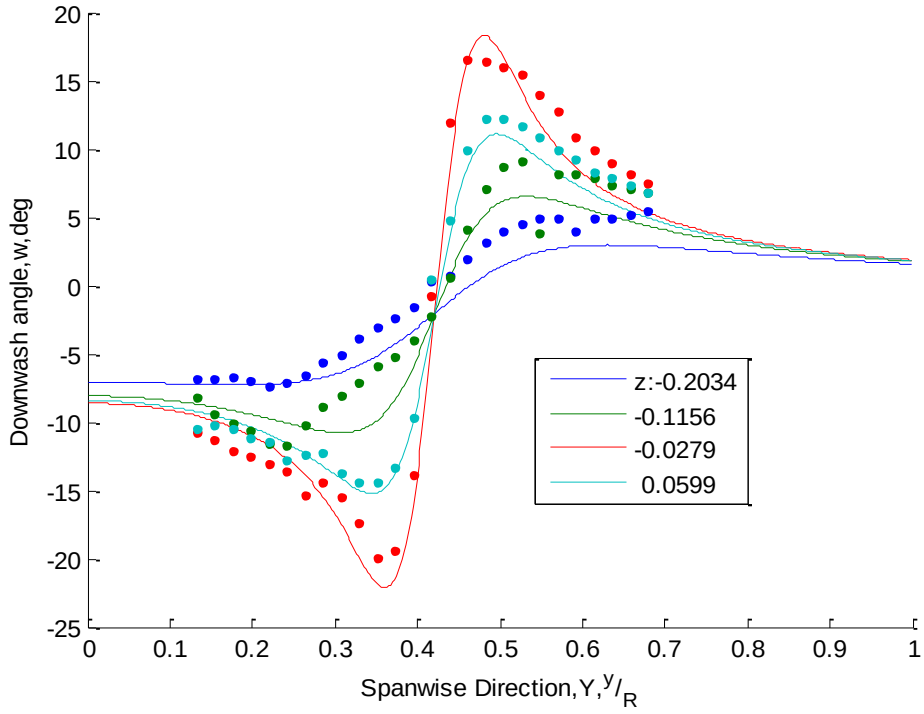

Figure 3-17: Comparison of Measured and Analytically Calculated Downwash Profiles. Measured downwash (points) overlaid on recreated vortex calculations (line). Data for 10° AOA at Re = 2x10^6.

Downwash profiles can be analytically calculated from the vortex strength calculations in the previous section. For the disc alone, we assume two equal and opposite vortices shed near the port and starboard tips of the wing. The vector field can be calculated by superimposing the effects of the two vortices. Similarly, we can do the same for a disc with blades attached.

In Figure 3-17, the vector field has been recomputed using the data in Table 3-2 and the corresponding downwash profiles are shown as solid lines. The points are the corresponding experimental data points used to calculate the vortex strengths. Downstream of the circular wing, vorticity is shed continuously across the wing. The single tip vortex measured is actually the shed vorticity "rolled" around each other appearing as a single vortex. The tip vortex cannot be perfectly represented by a point vortex. The vorticity is actually distributed over some area. This is the reason for error when recomposing the velocity field, however, a point vortex offers a much simpler approach to the problem.

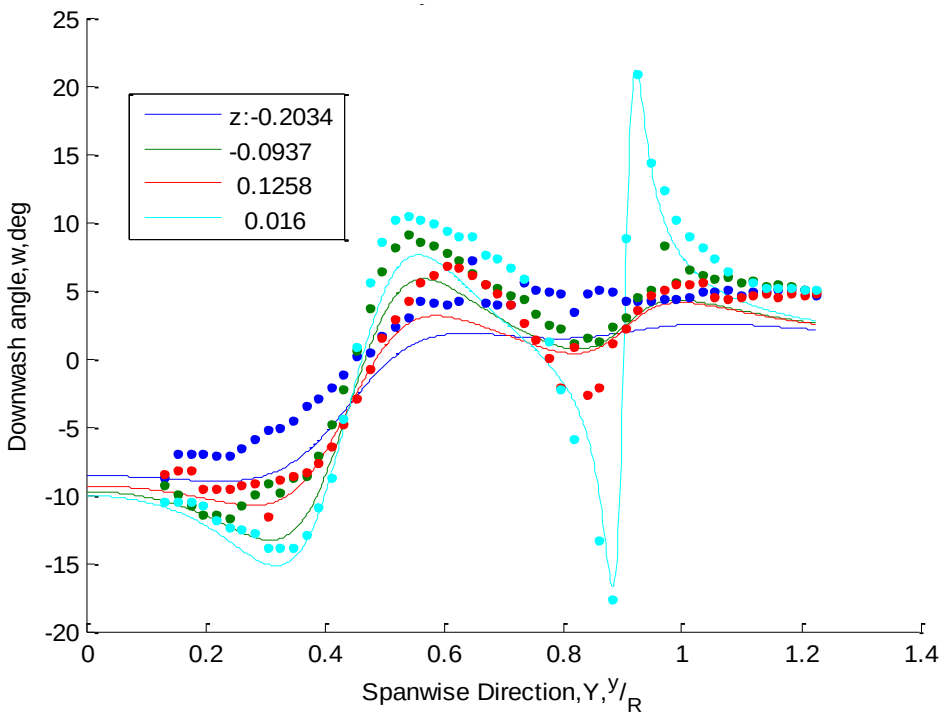

Figure 3-18: Comparison of Measured and Recreated Downwash Profiles, Measured downwash (points) overlaid on recreated vortex calculations (line). Data for blades with 2.4" chord and 8" length, 10° AOA, Re = $2x10^6$.

3-4: Comparison to Prandtl's Finite Wing Theory

Similar results are obtained from a comparison with the analytical solution of Prandtl's equation for finite wing theory for an elliptical chord distribution. The analytical solution may be found in multiple text books and the notation here will be borrowed from *Principles of Ideal-Fluid Aerodynamics* by Krishnamurty Karamcheti. Analytical results are obtained by finding the solution to:

$$\Gamma(y) = \frac{1}{2} a_0(y) c(y) \left[V_\infty \alpha(y) - \frac{1}{4\pi} \int_{-\frac{b}{2}}^{\frac{b}{2}} \frac{\frac{d\Gamma}{dy(\eta)d\eta}}{y-\eta} \right]$$

referred to as the integro-differential equation for the spanwise distribution of circulation where y is the spanwise coordinate, b is the span, $\Gamma(y)$ is the distribution of bound circulation, $c(y)$ is the chord distribution (wing planform), V_∞ is the free stream velocity, $\alpha(y)$ is the geometric angle of attack and η is a coordinate in the spanwise direction used for integration. From the analytical solution for an elliptical planform shape, an elliptic circulation distribution is found. The maximum bound circulation can be calculated as

$$\Gamma_0 = \frac{2\, b\, V_\infty\, \alpha}{1 + \left(\pi\, AR / a_0 \right)}$$

where AR is the aspect ratio. If we visualize the wing as a "horseshoe" vortex, then strength of the tip vortices will be equal to the maximum circulation and the sign will depend upon the side of the wing. The equation requires knowledge of the finite wing's Lift coefficient slope with respect to the angle of attack. The slope for a finite wing can be determined from the following equation:

$$\frac{a}{a_0} = \frac{1}{1 + \left(a_0 / \pi\, AR \right)}$$

where a is the slope of the lift coefficient for the finite wing an a_0 is the slope for a 2D cross section. In above formulation and solution to Prandtl's finite wing theory, it has been assumed that the flow over a spanwise component remains two dimensional. While this remains a fair assumption in high aspect ratio wings, it generally does not hold for low aspect wings. Nevertheless, the simplicity and ease of calculation can outweigh its computational shortcomings.

The above formulas may be combined with the results from the force measurements to estimate the tip vortex strengths for the circular wing. From Figure 3-6, the slope at each angle of attack can be calculated with a second order scheme to obtain the results in Figure 3-19. Using the above equations, the elliptical solution yields the tip vortex strengths at angles of attack of 8º, 10º and 15º of 0.1304, 0.1732 and 0.2983, respectively. Compared to experimentally measured values, this gives an error of 15.7, 13.7 and 3 percent. Similarly for the 0.5 million Re, we find an error of 32, 17 and 19 percent at angles of 2º, 6º and 10º.

It is important to note that Prandtl's theory will not yield the induced downwash as the downwash is not uniform across the wing.

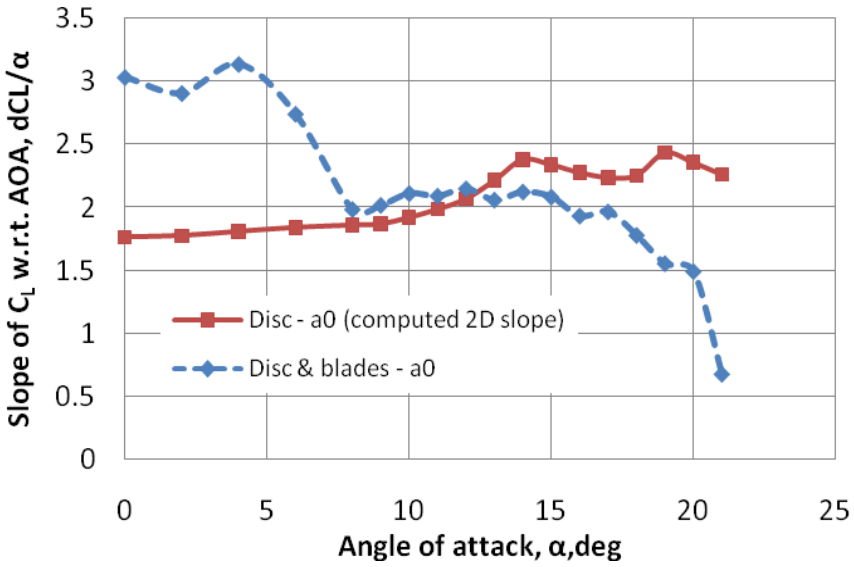

Figure 3-19: Derivative of Lift Coefficient w.r.t. AOA, RE = 2x10^6.
If present, blades have 2.4"chord and 8" length.

It becomes more difficult to apply finite wing theory to a circular wing with blades. An analytic solution is not readily available so the integro-differential equation must be solved numerically. A finite method approach can be found in *Fundamentals of Aerodynamics* by John D. Anderson and is described in the appendix. To validate the solving method, the numeric solution was found to be in exact agreement for the analytical solution at high aspect ratios. This validation is not included in this chapter.

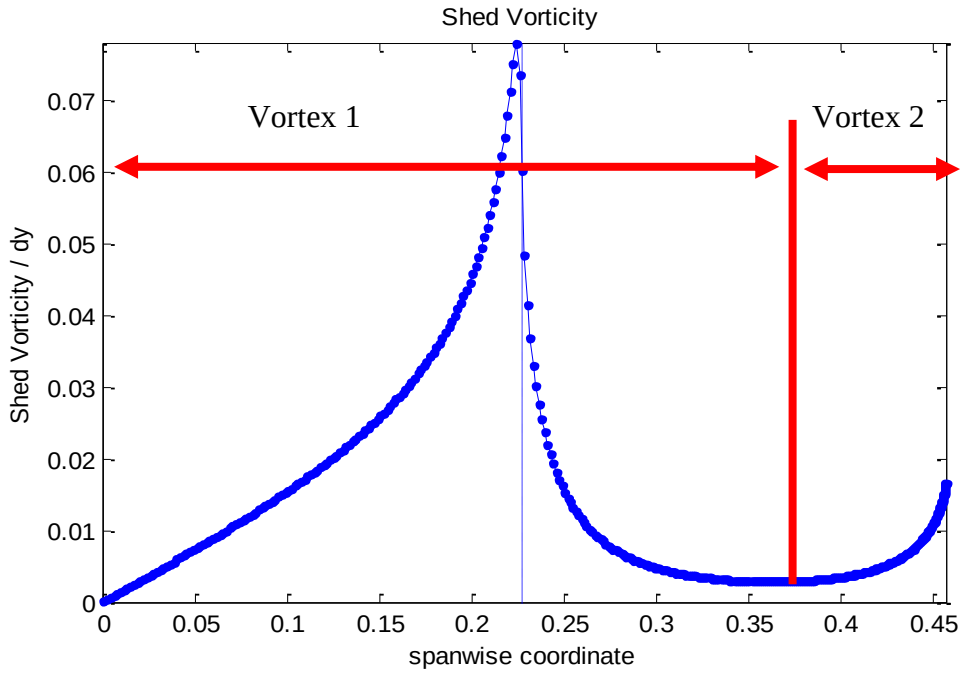

Figure 3-20: Numerical Solution for Vorticity Shed in Spanwise Direction. Circular Wing with Blades of 2.4" chord and 8" length at 10° AOA, Re = $2x10^6$.

In applying finite wing theory to the circular wing, we have assumed the same two dimensional lift coefficient slope obtained above. There will be two vortices present in the wake of the model. Summation of the shed vorticity is performed to estimate the vortex strength. A point is defined at the extrenum of shed vorticity (min or max depending on wing side) between the blade junction and the blade tip. The summation of shed vorticity from the midspan to this point is considered to be the strength of vortex 1 and the remaining outboard vorticity is the strength of vortex 2. This is shown graphically in Figure 3-20.

The estimate vortex strengths from this calculation method yield high relative errors compared to the experimental results. For vortex 1, the errors are 28, 33.5 and 23.6 percent for 8, 10 and 15° at a Reynolds Number of 2 million. For vortex 2, the errors are 23, 21.5, and 2 percent. The numerical solution with blades consistently under predicts the strength by nearly 25 percent at all angles, however, it predicts the relative strengths within 15% accuracy where the relative strength is defined as the vortex strength divided by the total circulation along the wing.

3-5: Conclusions

The aerodynamic forces and wake structure of a circular shaped wing, or disc, with a uniformly rounded edge immersed in a uniform free stream have been experimentally studied in wind tunnel testing. Reynolds numbers of 2 and 0.5 million have been investigated for multiple angles of attack. Aerodynamic forces were recorded via a 6 DOF balance and nondimensional quantities have been reported. Velocities in two dimensional planes perpendicular to the flow were measured by a traversing seven-hole velocity probe at one disc diameter downstream of the wing. The strengths of vortices found in the flow were calculated with three methods yielding the same results. The analytic solution to Prandtl's lifting lines theory for an elliptic wing was able to predict the tip vortex strengths within 15% accuracy, however, it is not a good predictor of the downwash.

To increase performance of the low-aspect ratio disc, blades have been added to the edges of the disc. An increase of 0.17 in the C_L was measured. This substantial increase in performance is due to the interaction between the disc and blades. A numerical solution to Prandtl's lifting lines theory under predicted the vortices' strengths by nearly 25% when compared to experimental values.

4. Hover Flight – DiscRotor Model

A concept for a novel high-speed, VTOL aircraft has been proposed and referred to as the *DiscRotor*. See chapter one for a detailed description of this concept. The concept will emphasize higher-speeds and increased mission radii compared to existing VTOL aircraft. In this section, the aerodynamic forces and wake structure are examined for a novel rotor design. The rotor is composed of a rotating disc with blades extended from its periphery. It appears similar to conventional helicopter rotors except for a large, centrally located disc. This geometry is inspired by interest in its hover characteristics for applications in VTOL aircraft. The addition of the circular disc to the rotor will have advantages as the aircraft increases forward speed.

Tests were conducted to generate basic aerodynamic characteristics of this novel rotor in hover. Because no such rotor exists, the validity of this as a lifting system was a critical design requirement. Small scale tests were conducted on a 3ft diameter rotor without the presence of a fuselage. A "hover rig" was constructed capable of rotating the model at speeds up to 3,500 RPM to reach tip speeds of 500fps. Thrust and torque generated by the rotating model were measured via a two-component load cell, and time-averaged values were obtained for various speeds and pitch angles. To examine ground effects on this rotor, the same hover rig was utilized with the ground simulated with by a movable, solid wall.

Additional pressure and velocity measurements were performed on the model. Thirty pressure taps were instrumented along the simulated ground. Pressure measurements on the disc were performed with a plate instrumented with 16 taps and placing it at the bottom of the rotating model. Experiments were performed to examine the flow field downstream of the rotor by traversing a seven-hole velocity probe. This probe is capable of measuring the three components of velocity as well as the total and static pressures at a point. The aim in this experiment was to understand the structure of the wake which has a large impact on hover performance.

The DiscRotor concept will require blades to protrude from the edges of the disc to hover and attain vertical take-off. The initial concept considers retracting all of the blades for high-speed forward flight and stowing them inside the disc. We consider a method to improve the circular

wing's performance in the previous chapter by simply leaving two blades extended in the spanwise direction, however, one of the blades will be improperly aligned, presenting a sharp leading edge. Reverse Velocity Rotors (RVRs) have symmetric airfoil shapes and therefore have identical lifting characteristics when oriented at 0º or 180º to the free stream (Van Riper). The blades for the present experiment model will have rounded leading and trailing edges to mimic RVRs.

The underlining purposes of these experiments were to aid in the development of the DiscRotor concept. Much of the model's geometry and dimensions were based upon work performed in parallel with the Boeing Corporation. Such a rotor had not been extensively considered in literature and industry; therefore, the rotor had to be established as a valid lifting system. Additional experiment were performed (wake velocity, pressure plate and ground measurements) within the remaining time and budget. This work will not design the actual DiscRotor aircraft, however, the motivation for this study was to provide the required information for the design and analysis of the DiscRotor concept.

4-1: Model Rotor

The rotor can be described as a flat, circular disc from which blades are extended from the edges. During hover and low-speed maneuvers, the disc and blades will rotate together generating lift similar to a helicopter. Therefore blades will require collective and cyclic pitch controls. In the current DiscRotor concept, the blades will be retracted and stowed inside the circular disc during high-speed forward flight. This constrains the length of each blade to be less than the disc radius where the length is defined as the distance from the edge of the disc to the tip of the blade. The blade length was chosen based upon practical design limitations. Blades equal to 90% of the disc radius should allow for the mechanical devices required for blade retraction and pitch controls. Unless noted otherwise, the total diameter (tip to tip) of 2.83 ft was used as the reference length when reducing the data.

Table 4-1: Rotor Model Dimensions

Total Diameter	34in	Blade Length	8in
Disc Radius	9in	Blade Chord	2.4in
Disc Thickness	2in	Blade Thickness	0.25in

Figure 4-1 shows an exploded drawing of the rotor model and the assembled model fixed to the hover rig. The rotor model was fabricated from aluminum in the Mechanical Engineering Machine shop at Virginia Tech. It attaches to a shaft via a central hub which are the two smaller discs shown in the exploded drawing. Both the disc and blades attach directly to this central hub. The disc's shape is created by connecting a large outer ring to two flat plates on the top and bottom. Each blade is composed of two parts, the first is the blade's airfoil shape and the second is a "collective pitch" rod. Each pitch rod has one end cut at a specific degree to create a pitch angle in the blade. These rods can be replaced to attain different collective pitch angles. Four angles of 8, 12, 14 and 16º were prepared and tested. Finally, all of the parts are held together by bolts (not shown in Figure 4-1) passing through the model. In the current study, only the collective pitch of the blades was varied and there was no attempt to include cyclic controls.

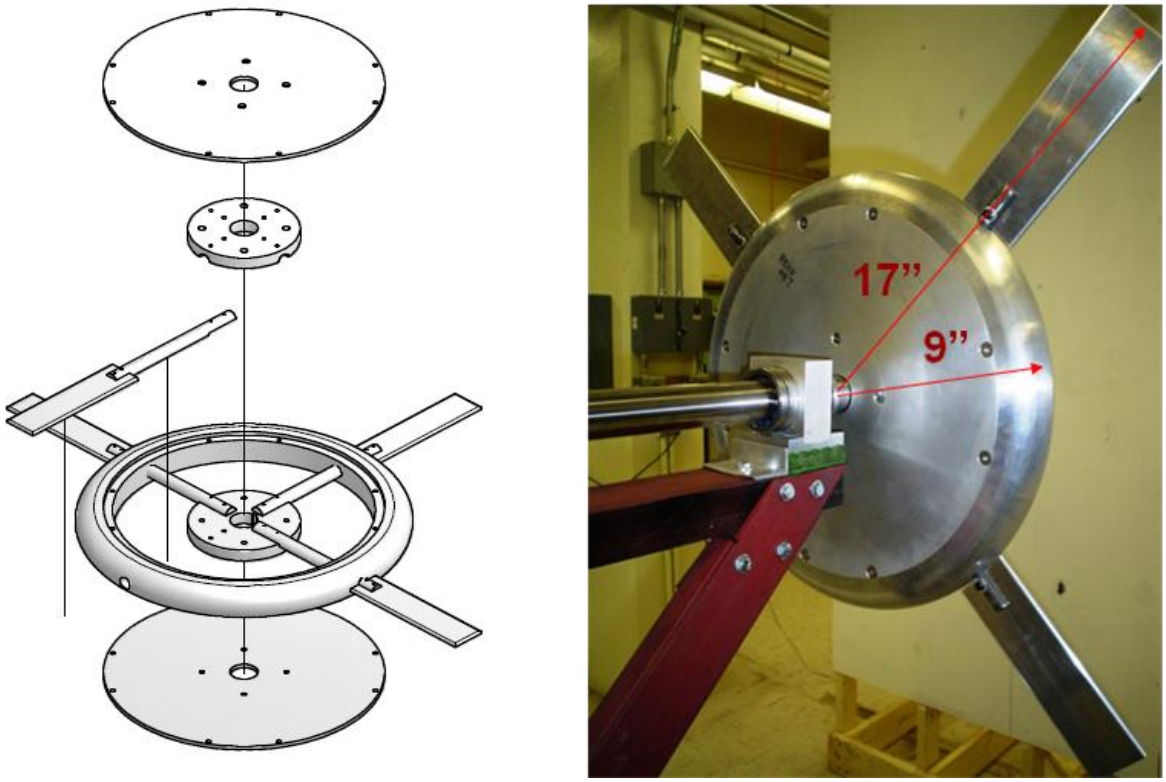

Figure 4-1: Rotor Model Exploded View (Left) and Mounted to Rig (Right)
Disc and Tip Radius Dimensions are Shown in Red (Right).

4-2: Hover Rig

The “hover rig” was designed and constructed in the Fluids Lab located in Norris Hall at Virginia Tech. The goal was to achieve tip speeds up to 500fps (340mph) with the rotor shown in Figure 4-1. The main purpose of the rig was to measure the thrust and torque generated by the model during hover in conditions both near and far from the ground. The forces were measured via a two component load cell while the ground conditions were simulated by a movable wall described below.

The torque and thrust generated by the model while rotating was measured in real-time. A load cell cannot be mounted to a rotating object without using wireless device. These wireless devices can become very expensive and were not an option. Instead, the experimental setup used is shown in Figure 4-2. The model is fixed at one end of a hardened steel shaft while the motor is connected to the other end. A cage around the motor allows for a secure connection to the bi-axial load cell. The weight of the motor is counteracted by a pulley system connected located far above the motor to reduce any experimental error. The entire system is held in place by two Linear-Rotary bearings and the load cell. The bearings allow the torque and thrust to be transmitted through the shaft with minimal friction. In general, the torque and thrust from the model is transmitted through the shaft and motor to be measured by the load via a DAQ system.

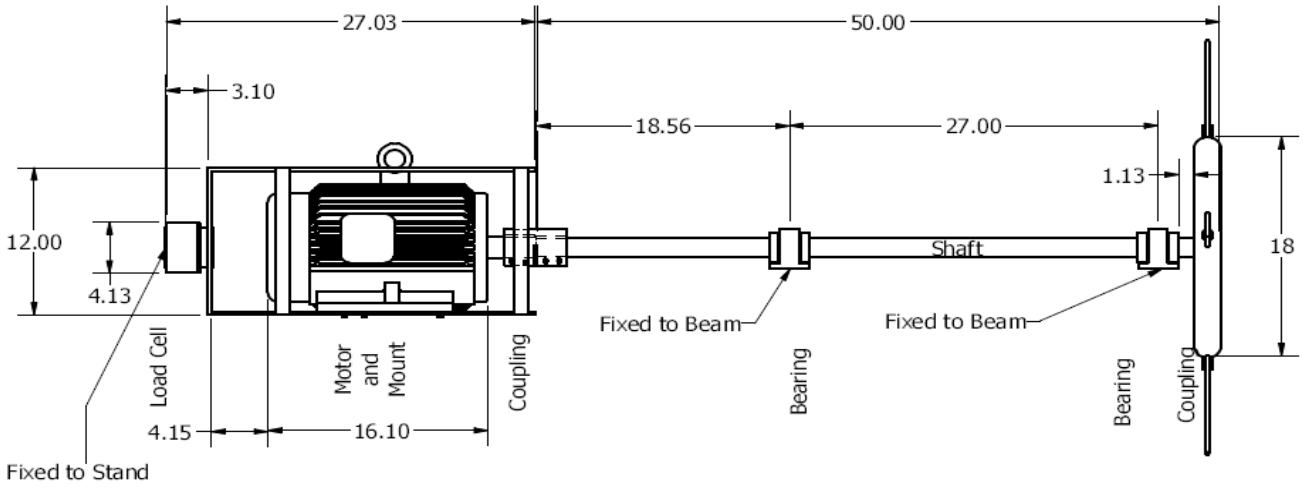

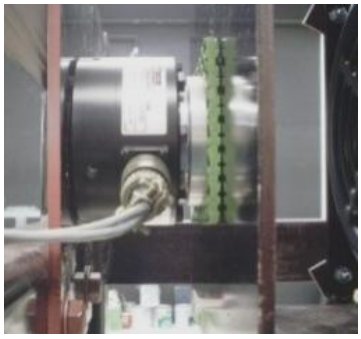

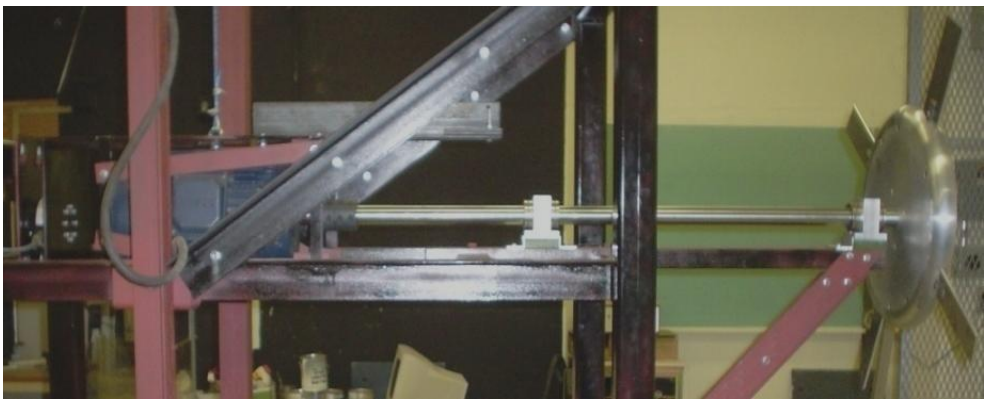

Figure 4-2: Experimental Setup Assembly Drawing (top).
Close-Up View of the Bi-Axial Load Cell (Bottom-Left).
Setup Mounted onto the Hover Rig (Bottom-Right).

A large iron structure was built to secure the testing apparatus horizontally in the room during experimentation. The structure was made by welding a series of "L" beams together. Pressure changes from different elevations may be neglected when performing tests in air. Having the model horizontal allowed for very large distances upstream and downstream of the rotor to be free of obstructions. The ceiling of the room is nearly 12ft and the model was held in the middle. An 8ft by 8ft wall was placed downstream of the rotor to simulate the ground during experimentation. The wall was not fixed in place, and could be moved to examine the effects of ground distance. See Figure 4-3 for pictures and drawings of the hover rig and Figure 4-4 for the placement of this rig in the lab. The 15hp motor was capable of speeds of 1,500 to 3,750RPM and was controlled by a remote computer system. This allowed operators to be a safe distance during experimentation.

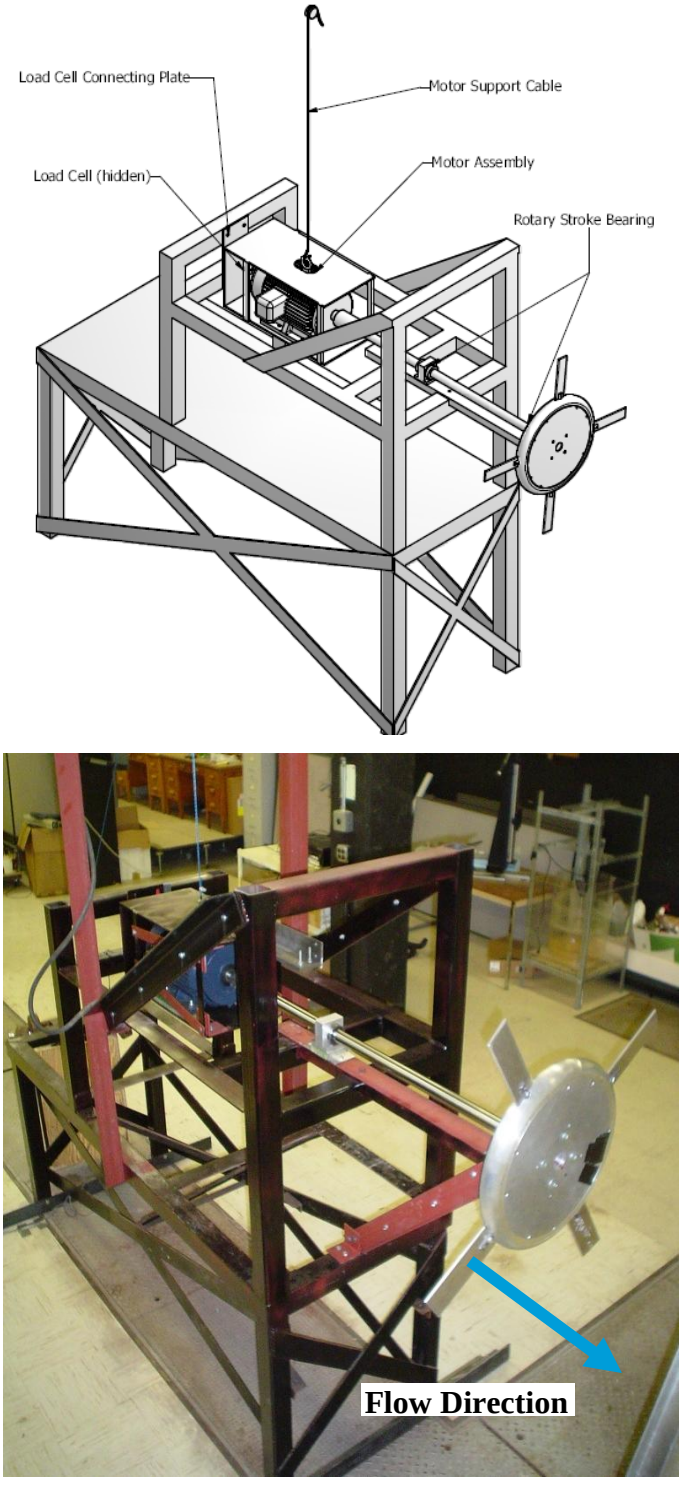

Figure 4-3: Assembly Drawing of Hover Rig (Top) and Picture of Final Rig (bottom)

Figure 4-4: Hover Rig Assembly Location and Movable Wall (White).

4-3: Definition of Symbols and Quantities

We define some common terms used for reducing the data from helicopter aerodynamics and can be found in multiple texts (Leishman). Quick descriptions of these quantities are included for completeness of the experiment results.

The tip plane area, S, is the area traversed by the blades of the rotor. Due to the geometry of the model, we remove the area of the disc from consideration and the tip plane is calculated as

$$S = \pi \left(R_{tip}^2 - R_{disc}^2\right)$$

where π is the known constant, S is the modified surface area of the tip plane, R_{tip} is the distance from the center of the rotor to the tip of a blade and R_{disc} is the radius of the disc. By using this modified tip plane area, we redefine the coefficient for thrust and power as

$$C_T = \frac{T}{\rho S V_{tip}^2} \qquad and \qquad C_p = \frac{Q}{\rho S R_{tip} V_{tip}^2}$$

where T is the thrust force, ρ is the air density, V_{tip} is the tip velocity, and Q is the torque. The solidity ratio is the ratio of area of the blades to the area of the tip plane and is found to be

$$\sigma = \frac{B\, c \left(R_{tip} + R_{disc}\right)}{\pi\left(R_{tip}^2 - R_{disc}^2\right)} = \frac{B\, c}{\pi\left(R_{tip} + R_{disc}\right)}$$

where B is the number of rotor blades, c is the chord of a blade and σ is the solidity ratio. The chord of the rotor blade was chosen such that the model would have a solidity ratio of 0.10 as defined above. The H/D ratio is defined as the distance of the rotor's bottom surface to the ground, H, divided by the total rotor diameter, D (where the rotor diameter is from tip to tip, and in the present case nearly 34 inches). To present pressures, the tip velocity is used to define a quantity similar to the dynamic pressure,

$$q = {}^1\!/_2 \rho V_{tip}^2 .$$

4-4: Load Cell Measurements

The thrust and torque generated by the rotor model was measured during hover. Ideally, any forces generated by the rotor will be measured by the load cell unaffected by the presence of the shaft, bearings, and motor. However, this is not the case. A static calibration, with the shaft fixed in relation to the motor, was performed to determine the sensitivity of the system. To quantify

and remove the dynamics effects in the system, a tare was performed without the model present and was later subtracted from the results.

In performing the calibration, a system of pulleys and weights was used to apply a known thrust or torque on the shaft at the model end. Output from the load cell was measured. The linear-stroke bearings are known to create a small amount of thrust at high rotational speeds due their design. A calibration was performed to quantify and remove the dynamic effects of the bearings.

During the static calibration, the model was removed from the shaft. The shaft was fixed in relation to the motor. A system of pulleys and weights were used to apply a known thrust or torque on the shaft at the model end. Output from the load cell was measured. Strong linear relationships were found for both loads. This calibration was performed after any change to the system such as a change in the pitch angle of the blades. Minor changes were observed and were most likely due to normal wear and tear on the bearings. Although only minor changes were present, a calibration was performed before each test.

To account for the dynamic effects, a tare was performed without the presence of the model. After each calibration, the shaft was rotated to the same speeds and conditions experienced in the upcoming tests. Loads were recorded and averaged with the same procedure as the test results (explained in the following paragraphs). Effects of the bearings were small (<10% of the loads generated by the model). The tare results are subtracted from rotor data to remove the dynamic effects of the system.

After performing the calibration and tare, the model is fixed to the shaft and rotated. Thrust and torque are recorded continuously as the rotational speed is increased and decreased. The speed is held constant for a minute at four RPM values when ramping up and down. These results are shown in Figure 4-5 where the vertical axis is the measured load and the horizontal axis is time. Each point in the plots is an average of the loads over 5 seconds. This was done to reduce effects such as noise and to obtain reliable averages for steady-state values. The plot appears to have a seven (or nine) “steps” where the RPM was held constant. Whenever the RPM is changed, there

is a large increase in torque to accelerate the model and is shown as a spike before each step. A full minute at a single RPM was given to allow ample time for the rotor wake to develop. Finally, the last 30 seconds is used to obtain averaged thrust and torque values at each RPM.

Notice that the thrust being measured at the third RPM step (near 2486RPM) in Figure 4-5. The steady-state values do not appear to be the same when RPM is increasing versus decreasing. This hysteresis-like effect was observed in multiple tests at only this RPM. The exact cause was not determined. It is possible that a low frequency is present in the loads at this RPM value. A low frequency could be caused by the aerodynamics of the rotor or experimental error due to an unknown natural frequency in the hover rig. Despite this discrepancy, the averaged values near 2486RPM follow the same trends compared to the other speeds and are included in the data analysis.

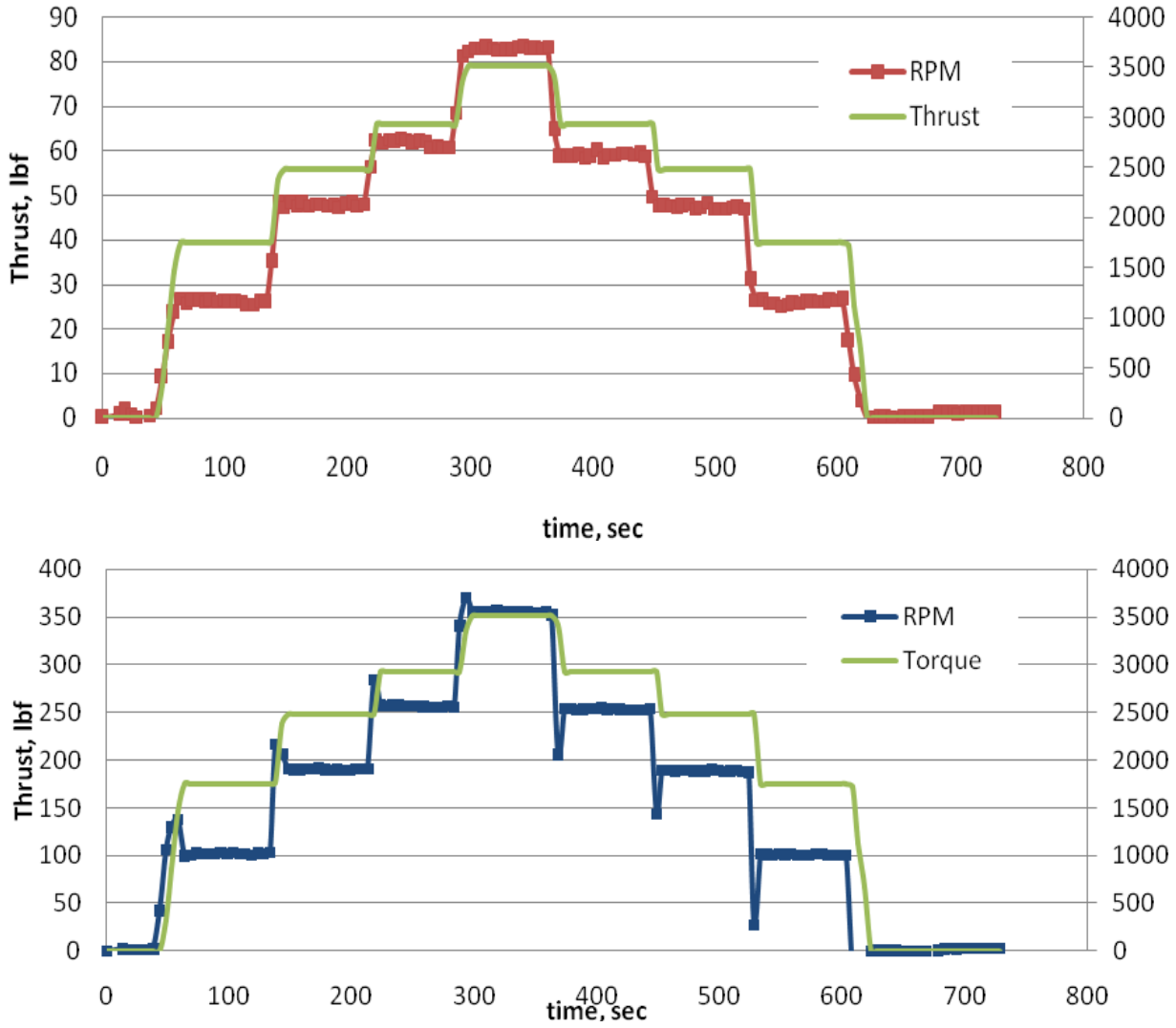

Figure 4-5: Measured Thrust (top) and Torque (bottom) Versus Time.
Each Point is an Average Over 5 Seconds Sampled Continuously.
Lines are Rotation Speed (Green), Thrust (Red), and Torque (Blue).
Data shown for 14º collective pitch angle.

At all speeds, the wake will take longer to reach a steady state when speeds are increasing compared to being decreased. The wake is already established as the speed is decreased and therefore the system requires less time to reach a steady state. Values obtained while the speed is decreasing could be considered a more accurate representation of the steady state. For this reason, however, both values are recorded in this work. Ample time was allowed for the wake to develop and the final value is an average of the increasing and decreasing values. For future

work, averaged values while decreasing the speed would be sufficient for reliable results and shorter time required to perform each test.

The above process was repeated for each pitch angle and ground distance. Results are shown in Figure 4-6. There are four groups of three (a total of twelve) lines where each line connects points with a similar pitch angle and ground distance. The four points on a line are the different rotational speeds. In general, the thrust and power coefficient increases with both the rotational speed and pitch angle. Ground height does not have a significant impact on the power, however, greatly increases the thrust.

From consideration of momentum theory, we find that the ideal power required to generate the slipstream should be related to the 3/2 power of the thrust coefficient. This is a well-known relationship in helicopter aerodynamics, however, it ignores the non-ideal factors such as tip losses and non-uniform flow. A simple method to account for these effects in the presentation of the data is to use the following formula (Leishman):

$$C_p = \frac{k\, C_T^{\frac{3}{2}}}{\sqrt{2}} + \frac{\sigma\ C_{d0}}{8}$$

where C_{d0} is the base drag of a 2D section of the blade airfoil and k is the induced power factor. The last term on the right-hand side is a base power term and often related to the profile drag from the rotor blades airfoil cross-section. An ideal rotor without a disc (ignoring non-ideal effects) will have an induced power factor and C_{d0} of 1 and 0, respectively. For the current rotor model, this base power term will have a significant contribution from the disc as well as the rotor blades. This equation contains no direct consideration for the presence of the disc in the central part of the rotor nor does it consider the ground effects. The parameters C_{d0} and k may be determined from Figure 4-7 where the vertical and horizontal axis have been transformed according to the above equation. Results from the fit of the data are presented in Table 4-2. From the H/D ratio of 3.17, we see high non-ideal effects for the rotor and a relatively high base drag term. While many factors of the rotor are ignored in the simple momentum equation (i.e. effects from the disc), the curve fit matches the data well within the range tested. This equation has been used to present the relationship between thrust and torque.

Using the fits to the simple momentum theory, the thrust augmentation ratio is plotted in Figure 4-8. The thrust augmentation ratio is defined as the thrust coefficient in ground effect divided by the ground independent thrust coefficient for a given, constant, power coefficient. A generally accepted value for the ground independent value is when the ground distance, H/D, is greater than 3. For this work, the H/D ratio of 3.17 is referred to as the ground independent case.

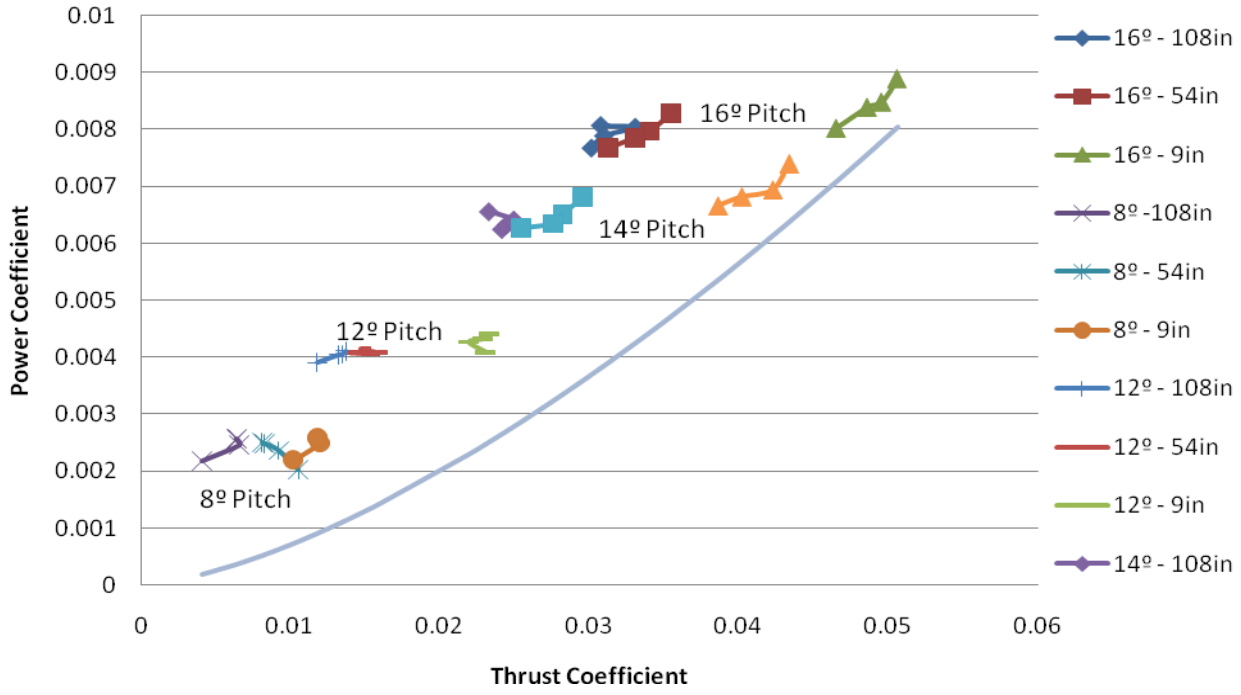

Figure 4-6: Summary of Force Measurement Results.
The Legend Details the Force Results.
Blue Curve is the Relationship for an Ideal Rotor.

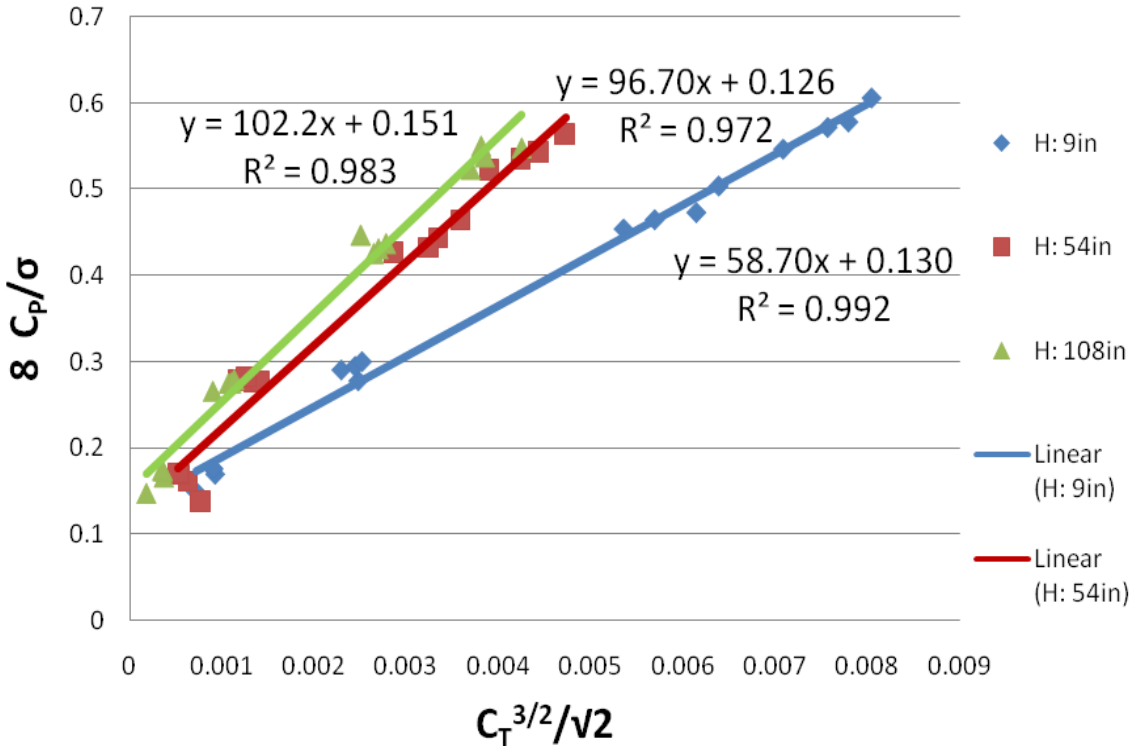

Figure 4-7: Summary of Force Data with Modified Axis. Equations of Fit are Overlaid onto Plot.

Table 4-2: Results from Curve Fit to Momentum Theory.

Ground Distance, H/D	Non-ideal effects, k	2D section base drag
0.26	0.86	0.13
1.59	1.42	0.126
3.18	1.50	0.151

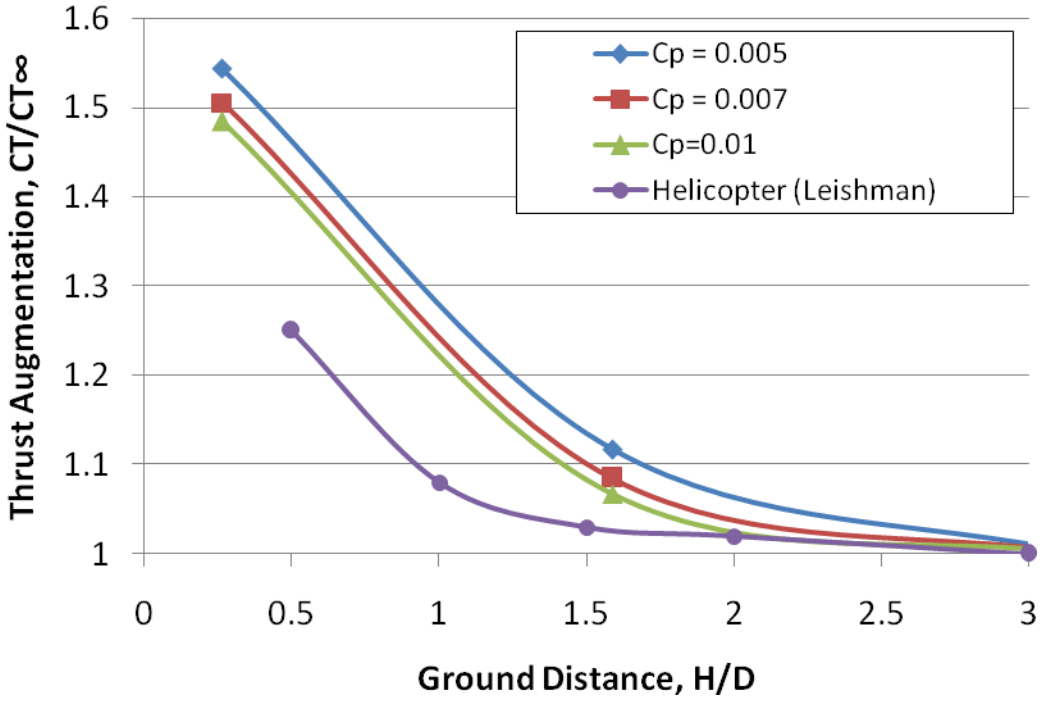

Figure 4-8: Thrust Augmentation Ratio at Constant Power Levels. Comparison made to conventional helicopters (Leishman).

The non-ideal coefficient of 1.5 is high compared to other published values of 1.1 to 1.2 for traditional helicopter rotors. The presence of a disc is not accounted for when determining the non-ideal coefficient. Also, the blade airfoil shapes in the present work are similar to RVRs which perform less-favorably compared to standard airfoils shapes. A comparison is made by plotting the power loading (thrust over power) versus disc loading for various aircraft types (Leishman). The current rotor model studied will require greater power than traditional helicopter rotors to achieve the same thrust.

No consideration was given to increase the performance aspects of the current rotor. The current study focused on understanding the aerodynamics for future work.

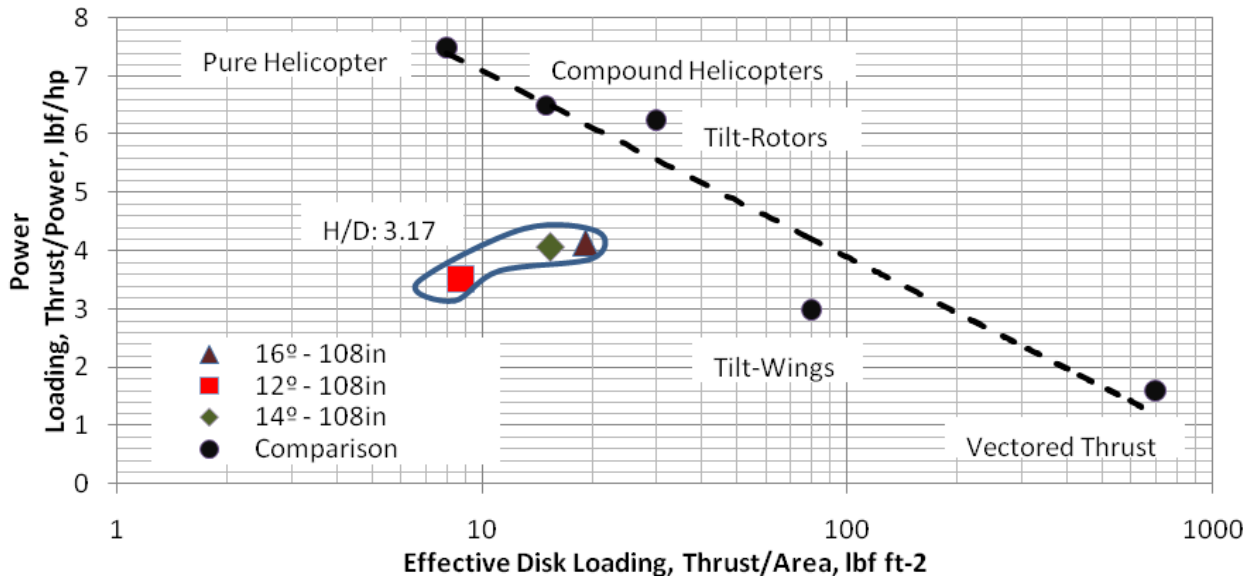

Figure 4-9: Comparison of current rotor model to existing aircraft.
Colored data presented for three collective pitch angles and an H/D of 3 (108 in for model).

4-5: Wake Velocity Measurements

The information about the aerodynamic forces provides a means to estimate the performance but does not provide any understanding of the physical mechanisms creating those forces. Additional experiments were performed to investigate the flow generated by the rotor during hover flight. It was physically observed that the flow downstream of the disc encountered a separated region. Further downstream, this separated region diminishes or "converges" until no longer noticeable. To quantify this physical observation, velocities in the wake were measured by traversing a seven-hole velocity probe in the radial direction and repeated at multiple distances downstream of the rotor. Only a collective pitch angle of 14º and a rotational speed of 2486RPM were considered.

The seven-hole probe measures the three components of the velocity, the total pressure, and the static pressure at the tip of the probe. The probe tip is made from brass, and has seven holes drilled into a conically-shaped tip with a diameter of 1/8". Pressure is measured at each hole with a high-density ESP scanner and the flow properties are calculated. The velocity probe is designed and calibrated by Aeroprobe Corporation.

The velocity probe was traversed along a 20" line of 80 points starting at the center of the disc to beyond the blade tip. This was done by mounting the probe onto a computer automated traversing system powered by a stepper motor. Tests were repeated at multiple distances downstream. To ensure that the rotor's wake was not disturbed by the additional instrumentation, the probe was mounted on a rod. This placed the probe far upstream from the traversing scales. For each point, three seconds of data were recorded and time-averaged velocity vectors were calculated.

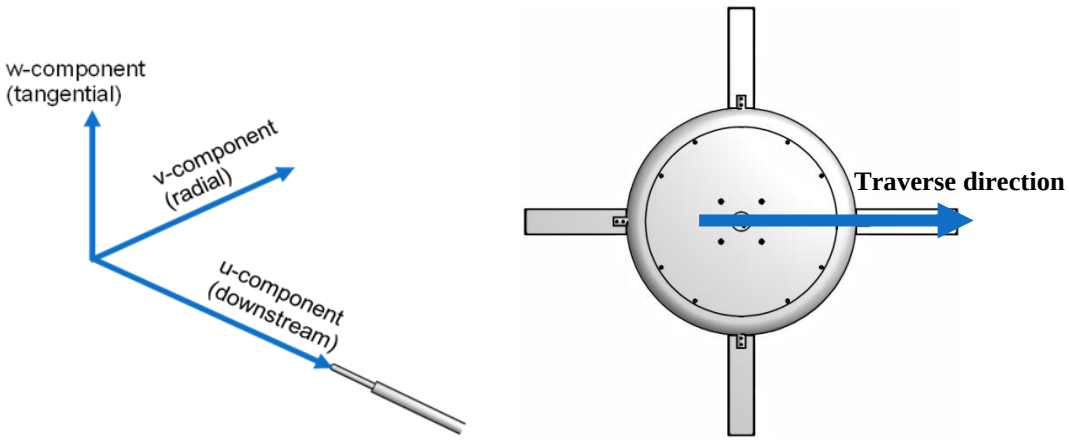

Figure 4-10: Definition of the velocity probe directions for the experimental setup.

The velocity probe used for this experimentation was designed for use in wind tunnels where the flow would be directed not far from the axis of the probe. This system was chosen for the experiments described in Chapter 3. It was not initially intended for hover experiments. Measurements are accurate when the flow alignment is within 70º from the probe axis (Aeroprobe Corporation). When these conditions are not met, the results from the probe are not as reliable. In the region downstream of the blades, there is a large downwash which guarantees this alignment to be appropriate. There is a region of stagnate flow downstream of the disc where velocities are unknown and the probe measurements are not reliable in this region. This is illustrated in Figure 4-11. Despite these conditions, the probe will be able to identify this region of low velocities and provide useful information about the flow.

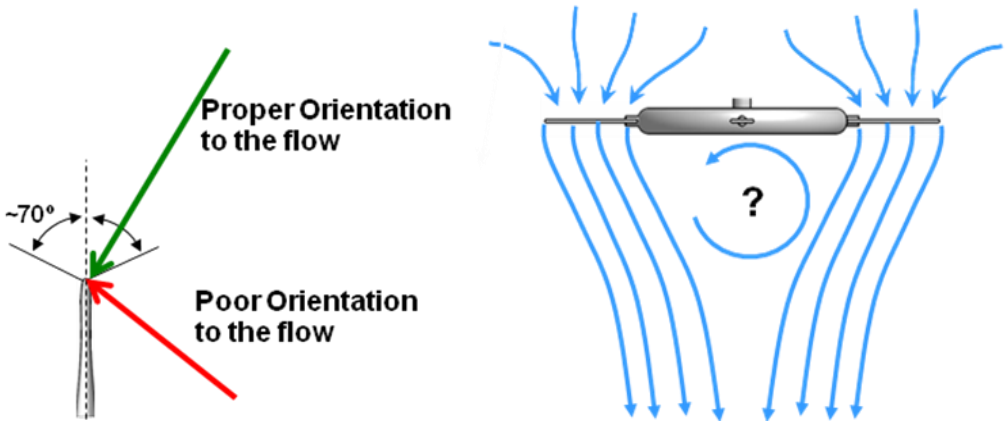

Figure 4-11: Sketch of Flow Alignment (Left) and Flow Field from Rotor (Right). Region Downstream of Disc is Stagnant and Labeled with a "?" (Right).

The flow in the wake of the model was assumed to be axisymmetric. Multiple plots are generated from the data and only the most relevant ground distances are presented in this section. The velocities are labeled as u, v and w corresponding to the velocity in the axial (downstream), radial (positive outward from rotor axis) and tangential (positive in the direction of the blade motion due to rotation). These velocities are plotted in Figure 4-12 and Figure 4-13. The static pressure is shown in Figure 4-14. Not included are plots of the total pressure which may be calculated from the presented data.

Finally, the downwash and radial velocities are combined into a single plot for all distances downstream in Figure 4-15. The symmetry in the flow is assumed and velocity vectors are mirrored about the vertical axis.

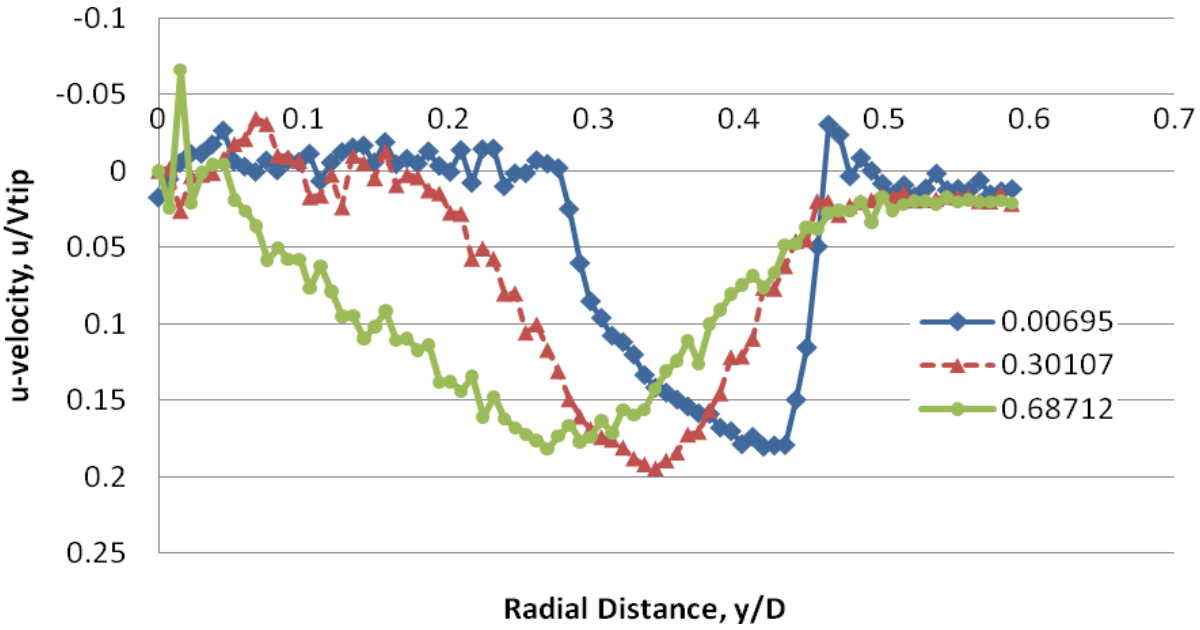

Figure 4-12: Downwash Profiles at Various Distances Downstream of Rotor.
All measurements were for the Ground Independent Case.
Velocity in the Axial Direction.

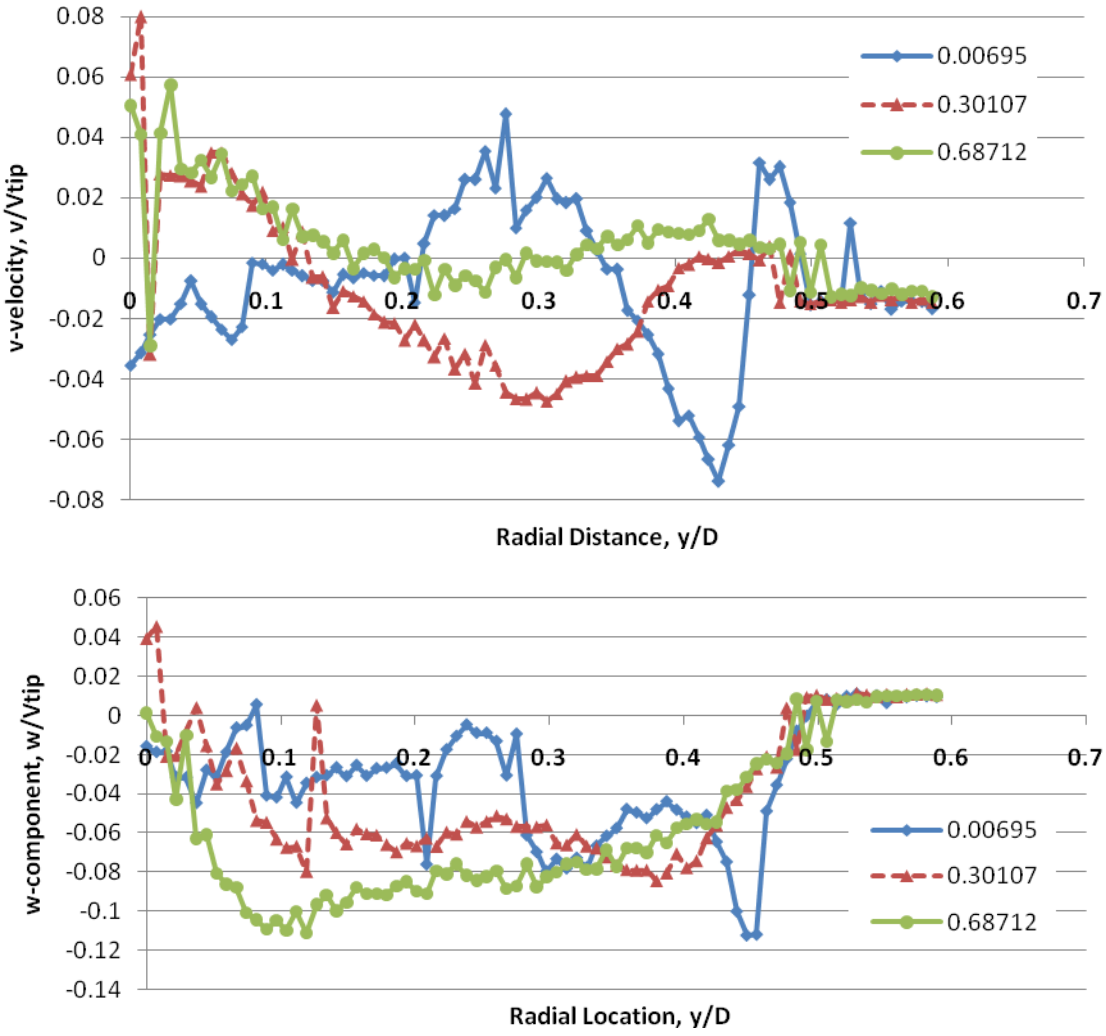

Figure 4-13: Plot of the radial (top) and tangential (bottom) velocities at selected H/D ratios.

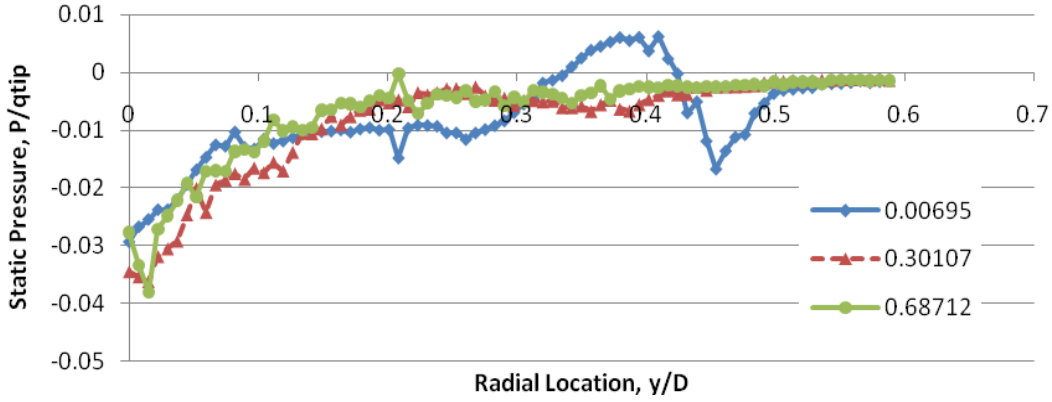

Figure 4-14: Static pressure at selected H/D ratios.

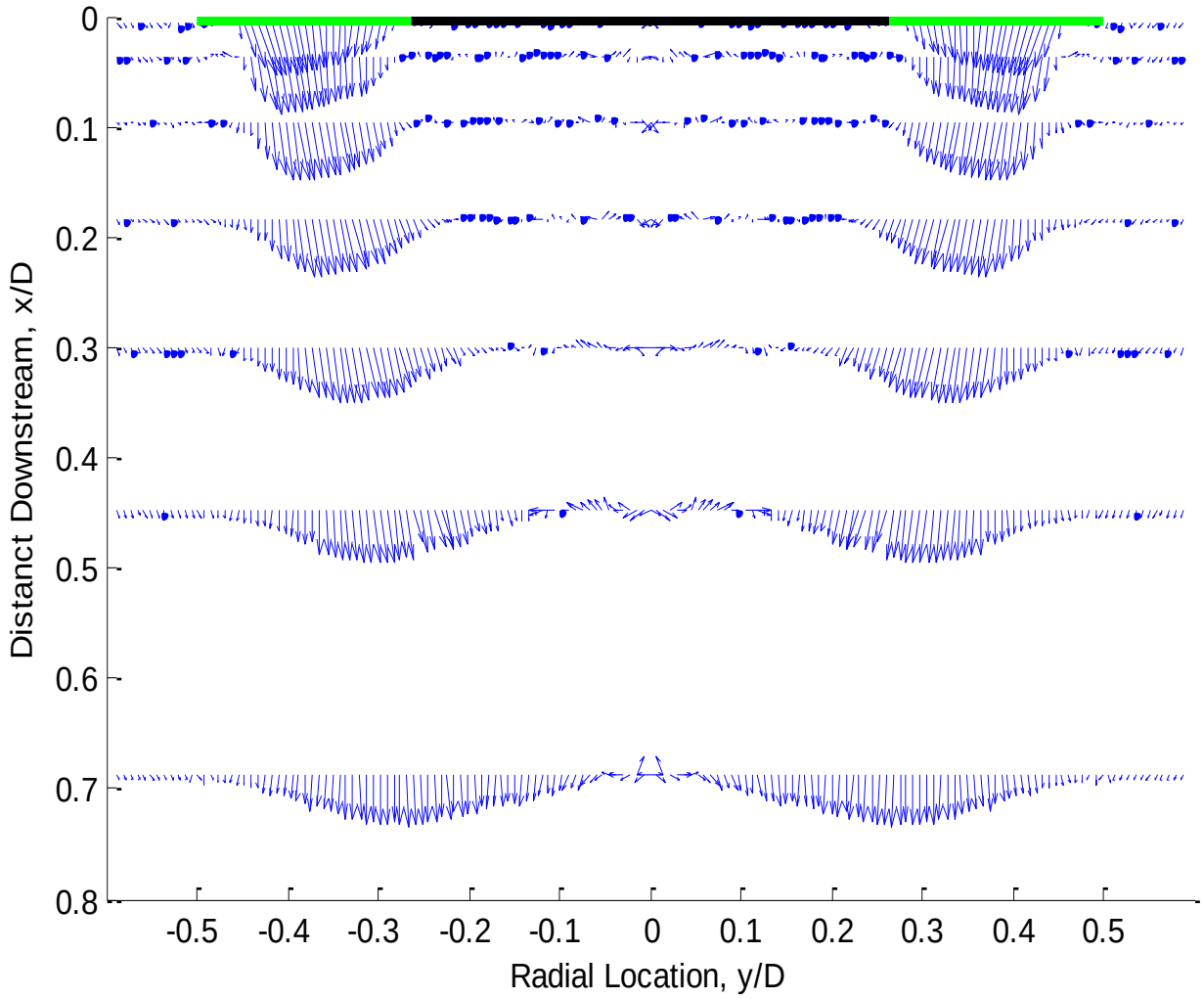

Figure 4-15: Summary of the Velocity Data.
Contains the Downwash and Radial Velocities as Vectors.
Multiple Distances Downstream of the Rotor are Included in the Vertical Direction.
The flow is assumed symmetric and profiles have been mirrored.
The disc is represented by a black line and the green are the tip plane of the blades.

Figure 4-15 contains information from multiple tests and helps to describe the qualitative aspects of the flow field. The other figures provide additional detail and allow for quantitative comparisons. Directly downstream of the rotor blades (in green) we observe a strong, non-uniform downwash seen in the downwash profiles of Figure 4-12 for the lowest y/D ratio. Close to the tip of the blades, the downwash sharply decreases and a slight upwash is encountered at the tip. This is the effect of the tip vortices that develop at the interface of the disc/blades and at the outer tip of the blades. There is a "vortex sheet" shed along the blades' span but this is not easily shown from results of the current experiments. Because of the tip vortices, the downwash is interrupted near the ends, as there is a "tip effect" at both the inner and outer ends of the blade. The rotor generates an annular jet which encapsulates a separated region. This separated region forms because of the presence of the disc which is a solid, impenetrable body.

Flow in the separated region is characterized by low velocities and low pressure. Because of the probe alignment requirements, measurements must be invalidated when the flow alignment is greater than 70º. In Figure 4-16, only the measurements points that are within 70º of the probe's axis are shown. Streamlines are calculated with starting locations originating near the rotor blades. There appears to be two recirculating regions immediately downstream of the blade ends, likely caused by the tip vortices. However, there is not enough information in those flow regions to support unbiased conclusions.

The streamlines shown in Figure 4-16 originate from the blades and none enter into the region downstream of the disc. This is the separated region caused by the disc where velocity measurements are not reliable. It can be seen that the downwash from the blades contracts around this region. Through viscous effects, velocity (momentum) will be imparted to the fluid in the separated region. The measurements are subject to error, however, it provides an understanding of the flow.

Simple momentum theory states that the area of the wake will be equal to one-half the tip plane area (Leishman). (This comes from the conclusion that the velocity in the wake far downstream is twice the induced velocity at the rotor) From study of the streamlines in Figure 4-16 very near

the rotor, there is an initial contraction of the downwash. At the point where the streamlines contract the most the inner, R_{in}, and outer radii, R_{out}, of the wake are 0.27 and 0.445. The area contraction ratio is estimated:

$$\frac{A_\infty}{A} = \frac{\pi\left(R_{out}^2 - R_{in}^2\right)}{\pi\left(R_{tip}^2 - R_{disc}^2\right)} = \frac{0.455^2 - 0.27^2}{0.5^2 - 0.265^2} = 0.695$$

where the symbols are defined before. This is far from the 0.5 expected from momentum theory for three possible reasons: (1) improper spacing of measurement downstream which does not capture the maximum contraction, (2) the presence of the separated region is causing the wake to expand at the same moment or (3) the current assumptions and momentum theory are not valid for this configuration. Additional testing should be performed to more fully investigate the contraction immediately downstream of the rotor.

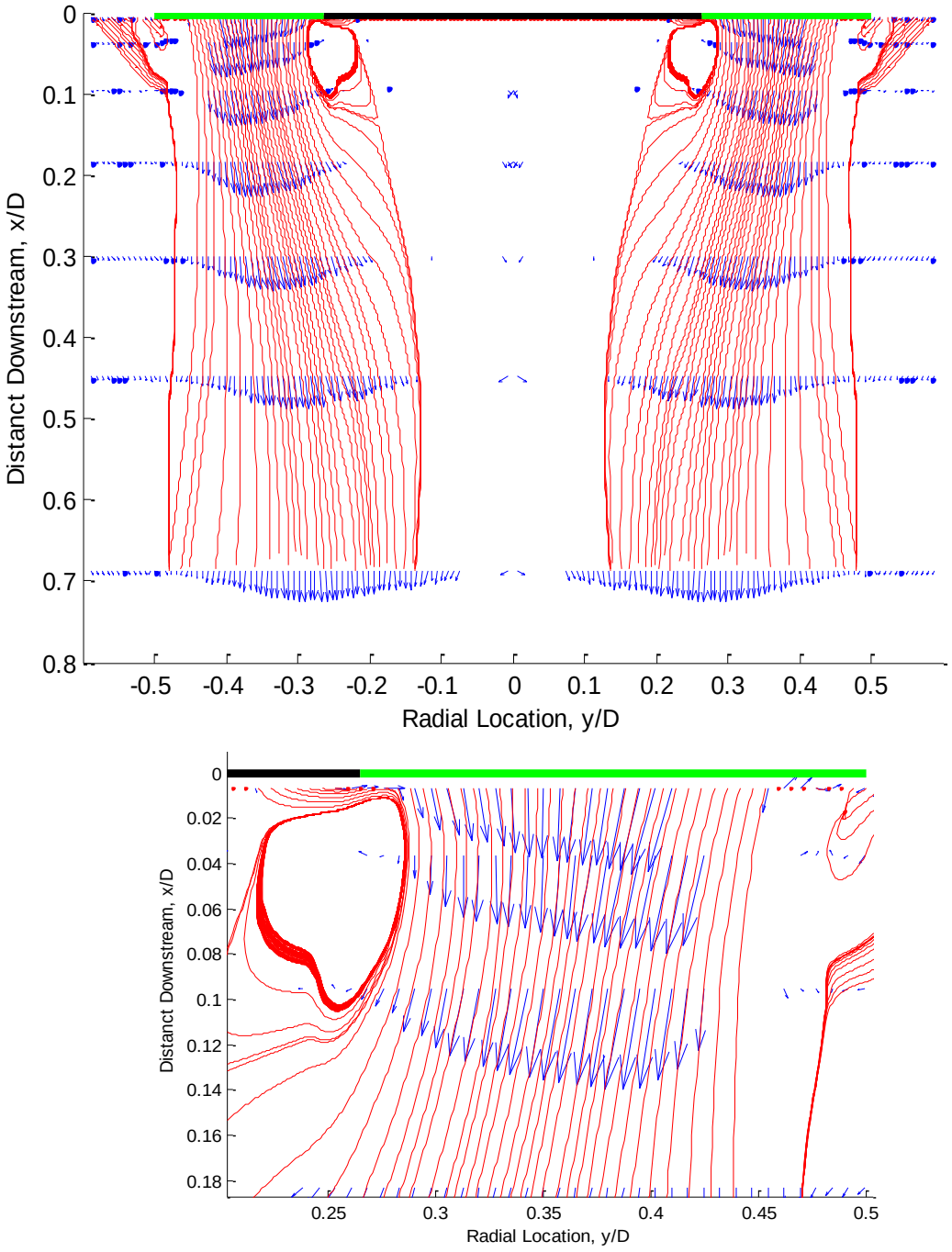

Figure 4-16: Streamline Plots from Velocity Data.
Plot of Streamlines with Misaligned Vectors Removed. (Top)
Close up view of contraction region. (Bottom)
The disc is represented by a black line and the green are the tip plane of the blades.

4-6: Pressure Plate

Results from the velocity measurements raised questions about the pressure on the lower surface of the disc, specifically low static pressures near the downstream surface of the disc. It was not possible to measure the pressure on the rotating disc directly and another method was devised.

A quarter inch aluminum, circular "pressure plate" was constructed and shown in Figure 4-17. It was identical in size to the disc's surface area. Pressure taps were instrumented along the surface of the plate. By building a separate stand, it was mounted close to the rotor with a ¼ in clearance. Ideally, the pressures generated by the flow would not be affected by the pressure plate and measured pressures on the plate would be identical to those on the disc surface.

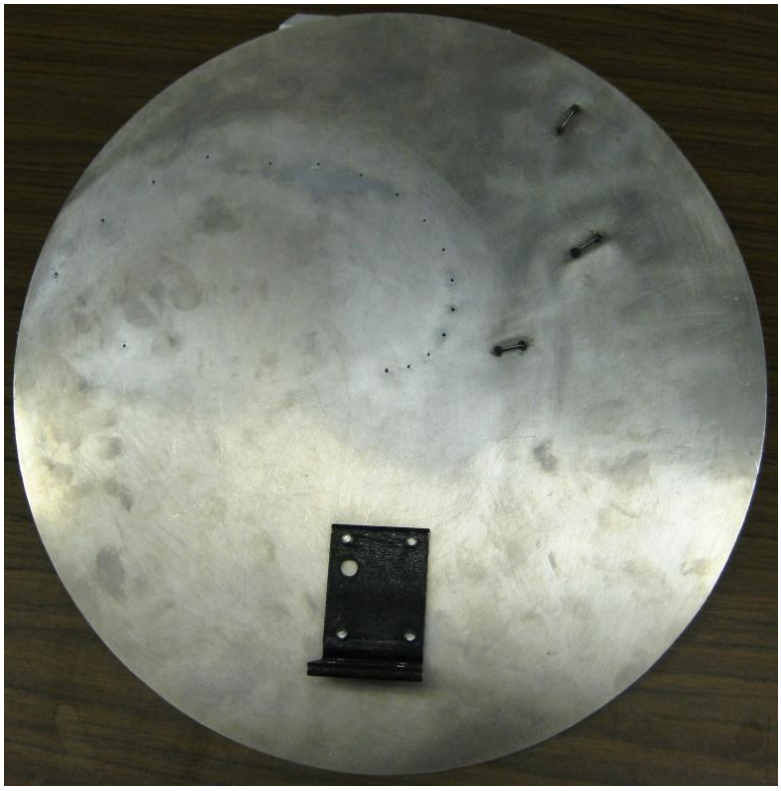

Figure 4-17: Picture of Pressure Plate with Angle (black) for Connection to Stand.

These tests were repeated for the three ground heights and four rotational speeds considered in this work. Results are shown in Figure 4-18. Pressures are reduced by dividing by the dynamic pressure defined earlier using the tip velocity. With the exception of the lowest RPM speed, data collapses into three curves for each ground height where data is reduced in the form of a pressure

coefficient. This shows the pressure distribution on the disc depends upon the rotor's aerodynamics (or more specifically the download).

The ground independent case is the lowest three curves in Figure 4-18. The pressure distribution will be negative on the disc's surface. Close to the disc edge there is a fluctuating pressure distribution likely caused by the inner shed vortex from the blade. Near the center of the disc, the pressure drops significantly due to the large separated region. Near the edge of the disc the same values are found, however, a greater drop in pressure near the disc center was measured by the pressure plate.

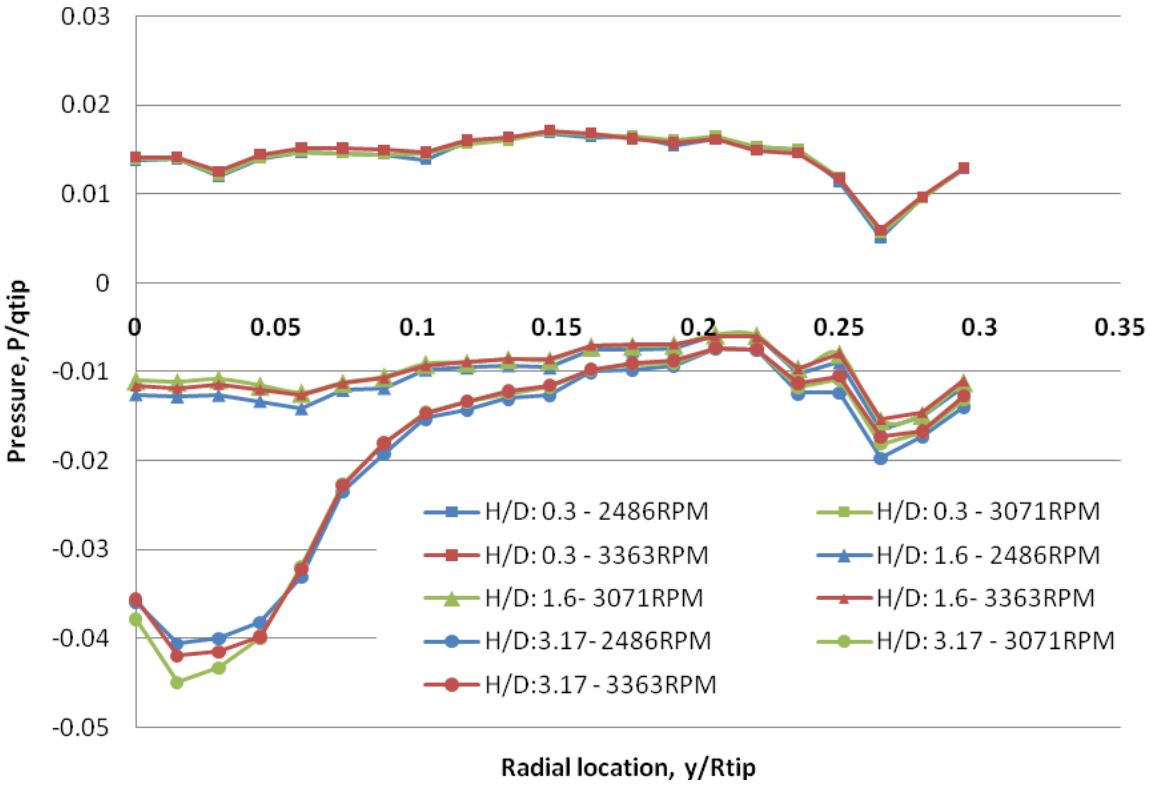

Figure 4-18: Results from Pressure Plate Tests with ¼" Clearance. Repeated for Multiple Speeds and Distances.

The ground effect was also varied with the pressure plate and the upper two sets of curves are shown in Figure 4-18. For the H/D ratio of 1.6, we see very similar pressures near the disc edge but there is nearly no drop in pressure at the disc center. This suggests pressure near the disc center is dependent upon the flow downstream. From Figure 4-8, there is nearly a 15% increase

in rotor thrust at a height ratio of 1.6, which is greater than for conventional helicopter rotors. The change in pressure at the center of the disc would contribute to the increased benefit from ground effects.

At the lowest H/D ratio, the pressure becomes positive and more uniform from the edge to center of the disc. Only three ground distances were considered during this study. The ground effect at this H/D ratio has caused higher pressure which contributes to the relatively high augmentation ratio seen in Figure 4-8.

4-7: Wall taps

Pressure measurements were performed on the simulated ground. Pressures along a line in the radial direction were measured by removing a "slice" from the ground and replacing it with a rectangular plate instrumented with 30 pressure taps. Here the first pressure tap was placed at a point corresponding to the center of the rotor and the last point was placed at the outer edge of the wall. Points are not evenly spaced and are concentrated in regions where high pressured gradients were observed. Tests were performed for multiple rotor speeds but with the same collective pitch angle of 14º. Figure 4-19 shows the hover rig and wall where the pressure taps can be seen on the right side of the wall used to simulate the ground. Results recorded are shown in Figure 4-20.

At this time, velocity measurements could not be performed in the wake in ground effect. However, the pressure measurements along the wall can give information about the flow. The pressure distribution along the wall is similar to the downwash (ground independent case) shown in Figure 4-12 through Figure 4-14. This indicates that the separated region behind the disc does not collapse and a slight expansion of the wake will occur due to ground effects.

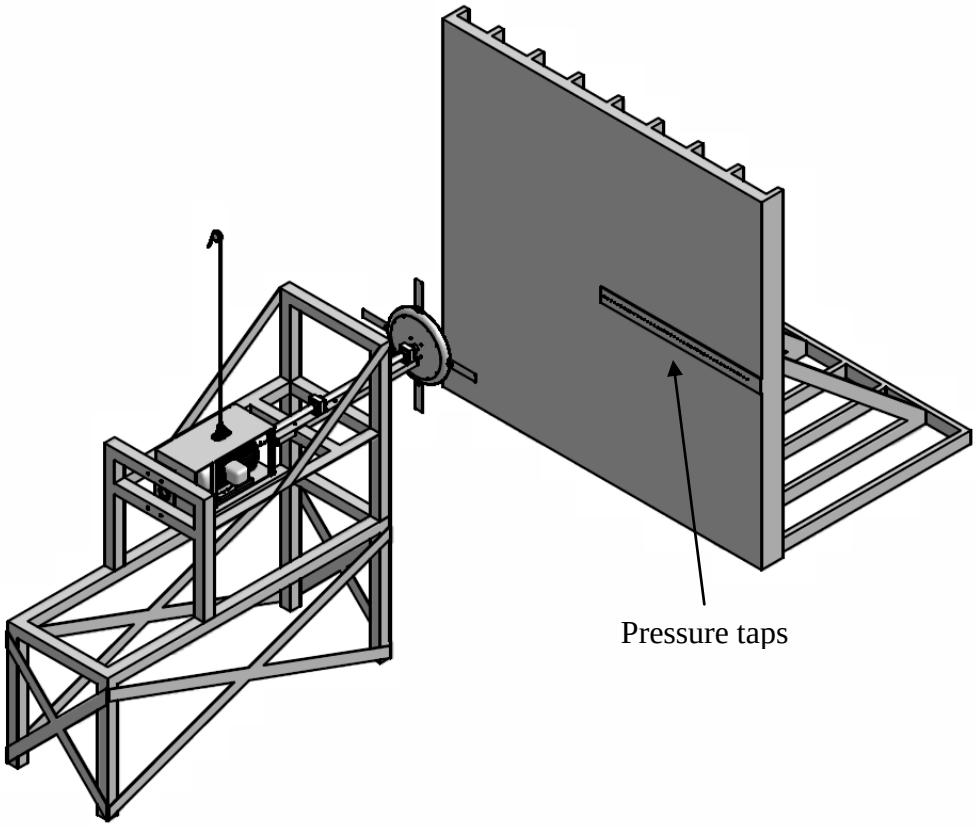

Figure 4-19: Drawing of the hover rig and wall orientation with pressure taps shown.

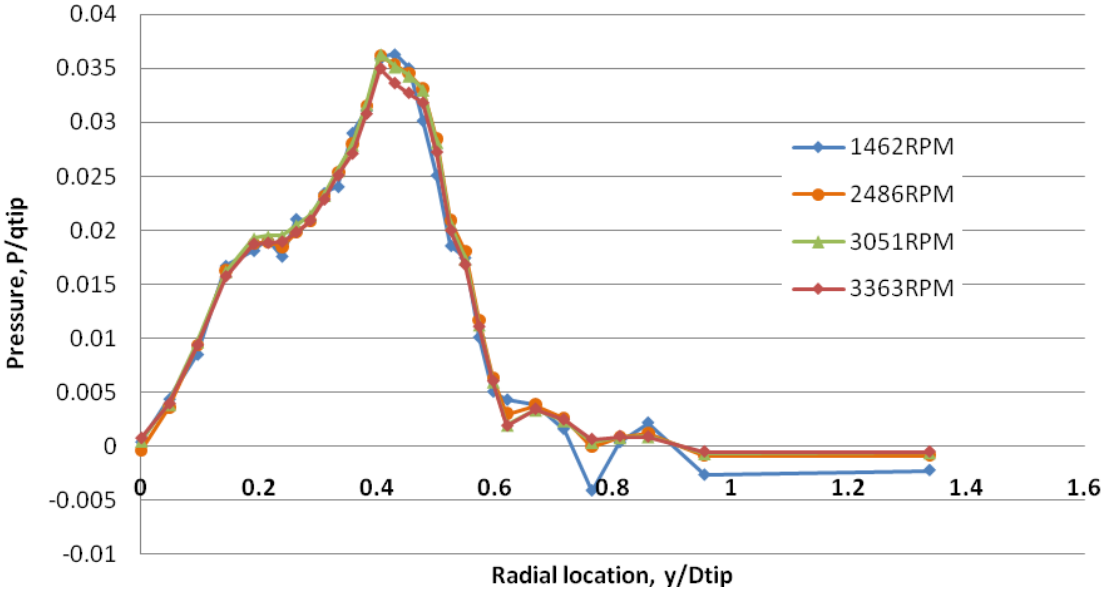

Figure 4-20: Pressure Distribution on Ground for Multiple Tip Velocities. Collective pitch of 14° and H/D of 0.26 shown.

4-8: Conclusions

The aerodynamic forces and wake structure have been examined for a novel rotor design which is a rotating disc with blades extended from its periphery. To measure the forces on the model, a "hover rig" was constructed capable of rotating a model up to 3,500RPM and achieving tip speeds above 500fps. The thrust and torque from the model were measure via a two-component load cell. Results follow expected trends from momentum theory but show high non-ideal effects due to the disc and blade airfoil shape. Pressure and velocity measurements were performed in the wake of the model. Immediately downstream of the rotor, a region of "dead air" (low pressure and low velocity) was found due to the presence of the disc. Moving downstream, the wake was shown to collapse upon this dead air region. The pressure along the disc surface was shown to increases greatly in ground effects, contributing to high Augmentation ratios with a maximum measured to be nearly 1.5 for an H/D of 0.3.

5. Works Cited

Aeroprobe Corporation. AeroAcquire Manual. Multi-Hope Probe Manual. Blacksburg, VA: AeroProbe , 2007.

Anderson, John D. Fundamentals of Aerodynamics. McGraw-Hill, 2001.

Boeing V-22 Osprey Backgrounder. "V-22 Osprey Backgrounder." July 2008. www.boeing.com. 20 Jan 2009.

Darcy, Jamie. navairCV-22_aerial_35. 20 Jan 2009 <http://www.boeing.com/companyoffices/gallery/images/military/rotorcraft/v22/navairCV-22_aerial_35.html>.

Devenport, William, et al. "Virginia Tech Stability Wind Tunnel." January 2009 <www.aoe.vt.edu>.

Espinoza, Oscar. V-22 Osprey -- 070427-N-0841E-011 . 27 April 2007. 20 Jan 2009 <http://www.boeing.com/companyoffices/gallery/images/military/rotorcraft/v22/070427-N-0841E-011.html>.

Hirschberg, Michael. "An Overview of the History of Vertical and/or Short Take-Off and Landing Aircraft." 2000. International V/STOL Historical Society . 20 Jan 2009 <http://www.vstol.org/>.

Imber, Robin D and Ernest O Rogers. "Investigation of a Circular Planform Wing with Tangential Fluid Ejection." American Institutue of Aeronautics and Astronautics (1996).

Karamcheti, Krishnamurty. Principles of Idel-Fluid Aerodynamics. Malabar, Florida: Krieger Publishing Company, 1966.

Leishman, J. Gordon. Principles of Helicopter Aerodynamics. Cambridge: Cambridge University Press, 2006.

Rulan, Jose. The Aerodyanmics of Low Sweep Delta Wings. PhD Thesis. Blacksburg: Virginia Tech, 2008.

Spiers, Dean. Full Long Arm Calibration for the FF-11VT. Calibration Report. NASA Langley Research Center. Hampton, Virginia, 2007.

Stroub, Robert H. Introduction of the M-85 High-Speed Rotorcraft Concept. NASA Technical Memorandum 102871. Moffett Field: Ames Research Center, 1991.

Swanson, Stephan M. and Robert H. Stroub. "AIAA Low-Speed Cruise Aerodynamics of the Stopped Rotor/Disk Rotorcraft Concept." American Institue of Aeronautics and Astronautics (1991).

Talbot, P., J. Phillips and J. Totah. "AIAA-90-3297 Selected Design Issues of Some High Speed Rotorcraft Concepts." AIAA (1990).

UH-60A Blackhawk. 20 January 2009 <http://tech.military.com>.

"V-22 Osprey Pocket Guide." 2007. 20 January 2009 <http://www.bellhelicopter.com/en/aircraft/military/pdf/V-22_64214_pGuide.pdf>.

Van Riper, Steven G. "Investigation of Increased Forward Flight Velocities of Helicpters Using higher harmonic Stall Control and Reverse Velocity Rotor Concept." MS Thesis. 1991.

"VSTOL Wheel of Mis-Fortune." International V/STOL Historical Society . 20 Janurary 2009 <http://www.vstol.org/wheel/>.

Appendix A: **Velocity Probe and Pressures System**

To extract useful information about the wake behind the model, the velocities in a two-dimensional plane were measured experimentally using a seven-hole probe. This probe measures the three components of the velocity, the total pressure, and the static pressure at the tip of the probe. It does this by measuring the pressure with an Electric Pressure Scanner (ESP) at seven holes place around the tip of the probe. From an extensive calibration, the velocity at the pressures can be computed. The velocity probe is designed and calibrated by Aeroprobe Corporation. The required instrumentation and programming were also purchased from Aeroprobe Corporation. For additional information about this system, see the most current manuals and files provided by Aeroprobe Corporation.

A-1: Seven-Hole Probe

A convenient way to obtain velocity measurements within a flow field is through the use of a flow measurement probe. A 7-hole probe, produced by the Aeroprobe Corporation was used to take velocity measurements. Multi-hole probes can measure all three components of the velocity, the total pressure, and the static pressure at any given point. The probe is constructed from several different machined parts and then assembled. Appendix Figure A-1 shows the external geometry and components of the probe. The probe tip is made from brass, and has seven holes drilled into it. The probe used for this research had a tip with a conical shape and a diameter of 1/8”. The same probe diameters have been used in similar research. The first extension is the same diameter as the probe tip and its length was approximately 20 probe tip diameters long. To increase the overall length of the entire probe, a ferrule and second extension are added. The diameter of the second extension was about 1.5 times that of the tip. The larger diameter of the second extension gives the probe structural rigidity. The overall length of the 7-hole probe used was 6”.

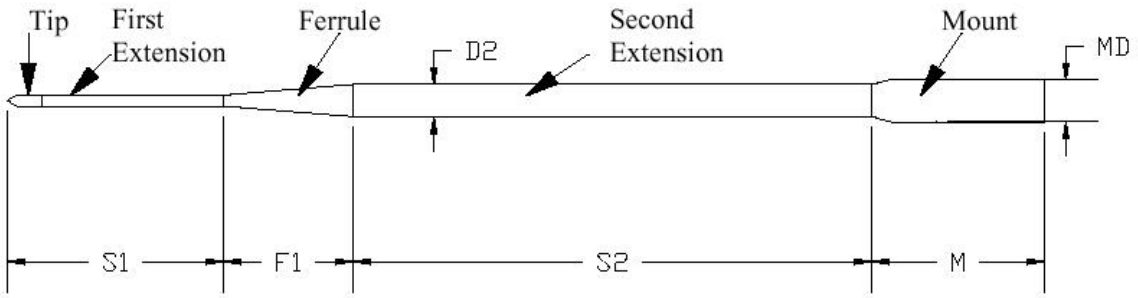

Appendix Figure A-1: External Geometry of the seven-hole probe.

At the end of the probe, there is a brass mount. The shape of the mount is hexagonal, allowing it to be mounted into a collar with the same shape cutout, and then secured with a setscrew. Each of the holes in the probe tip leads to a stainless steel tube, with its inside diameter matching the diameter of the holes. As the probe shaft diameter increases, each tube is telescoped into a larger tube, which finally protrudes from the back of the mount enabling the connection of flexible Tygon tubing. Each connection is soldered and tested for strength and leakage. The final assembly is also tested for pressure "cross-talk", i.e. pneumatic communication between two or more probe holes and their associated tubing. Appendix Figure A-2 presents structural details of a typical probe tip and sample dimensions for a 0.125" (1/8") tip diameter probe tip.

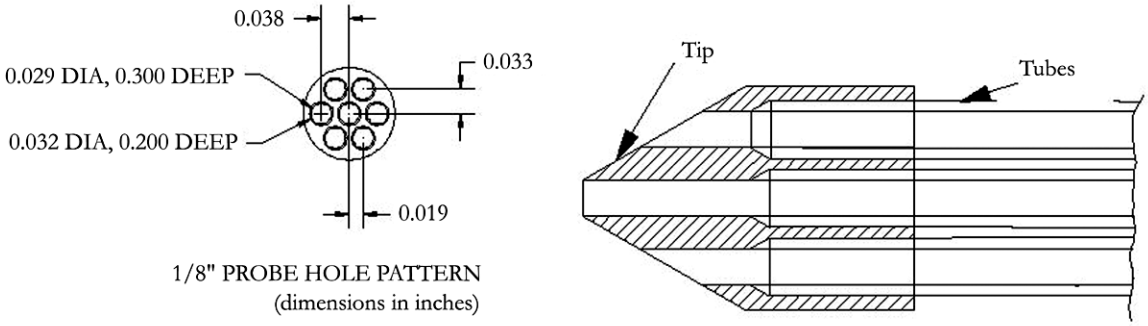

Appendix Figure A-2: Seven-hole probe tip and tubing dimensions.

Because no two probes are identical after fabrication, and because small amounts of damage can occur to the probe over time, it must be calibrated to provide accurate results. The calibration procedure performed was previously developed by the Aeroprobe Corporation and involves placing the probe into a known flow field and rotating the probe through many different angles while acquiring data. The principle idea of operation

is the following: The pressure over a bluff body is the highest at the stagnation point and lowest near separation. If the flow direction forms small angles with the axis of the probe (below 2°), the center hole registers the highest pressure. If however, the flow is steeply inclined with respect to the probe then one of the peripheral holes on the windward side of the probe tip registers the highest pressure, while on the leeward side of the probe, the flow is separated. The pressure information provided by the three holes in the separated region is not used. This type of careful calibration allowed the instrument to measure the direction and the magnitude of the velocity accurately.

A-2: Pressure Scanner and DAQ

To obtain actual velocities from the probe, several pieces of equipment must be used in addition to the probe itself. Tygon tubing was attached to the leads of the probe. While this sounds simple, it was important to label the ends of the tubing to determine which tube went to which port of the probe. The tubing was then connected to a Pressure Systems ESP (model ESP-32HD). The ESP is a compact device containing multiple pressure transducers; each transducer converts an applied pressure to a voltage. This particular ESP model contained 32 separate ports with a usable pressure range of ±10" of water. The first seven ports were connected to the seven Tygon tube leads from the probe. The eighth port on the ESP was connected to the total pressure side of the wind tunnel pitot tube. Finally, the static pressure from the pitot is used as the reference pressure for all eight pressures. This enabled the measurement and recording of the wind tunnel velocity at the same instant data were recorded from the probe, important for the nondimensionalization of velocities to compare test cases later. To interface the ESP to the data acquisition board in the computer an Aeroprobe Corporation system was used.

A Measurement Instruments CIO-DAS08/AOL data acquisition board was installed into the computer system used for data collection. This board has eight 12-bit differential ended analog inputs. Using differential inputs reduces errors caused by such factors as electromagnetic interference or radio frequency interference. Before installing the board into the computer, InstaCal (initialization software provided for the board) was installed. The D/A range for the board was set to ± 5 volts. During the data acquisition process, the

pressures acquired with the probe and ESP were reduced to velocities using Aeroprobe's built in velocity reduction software.

Once the acquisition system was designed and assembled, obtaining useful data depended on its correct implementation. Specific parameters such as sampling rate, period, and spatial resolution were considered during data collection. Several types of tests were conducted, each requiring slightly different acquisition of data. Regardless of which test was performed, the time requirement to acquire all the data was large. Before each test, a long time history of data (either forces, pressures or velocities) was obtained for a sample point. From computing the spectrum of the sample history, the lowest frequencies were identified. The record length was at least 20 times the lowest frequency and an average was obtained. In most cases, the record length was far greater but the 20 was a minimum requirement for all tests. Due to the limitations of the ESP and velocity probe system, the upper limit of the frequency response was only 50Hz. Although this was well below the maximum frequencies expected, an accurate sample average could still be obtained by increasing the acquisition time duration significantly. By using an acquisition time orders of magnitude longer than the lowest frequency's' period, any aliasing of the data could be compensated for. Although this is method does not avoid aliasing, the extremely long acquisition time period will help to reduce its effect. Probe data were taken at 512Hz for a period of four seconds for a single point.

A-3: Traversing System

In multiple experiments, either one or two traversing scales were used to move the probe and acquire data at multiple points. Each scale was powered and controlled by a stepper motor rotating a threaded rod. Depending on tests, different scales are used but operate in identical manners where the only difference was size. The Aeroprobe system includes hardware that interfaces with the ESP and motor controllers to drive the stepper motors used for the 3-axis probe traversing scales. The software system allowed for the input of a user defined grid to traverse points. These scales allowed the probe to be moved to the desired locations in the downstream flow field. In some cases, the motors can "skip"

causing the spacing and accuracy of the scales to be compromised. This is caused by friction in the scales being too great for the stepper motor to overcome and can be remedied by reducing the traversing speed between grid points. When skipping occurs, the scales will not return to the original starting position. The start and end positions were check for every test case.

As was mentioned, acquiring data with a velocity probe required a significant amount of time, and was an important limiting factor. Once the minimum sampling rate and time was chosen, the total acquisition time was only dependent on the time required to traverse the positioning motors plus the time required to acquire and save data for each grid point. To keep tests to a reasonable amount of time, the number of data points in each plane of interrogation could not be too large. In contrast, too coarse a spatial resolution of grid points would increase the error of during post processing of the data. Errors due to spatial resolution were unavoidable and should be considered when examining the data.

Appendix B: **Force Measurement Systems**

The two balances used were the FF-11VT and the GA-10. These balances are the property of Virginia Polytechnic Institute and State University. A biaxial load cell, model 1216CEW-1K, was purchased for use in the hover rig. Use of load cells has been widely documented and known. For this reason, background on the mechanics and theory of this equipment will not be provided. Information about the individual parts is provided.

Vishay Measurements Group strain gauge conditioners (Model 2120A) were used to amplify the signals. These particular conditioners accept connections for quarter, half, or full Wheatstone bridges. Output gain is continuously adjustable between 1 and 2100. Up to eight channels were available with this conditioner and allowed all forces to be measurement simultaneously. Voltages were acquired with two NI-6009 USB data acquisition devices and programming was performed in LabView 8 environment.

B-1: FF-11VT Balance System

The FF-11VT balance was manufactured and calibrated by Modern Machine and Tool, Inc. It is a custom-made load cell, or balance, that will directly measure the three forces and three moments about a single reference point. Each load is measured by an independent channel comprised of a full bridge. The internal strain gages of this unit are arranged such that the interactional effects are less than 5% of the full load capacity (where <5% represents the worst-case scenario). Therefore the forces and moments can be directly recorded reducing the post-processing of the data.

An excitation of 5volts was applied. The calibration of this instrument was provided by the manufacture. Before performing an experiment, the calibration and settings were checked by applying known forces in specified directions through use of a pulley-weight system. In all cases, the FF-11VT was found to be a highly reliable instrument and yielded repeatable results.

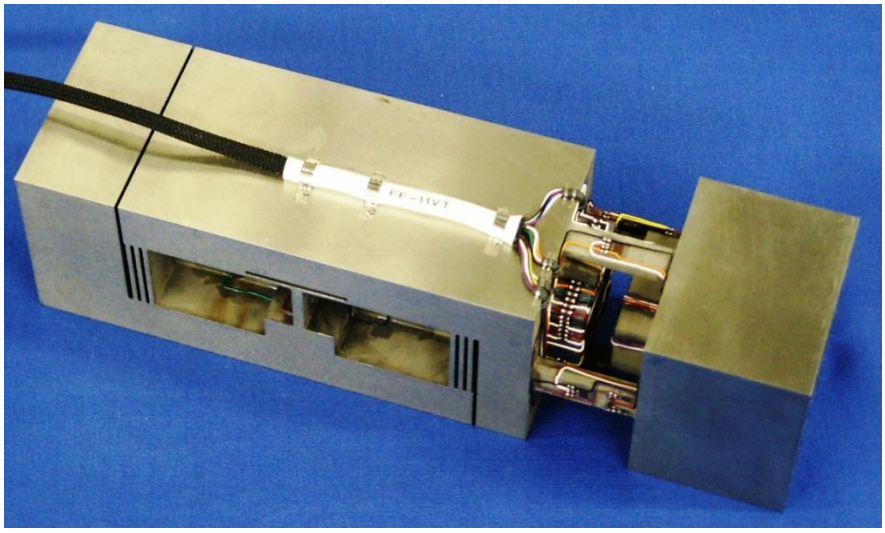

Appendix Figure B-1: Close-up of FF-11VT Balance

Appendix Table B-1: Full Scale Output and Sensitivity for FF-11VT Balance

COMPONENT	NF	AF	PM	RM	YM	SF
FS LOAD (lb or in-lb)	120	120	1,200	372.0	1,200	120
FS OUTPUT (μV/5V)	5,597	5,733	7,096	6,095	6,924	5,614
Sens (lb/μV/5V or in-lb/μV/5V)	2.14E-02	2.09E-02	1.69E-01	6.10E-02	1.73E-01	2.14E-02

Appendix Figure B-2: Detail drawing showing connections to FF-11VT.

B-2: GA-10 Balance

The NASA Langley GA10 is constructed in a similar manner the aforementioned FF-11VT Balance. The GA10 is considerably smaller in size and has a reduced load capacity on all channels. The balance and strain conditioning system was purchased from NASA and used in past experiments by Jason Gibbs.

During experiments, all six degrees of freedom were measured. Full calibrations were performed prior to utilizing this instrument. Some problems were encountered with the axial channel. This channel was able to be calibrated and yielded repeatable results, however, the axial direction was less sensitive to measurements. The axial channel is a possible source of error and should be considered for any later researchers. Aerodynamic loads were expected to be aligned with the normal axis. Therefore the reduced resolution on the axial channel was not a major cause of concern.

A rig was constructed to calibrate the GA10 balance. Different pulley and weight configurations were to apply known loads along all six degrees of freedom. All channels exhibit a strong linear trend as seen in Appendix Figure B-4, an excitation of 10 volts was applied.

Appendix Figure B-3: Close-up of the GA-11 balance.

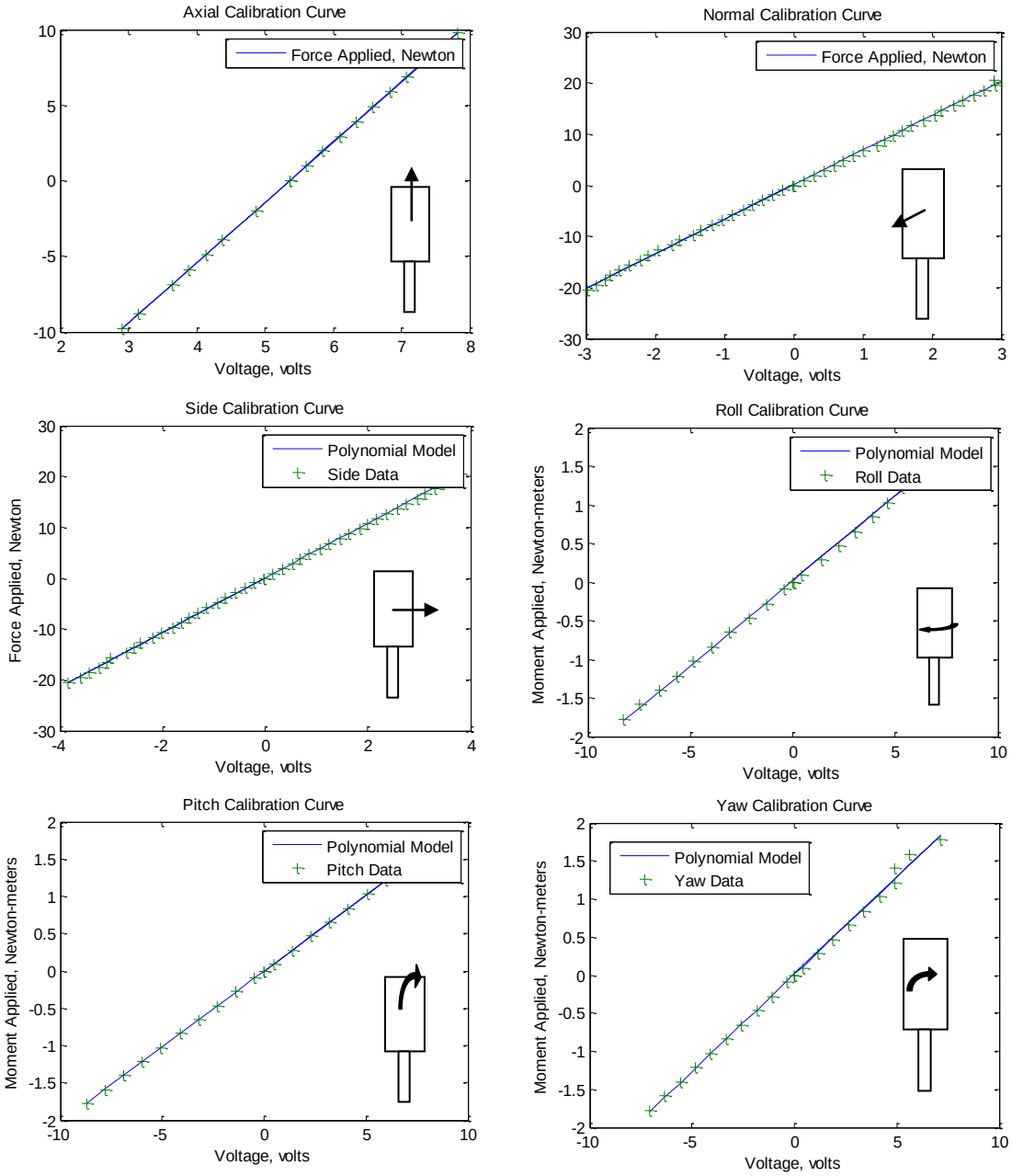

Appendix Figure B-4: Calibration curves for GA-10 Balance.

Appendix Table B-2: Calibration results for GA-11 balance.

COMPONENT	NF	AF	PM	RM	YM	SF
FS LOAD (lb or in-lb)	9	3	27	7.5	27	6
Final Slope	6.7644	3.9924	0.0203	0.0220	0.0255	5.3711

B-3: Biaxial Load Cell

The biaxial load cell was required for the hover rig because the thrust and torque existed at the same moment. Individual load cells for each force would not have been appropriate due to the possible interaction effects. An Interface load cell, model 1216CEW-1K, was chosen. It has a capacity of 1000lbf axial load and 500in-lb torsional load. Detailed information about the load cell is included in the calibration certifications. An excitation of 10 volts was applied.

Calibrations of the hover rig are explained in Chapter 4 of this document.

interface
ADVANCED FORCE MEASUREMENT

LOAD CELL CALIBRATION CERTIFICATION

CONDITION: FINAL
MODEL: 1216CEW-1K SERIAL: 263592 BRIDGE: A CAPACITY: 1000 lbf
PROCEDURE: C-1257 Mounting Per Interface Installation Instruction 15-5

INPUT RESISTANCE: 699.1 OHM OUTPUT RESISTANCE: 699.0 OHM
ZERO BALANCE : -0.638 %RO

TEST CONDITIONS

TEMPERATURE: 74 °F HUMIDITY: 37 % EXCITATION: 10 VDC

TRACEABILITY

FORCE STANDARD : STD-28 NIST #: 822/258487-97 DUE: 15-JAN-09
STANDARD INDICATOR: BRD250 NIST #: 512727
TEST INDICATOR : BRD308 NIST #: 512727

SHUNT CALIBRATION

	Shunt (± 0.01%)	Output	Straight Line Conversion		Connections*
Tension	120 Kohm	1.45223 mV/V	964.53	lbf	-Out to -Exc
Compression	120 Kohm	-1.45228 mV/V	962.66	lbf	-Out to +Exc

*For models wired with +Sense, -Sense, or -SCal leads, resistor connections are actually to these leads in place of +Exc, -Exc, or -Out respectively.

PERFORMANCE

	RATED OUTPUT	SEB OUTPUT	NONLINEARITY	HYSTERESIS		SEB
TENSION	1.50535 mV/V	1.50561 mV/V	.007 %FS	.018 %FS	±	.018 %FS
COMPRESSION	-1.50819 mV/V	-1.50860 mV/V	.043 %FS	-.008 %FS	±	.027 %FS

STATIC ERROR BAND (SEB) - The band of maximum deviations of the ascending and descending calibration points from a best fit straight line through zero OUTPUT. It includes the effects of NONLINEARITY, HYSTERESIS, and nonrecurro to MINIMUM LOAD.

TEST LOAD APPLIED (lbf)	RECORDED READINGS (mV/V) Tension	Compression
0	.00000	.00000
200	.30115	-.30194
400	.60224	-.60385
600	.90330	-.90556
800	1.20430	-1.20693
1000	1.50535	-1.50819
400	.60251	-.60373
0	.00003	-.00002

Interface, Inc. certifies that all calibration measurements are traceable to NIST. Estimated uncertainty of measurements is 0.05%. Results relate to 263592 only. Do not reproduce this report except in full or with Interface written approval.

TECHNICIAN : Karsten Mueller DATE :18-OCT-07

INTERFACE INC.
7401 EAST BUTHERUS DRIVE · SCOTTSDALE, ARIZONA 85260, U.S.A.
TELEPHONE (480)948-5555 · FAX (480)948-1924

F16-30-1104

PAGE 1 OF 1

Appendix Figure B-5: Axial calibration for the Biaxial Load cell.

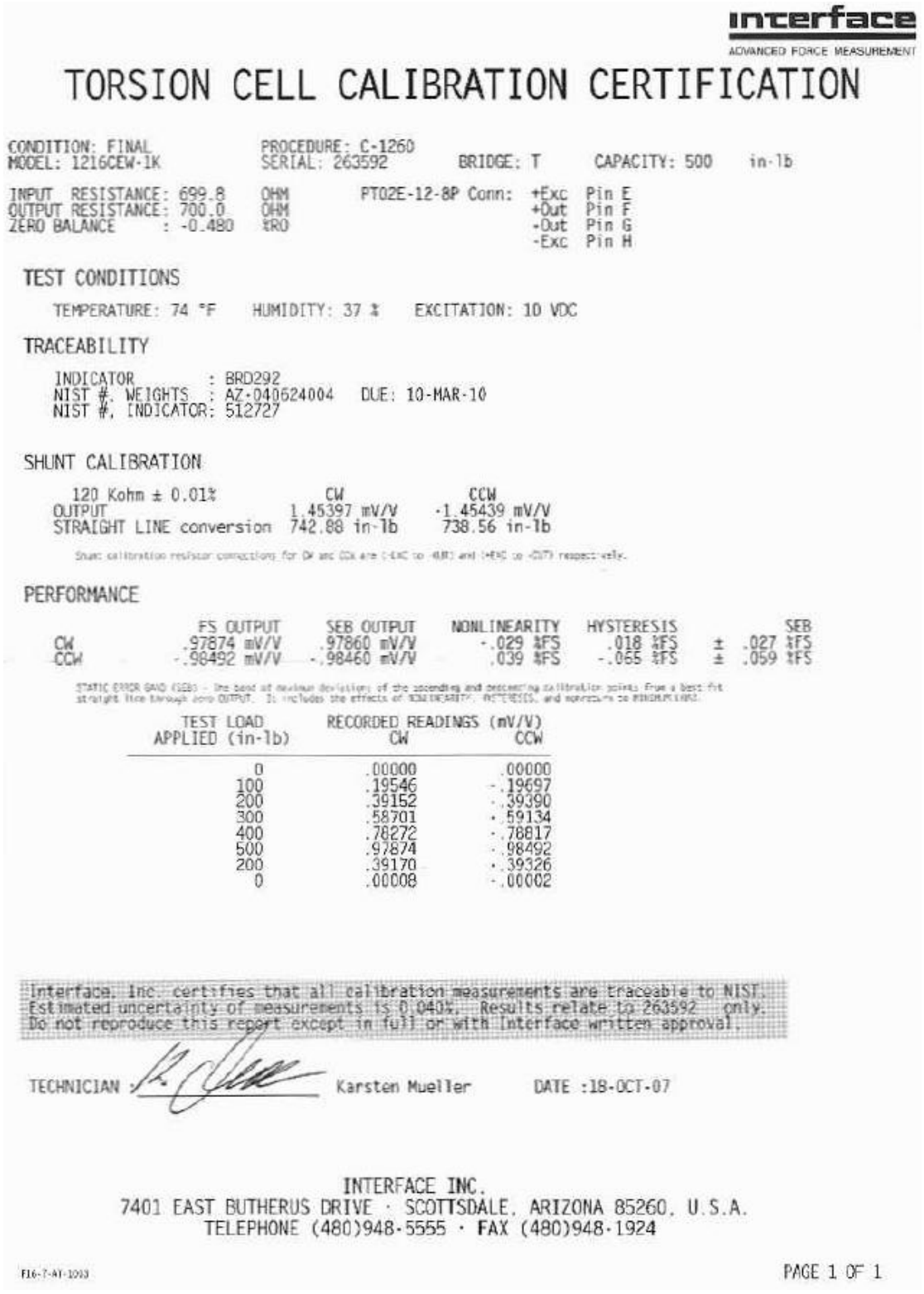

interface
ADVANCED FORCE MEASUREMENT

TORSION CELL CALIBRATION CERTIFICATION

CONDITION: FINAL — PROCEDURE: C-1260
MODEL: 1216CEW-1K — SERIAL: 263592 — BRIDGE: T — CAPACITY: 500 in-lb

INPUT RESISTANCE:	699.8	OHM	PT02E-12-8P Conn:	+Exc	Pin E
OUTPUT RESISTANCE:	700.0	OHM		+Out	Pin F
ZERO BALANCE :	-0.480	%RO		-Out	Pin G
				-Exc	Pin H

TEST CONDITIONS

TEMPERATURE: 74 °F HUMIDITY: 37 % EXCITATION: 10 VDC

TRACEABILITY

INDICATOR : BRD292
NIST #, WEIGHTS : AZ-040624004 DUE: 10-MAR-10
NIST #, INDICATOR: 512727

SHUNT CALIBRATION

120 Kohm ± 0.01%	CW	CCW
OUTPUT	1.45397 mV/V	-1.45439 mV/V
STRAIGHT LINE conversion	742.88 in-lb	738.56 in-lb

Shunt calibration resistor connections for CW and CCW are (-EXC to -OUT) and (+EXC to +OUT) respectively.

PERFORMANCE

	FS OUTPUT	SEB OUTPUT	NONLINEARITY	HYSTERESIS		SEB
CW	.97874 mV/V	.97860 mV/V	-.029 %FS	.018 %FS	±	.027 %FS
CCW	-.98492 mV/V	-.98460 mV/V	.039 %FS	-.065 %FS	±	.059 %FS

STATIC ERROR BAND (SEB) - The band of maximum deviation of the ascending and descending calibration points from a best fit straight line through zero OUTPUT. It includes the effects of NONLINEARITY, HYSTERESIS, and repeatability as applicable.

TEST LOAD APPLIED (in-lb)	RECORDED READINGS (mV/V) CW	CCW
0	.00000	.00000
100	.19546	-.19697
200	.39152	-.39390
300	.58701	-.59134
400	.78272	-.78817
500	.97874	-.98492
200	.39170	-.39326
0	.00008	-.00002

Interface, Inc. certifies that all calibration measurements are traceable to NIST. Estimated uncertainty of measurements is 0.040%. Results relate to 263592 only. Do not reproduce this report except in full or with Interface written approval.

TECHNICIAN Karsten Mueller DATE :18-OCT-07

INTERFACE INC.
7401 EAST BUTHERUS DRIVE · SCOTTSDALE, ARIZONA 85260, U.S.A.
TELEPHONE (480)948-5555 · FAX (480)948-1924

F16-7-AT-1003

PAGE 1 OF 1

Appendix Figure B-6: Torsional calibration for the Biaxial Load cell.

Appendix C: **Hover Rig**

Before beginning this work, there was no available experimental equipment or facilities which could rotate the model at our desired speeds. The "hover rig" was designed and constructed in the Fluids Lab located in Norris Hall at Virginia Tech. The goal was to achieve tip speeds up to 500fps (340mph) with the rotor shown in Figure 4-1. The main purpose of the rig was to measure the thrust and torque generated by the model during hover in conditions both near and far from the ground. The forces were measured via a two component load cell while the ground conditions were simulated by a movable wall described below.

The following sections provide component-specific details on the hover rig. For additional discussion, see Chapter 4.

C-1: Stand

A metal structure was required to support the experimental system during testing. To aviod effects from the floor of the room, the stand needed to be nearly 6ft tall. A large iron structure was built to hold the testing apparatus horizontally in the room. The structure was made from welding a series of "L" and square beams together. The ceiling of the room is nearly 12ft and the model was held in the middle. To reduce raw material cost, an existing iron table was used as a base to reach the required 6ft height. All parts were welded together with the exception of the table (which was bolted). Will all parts together, the structure was bolted to the concrete floor of the lab. Selected detail drawings are included.

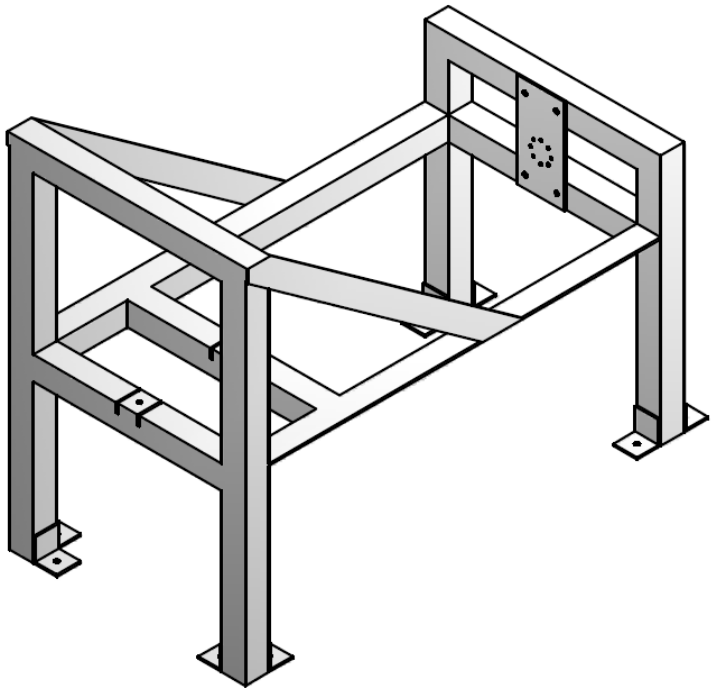

Appendix Figure C-1: Top of hover stand, constructed in ESM machine shop.

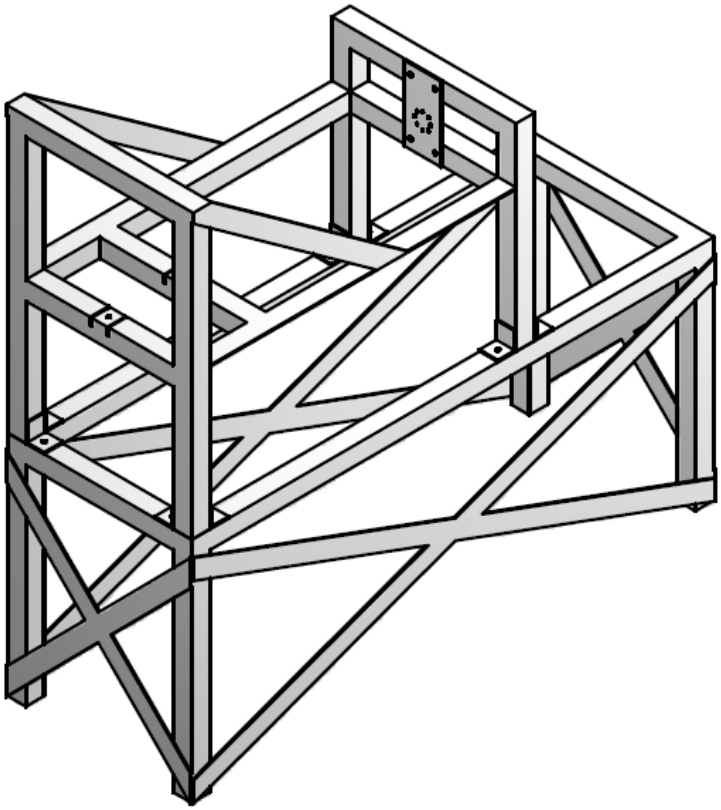

Appendix Figure C-2: Entire assembly of stand

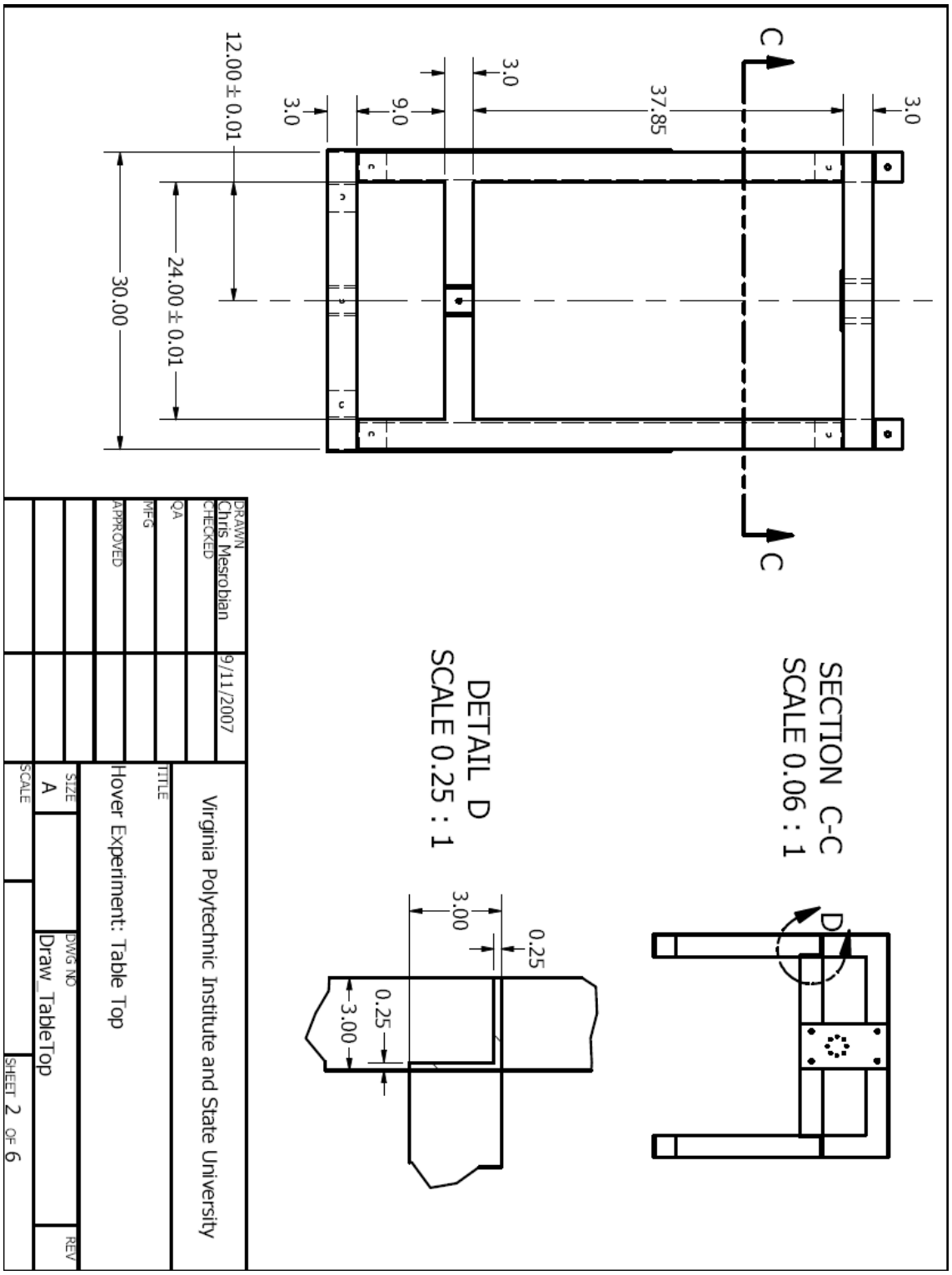

Appendix Figure C-3: Drawing with top view of stand.

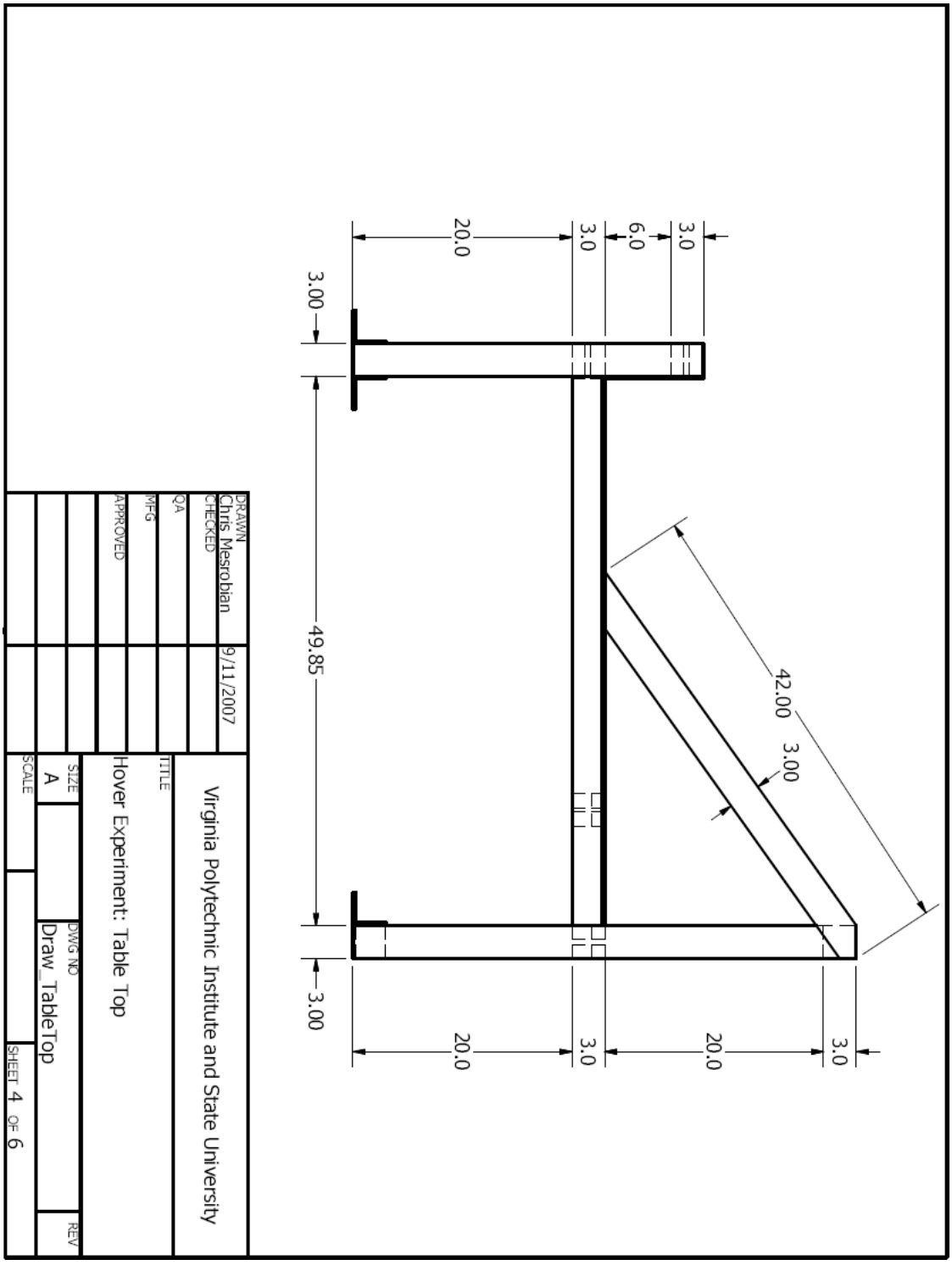

Appendix Figure C-4: Drawing with side view of stand.

C-2: Biaxial Load Cell

The biaxial load cell was required for the hover rig because the thrust and torque existed at the same moment. Individual load cells for each force would not have been appropriate due to the possible interaction effects. An Interface load cell, model 1216CEW-1K, was chosen. It has a capacity of 1000lbf axial load and 500in-lb torsional load. Detailed information about the load cell is included in the calibration certifications. To get a signal with the load cell, a 2100 strain gage conditioner and amplifier system manufactured by Vishay Measurements was used with an excitation of 10volts. A NI USB-6009 data acquisition system was then connected to sample the signal.

C-3: Motor

A 15hp Leeson AC motor (model #C215T34FB51C) was selected to power the model during experimentation. To control the speed of the motor, the G53-2015 Dura Pulse motor drive was selected for the motor. This system allowed for rotational speeds between 1100 and 3750 RPM. An Ethernet adapter was purchased for the motor drive and allowed remote control of the drive via a computer running LabView. Output of the motor's speed and performance was recorded by the computer during tests. This allowed the users to be a safe distance from the model. To offset the weight of the motor on the load cell and shaft, a support cable was connected to the motor. The cable was about 5ft in length and directly above the motor so that any axial force from the cable was negligible.

A 1538-A Electronic Stroboscope was used to check the accuracy of the motor's rotational speeds. Once at a constant RPM value, the speed was determined by visually matching the correct frequency with the stroboscope. At the correct frequency, the model will appear stationary. The motor drive was found to be within manufacturer limits of less than 5% at all RPM values. In most cases, the RPM values matched exactly where errors were mainly caused by the user.

C-4: Bearings and Shaft

To allow the transmission of the torque and thrust but still provide the needed support, two linear ball bearings were placed along the shaft. These were LR-24 bearings produced by Linear Rotary Bearings, Inc. and fit a nominal shaft diameter of 1.5". Specific tolerances on the shaft radius and hardness recommended by manufacturers were taken into consideration to ensure the most efficient bearing performance.

During experimentation, it was noticed that the bearings will create a relatively small axial force, or thrust, when compared to measured quantities. This was measured during the "tare" when no model was present. A small thrust is generated when rotating at these high speeds due to the design of the bearings. This effect was measured and removed from all results. These bearings showed to be an appropriate choice for their cost and availability.

Appendix Figure C-5: Image of LRB ball bearing, similar to model in hover rig.

C-5: Wall (Simulated Ground)

An 8ft by 8ft wall was built and placed downstream of the rotor which was to simulate the ground during experimentation. This wall was made from plywood and 2"x4" wood supports. The flat 8ft by 8ft wall was finished and painted to be a smooth surface and care was taken to ensure the wall was perpendicular to the model. This wall was not fixed in

place, and could be moved to examine the effects of ground distance. During testing, weights were placed on the base behind the wall to prevent movement.

In later tests, a section of the wall's surface was replaced with an aluminum plate instrumented with 1/16" pressure taps. Any gaps were filled with an epoxy to maintain a smooth surface. The pressures were measured by the ESP scanner system purchased from Aeroprobe.

C-6: Model

The rotor model was manufactured in the Virginia Tech Mechanical Engineering machine shop. Blades on the rotor are 2.7" chord and 8" in length and are connected to steel "pitching rods" which control the collective pitch angle. For each pitch angle, these rods are replaced. Each rod passes through the outer ring and is fixed in the inner hub. With exception of the outer ring, all parts of the model are fixed to the inner hub for that is the part secured to the shaft. The outer ring creates the outer edge of the disc where the radius of curvature is ¾" (total thickness of model is 1.5"). Two flat plates are attached to the top and bottom of the ring and secured to the hub.

Accurate balancing of the model is required for the desired rotational speeds. Only two dimensional (static balancing) is required because of the relatively thin rotor model. Balancing was achieved by a static balancer where the center of mass is determined by gravity. A lead mass was added inside the model and the process was repeated until the model was sufficiently balanced.

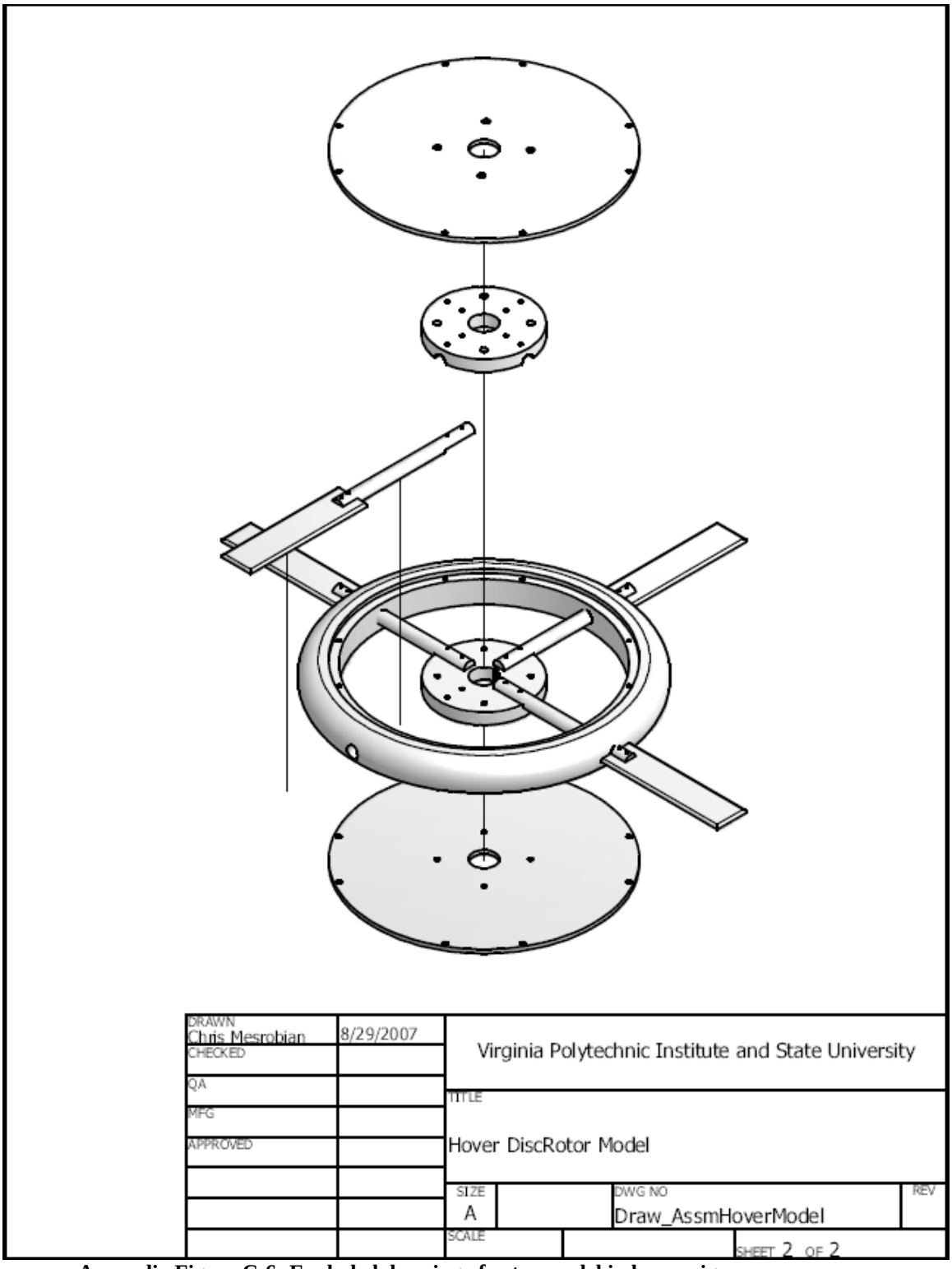

Appendix Figure C-6: Exploded drawing of rotor model in hover rig.

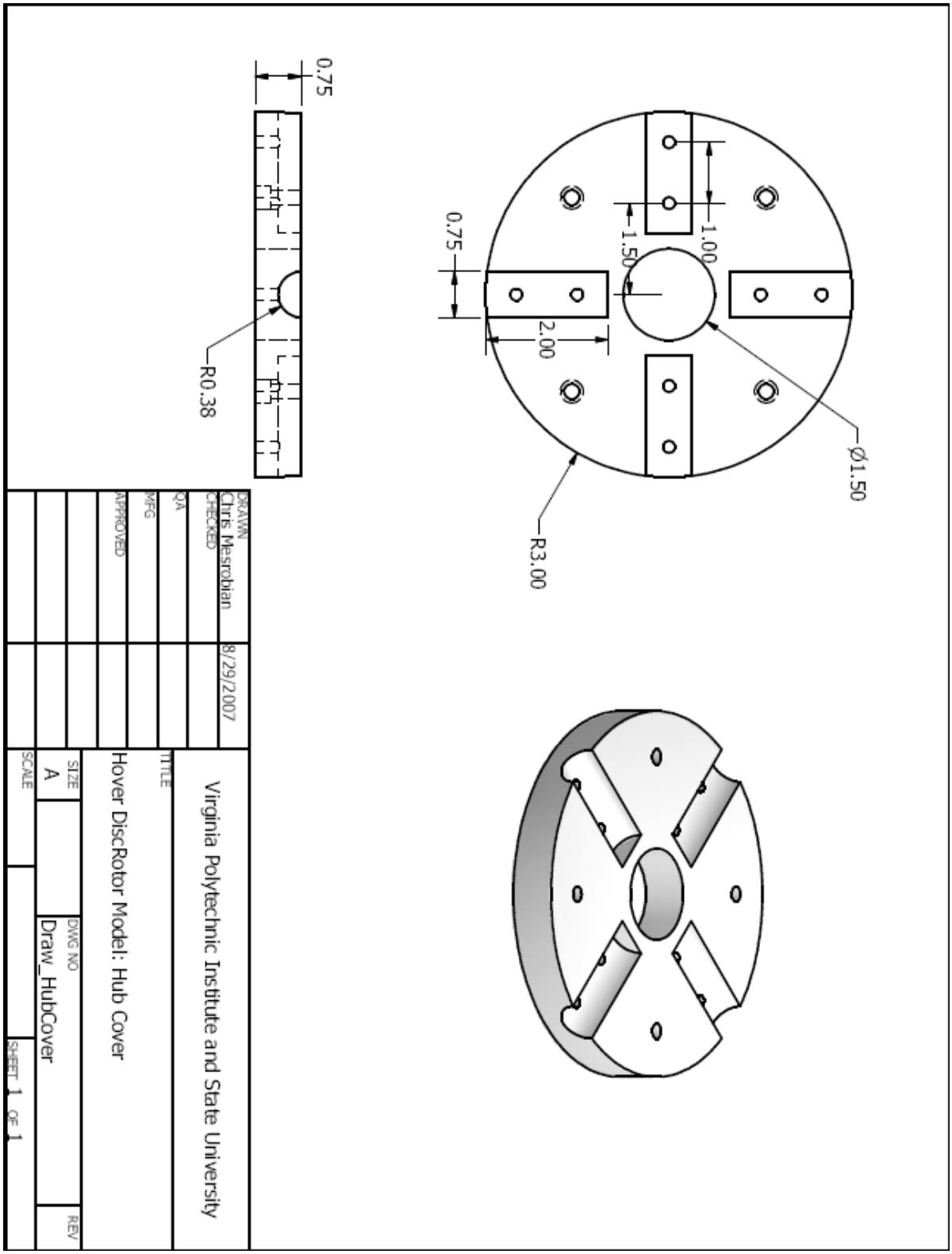

Appendix Figure C-7: Top half of inner hub, round portions are to receive the pitch rods.

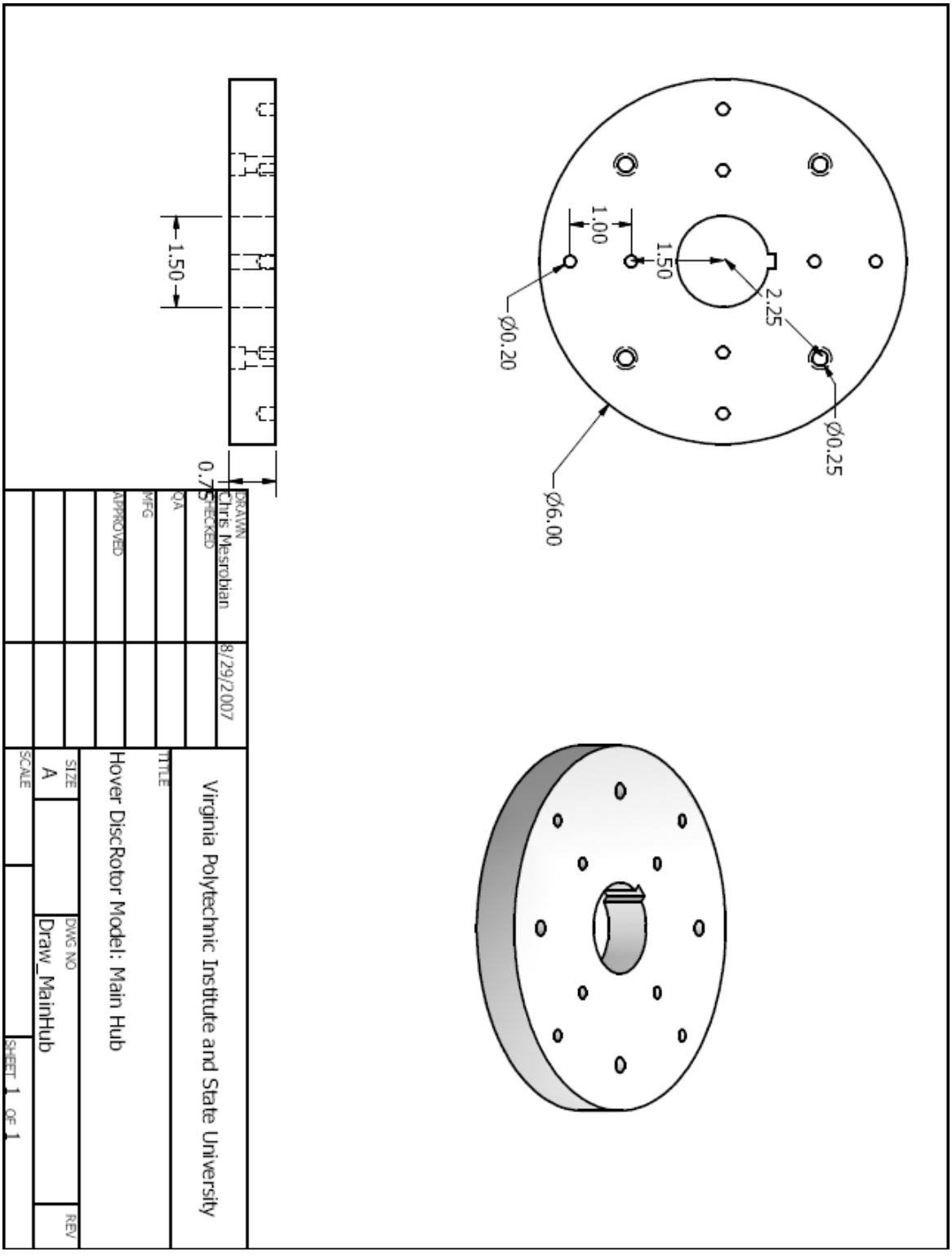

Appendix Figure C-8: Bottom half of inner hub.

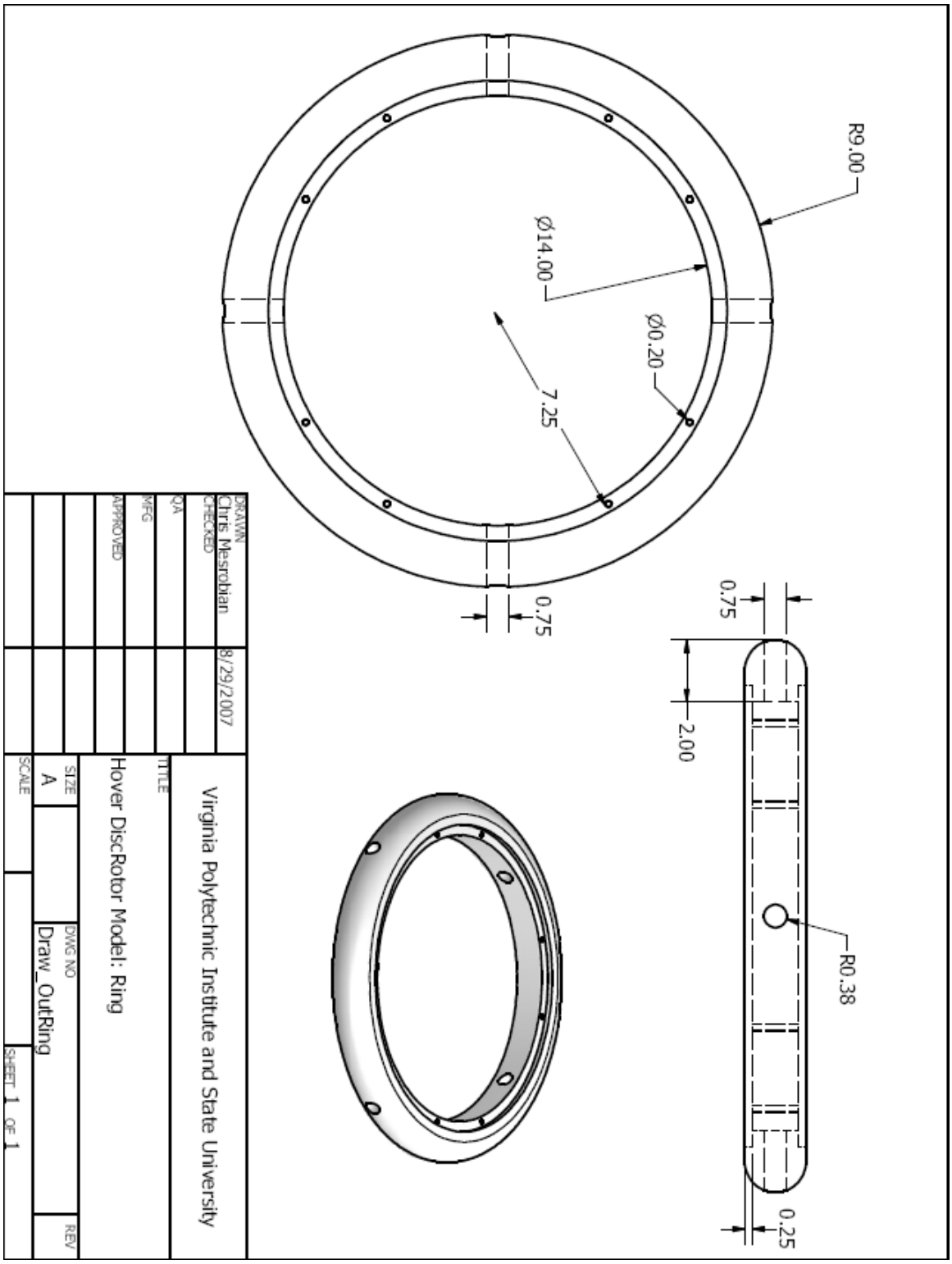

Appendix Figure C-9: Outer ring of hover model.

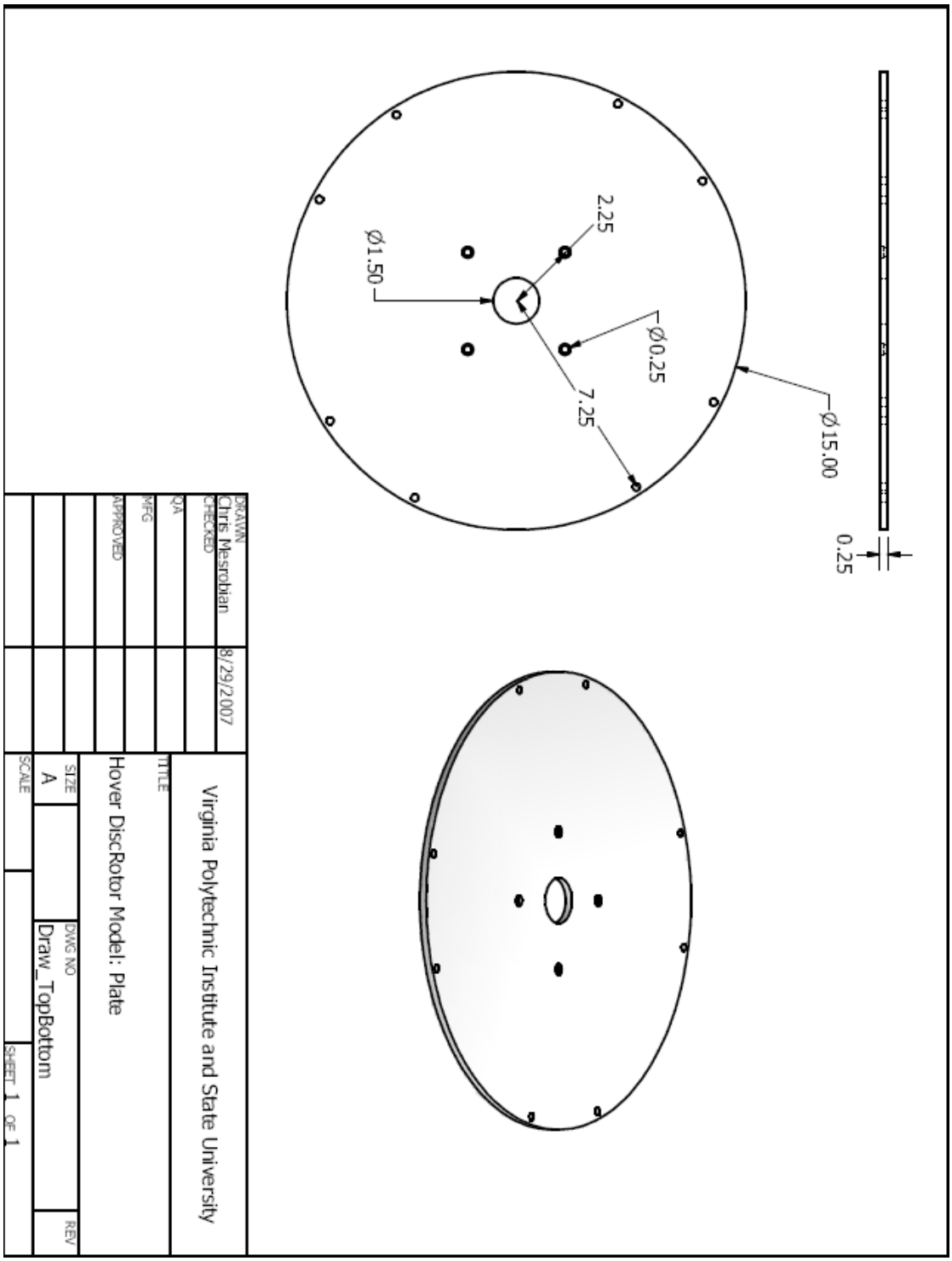

Appendix Figure C-10: Top and bottom plates of hover model.

Appendix D: **Wind Tunnel Model - Fuselage**

The fuselage body has a 3.6 in by 3.6 in cross section and a total length of nearly three feet. The fuselage was built around the FF-11VT balance, which is an internal balance, and the aerodynamic forces could be directly measured. With this instrument, interaction and nonlinearities effects have been shown to be negligible. See Chapter 2 for additional information on the FF-11VT balance. The balance was rigidly connected to the sting and the fuselage was connected to the opposite end. The fuselage only made contact with a single surface of the balance.

Details of the fuselage are shown in the following figures. Some drawings depict a tail at the end of the fuselage (attached to the top plate). This tail was not machined and was never present during testing.

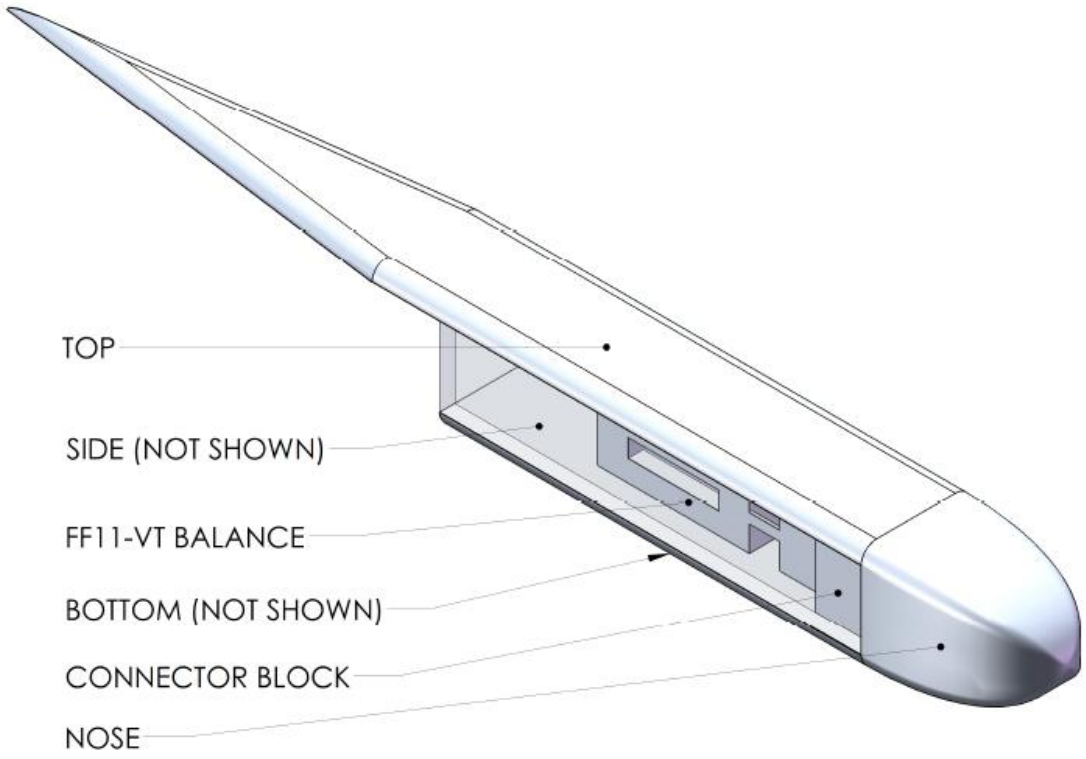

Appendix Figure D-1: Assembly sketch of fuselage model.

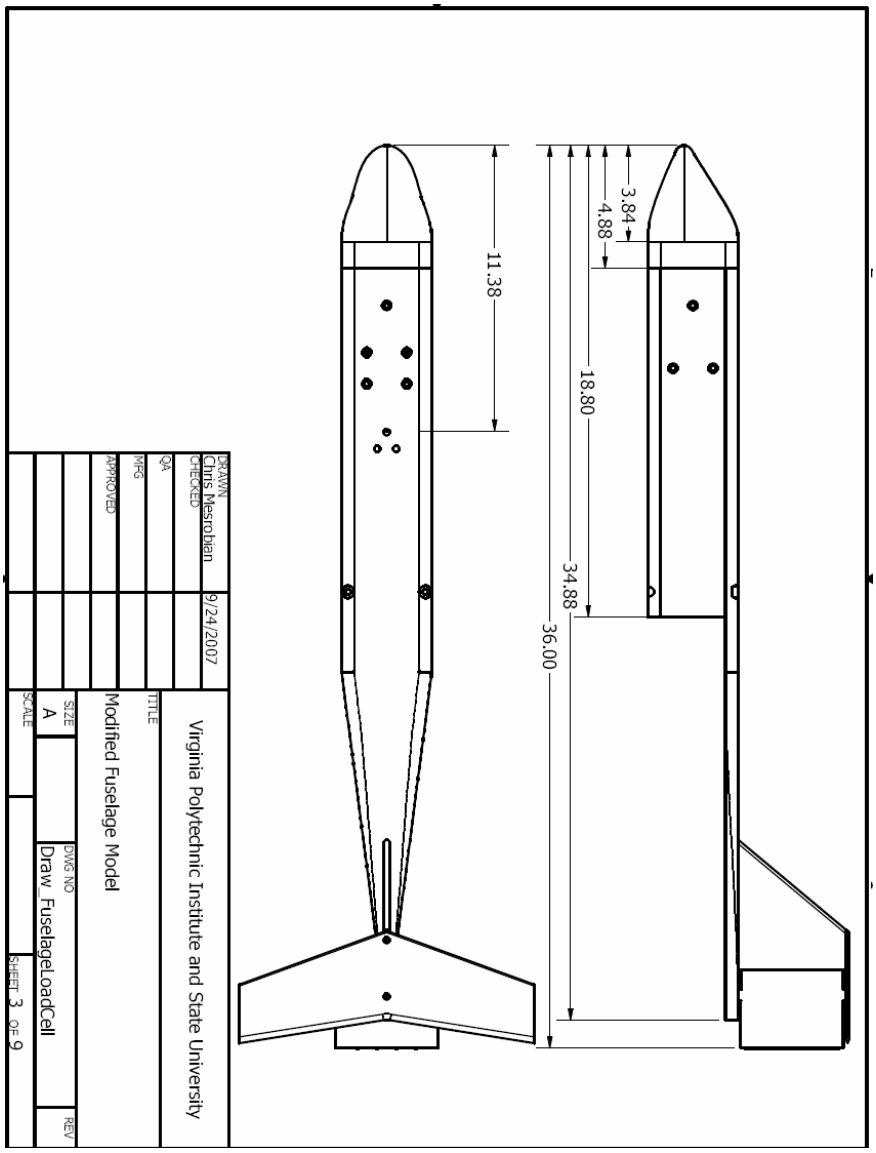

Appendix Figure D-2: Detailed drawing of fuselage.
Note: Tail shown in this drawing was not considered under the scope of this work.

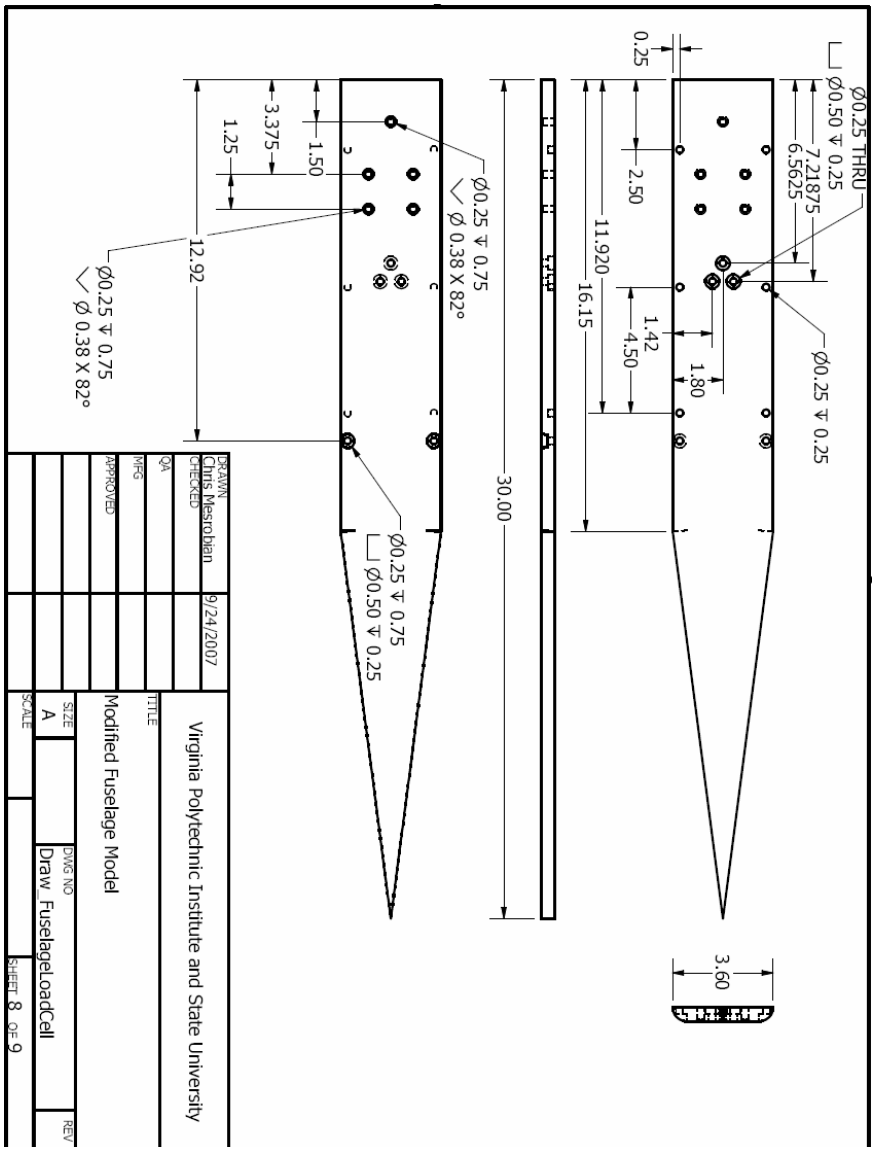

Appendix Figure D-3: Detailed drawing of fuselage top plate.

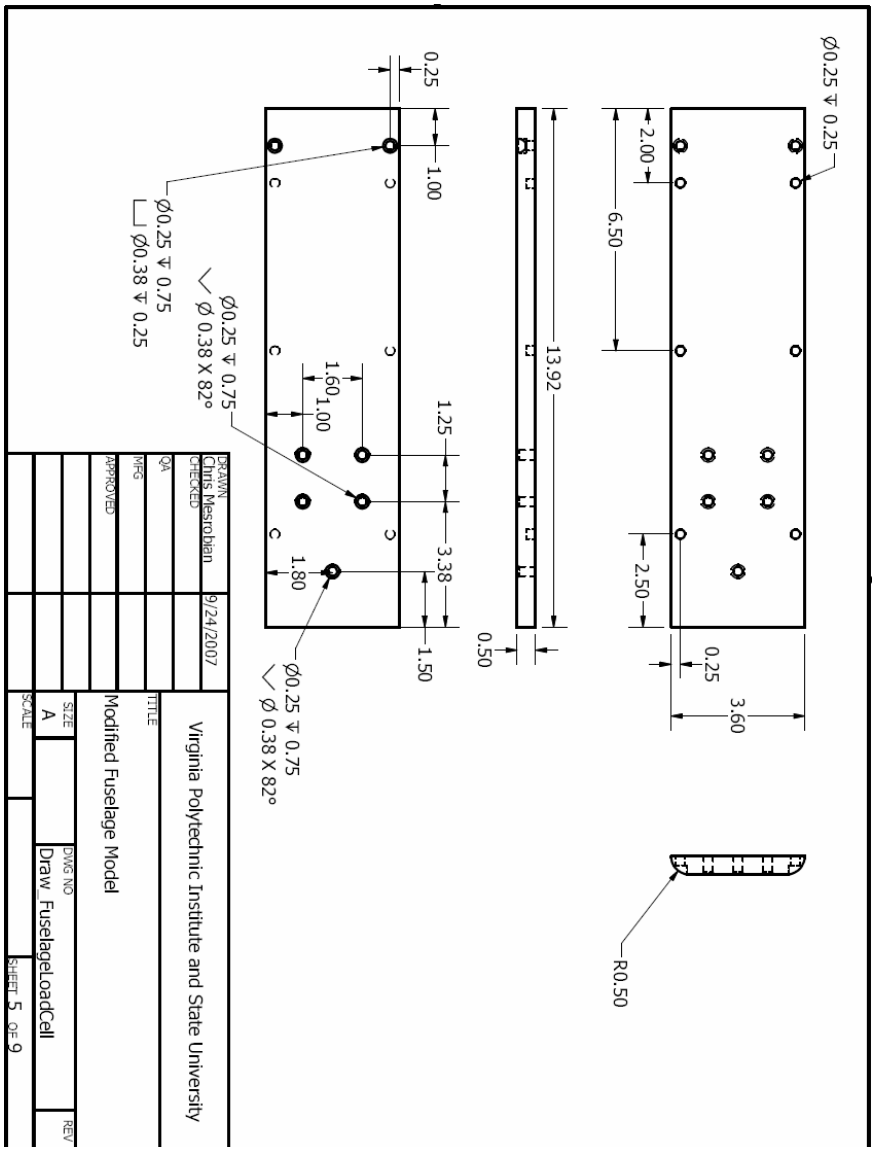

Appendix Figure D-4: Detailed drawing of fuselage bottom plate.

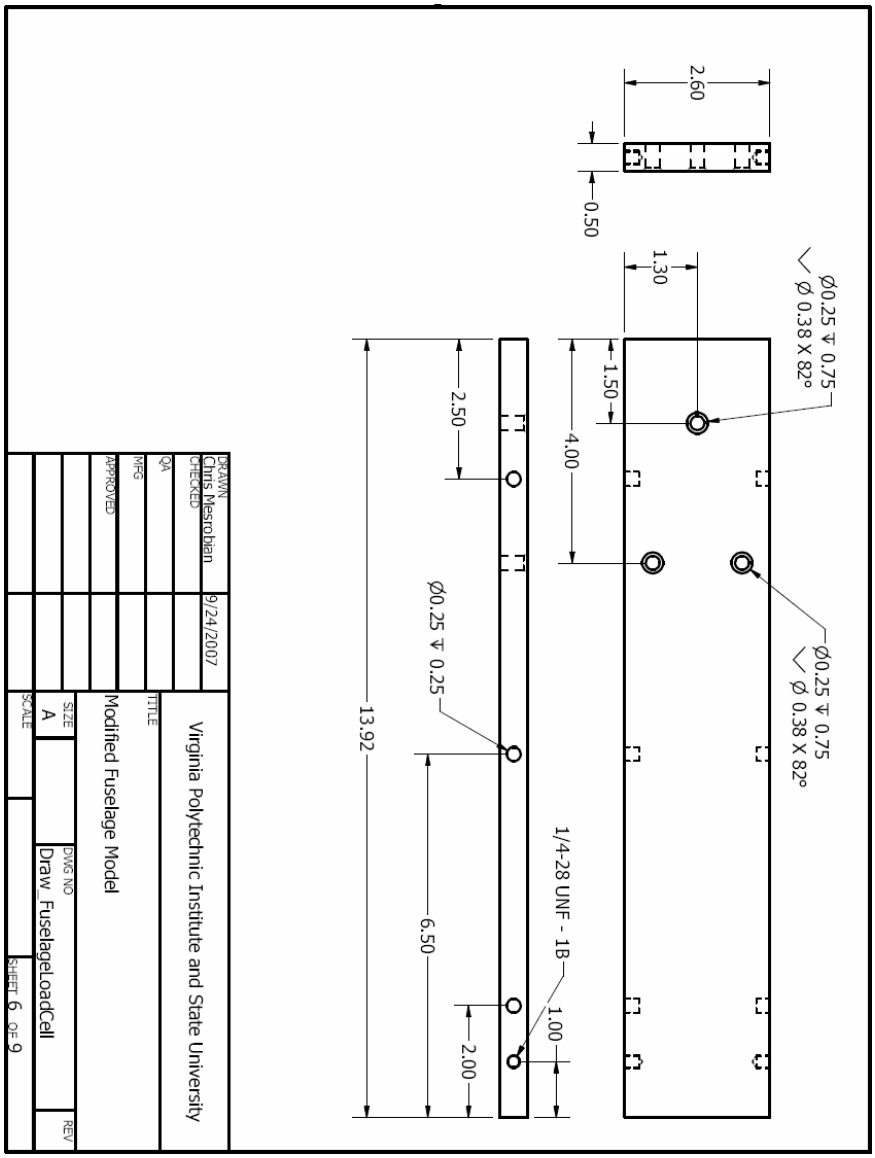

Appendix Figure D-5: Detailed drawing of Fuselage side plate. Two total in assembly.

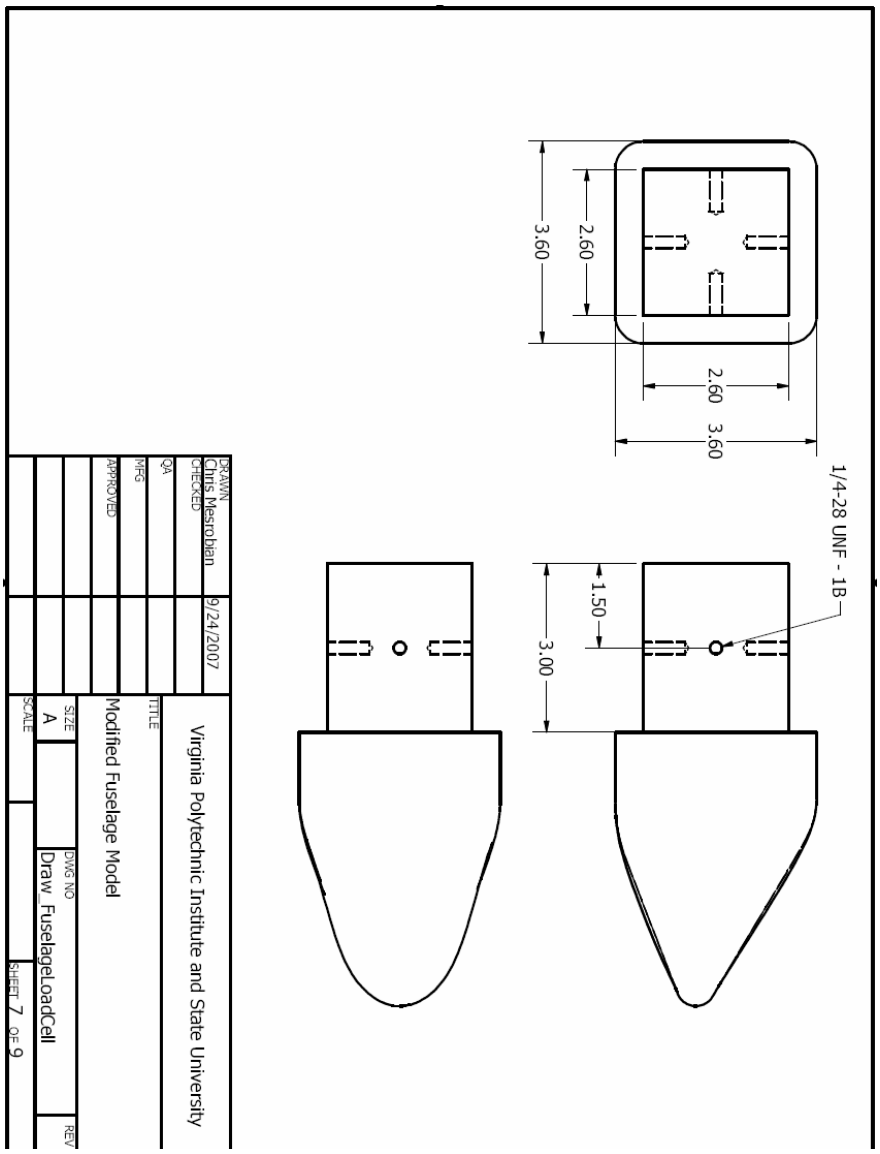

Appendix Figure D-6: Detailed drawing of Fuselage nose (1 of 2)

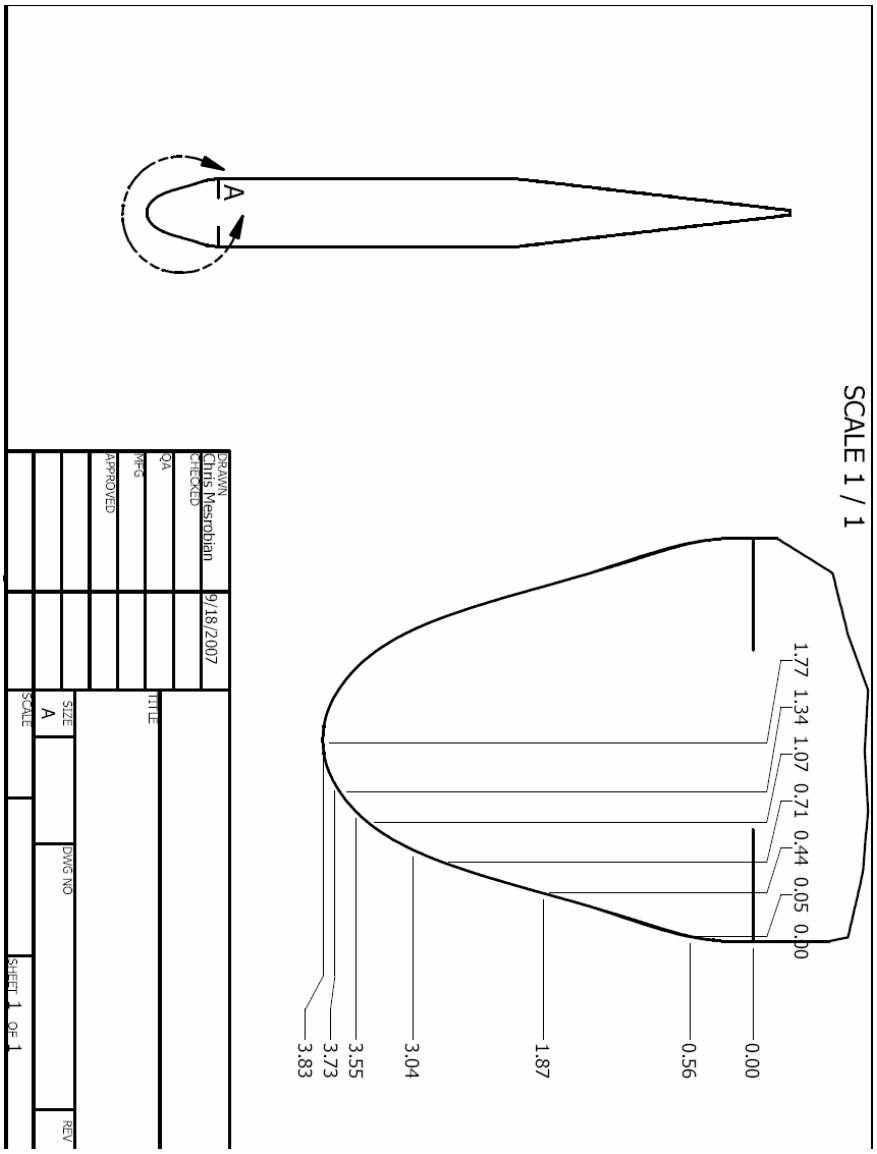

Appendix Figure D-7: Detailed drawing of Fuselage nose (2 of 2). Actual machined dimensions may differ slightly.

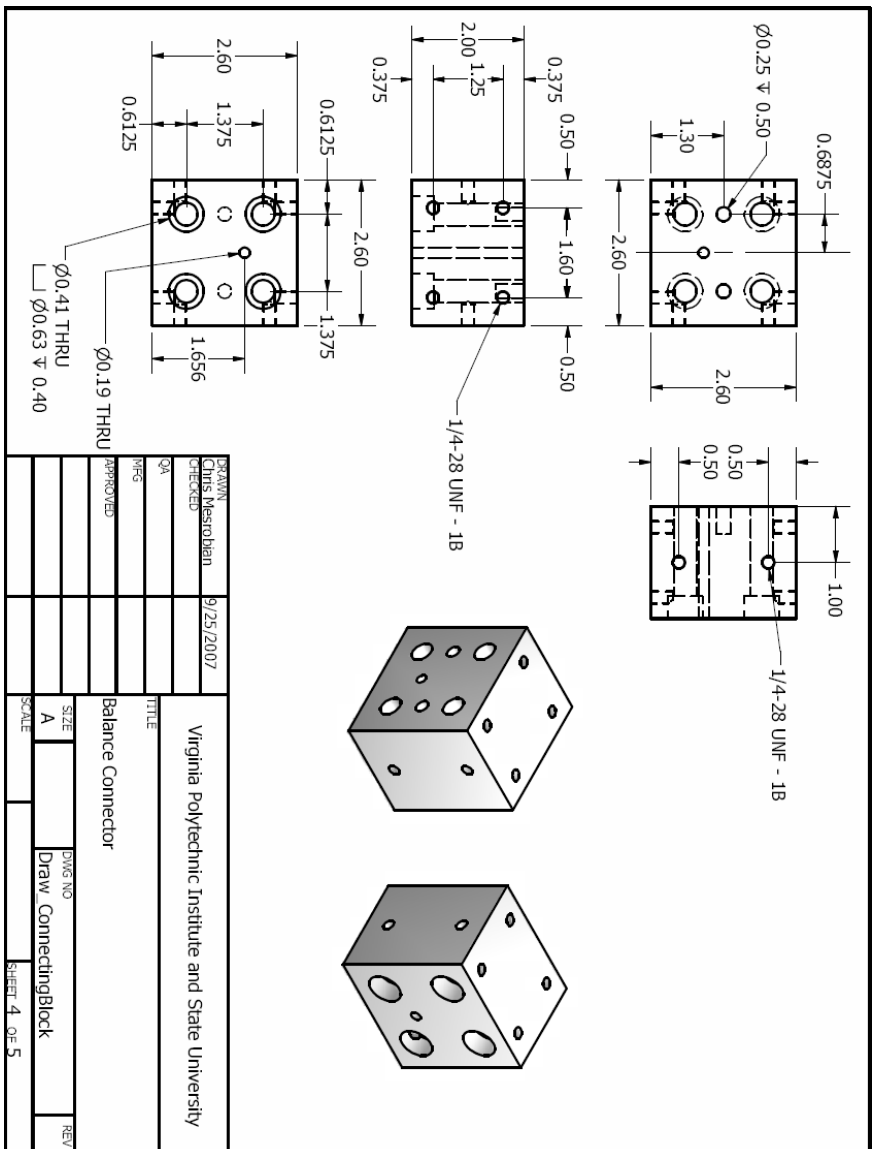

Appendix Figure D-8: Detailed drawing of Connector Block. All parts were fixed to this block for connection to balance.

Appendix E: **Tabulated Data - Wind Tunnel Forces**

Figures shown in Chapter 3 present curves based upon experimental data of measured forces during experiments. The data points are summarized in the following tables for following research and design efforts.

E-1: Stability Tunnel Results

The following tables summarize the data recorded on the wind tunnel model during experiments performed in the VA Tech Stability Tunnel.

Appendix Table E-1: Stability Tunnel Results, Re= 2x106

AOA (º)	Fuselage and Disc			
	U_∞ (m/s)	CL	CD	L/D
-4	67.16932	-0.18454	0.050361	-3.66437
-2	67.1525	-0.1235	0.044292	-2.78827
0	67.24538	-0.06141	0.040401	-1.51995
2	67.06788	0.000362	0.04266	0.008497
4	67.07181	0.064781	0.045436	1.425773
6	66.96875	0.128758	0.051702	2.490406
8	66.81668	0.194487	0.060586	3.210094
9	66.91685	0.22682	0.066163	3.428197
10	66.88203	0.261481	0.072695	3.596973
11	66.81424	0.296096	0.080186	3.692623
12	66.80267	0.333672	0.088862	3.754935
13	66.67204	0.37345	0.104799	3.563497
14	66.55473	0.416848	0.114308	3.646702
15	66.51301	0.455162	0.126943	3.58555
16	67.24915	0.496385	0.142063	3.494113
17	67.07645	0.533288	0.171708	3.105781
18	66.88127	0.575091	0.194487	2.956971
19	66.86518	0.618322	0.200184	3.088768
20	66.67335	0.657446	0.220297	2.984364
21	66.23067	0.69733	0.275158	2.534287
22	65.99679	0.734972	0.299402	2.454801

Appendix Table E-2: Stability Tunnel Results, Re= 2x106

	Fuselage and Disc			
AOA (º)	U_∞ (m/s)	CL	CD	L/D
-4	47.37067	-0.1097	0.062667	-1.75049
-2	47.22448	-0.05173	0.058701	-0.88121
0	47.23177	0.014582	0.056298	0.259025
2	47.21282	0.077706	0.061038	1.273074
4	47.10699	0.140303	0.066995	2.094235
6	47.1591	0.203116	0.074739	2.717657
8	47.0717	0.265284	0.08564	3.097657
9	47.14793	0.304833	0.095753	3.183521
10	47.13447	0.329539	0.09977	3.302988
11	47.04009	0.362712	0.107823	3.363954
12	47.107	0.39808	0.117184	3.397057
13	47.13653	0.442772	0.13067	3.388484
14	47.01219	0.476184	0.141202	3.37235
15	47.13664	0.511189	0.154971	3.298615
16	46.91638	0.546823	0.179579	3.045029
17	46.83339	0.595891	0.203371	2.930068
18	46.59047	0.640452	0.232429	2.755469
19	46.64606	0.676532	0.257751	2.624755
20	46.43959	0.71469	0.286872	2.491321
21	46.17669	0.74899	0.311628	2.403476
22	46.04194	0.798065	0.331276	2.409066

Appendix Table E-3: Stability Tunnel Results, Re= 2x106

	FDB with 2.4C, 8L blades			
AOA (º)	U_∞ (m/s)	CL	CD	L/D
-4	66.82067	-0.19265	0.049535	-3.8892
-2	66.828	-0.08052	0.040995	-1.96413
0	66.90037	0.019026	0.040957	0.464523
2	66.80496	0.122296	0.04475	2.732871
4	66.94213	0.237956	0.055654	4.275633
6	66.91228	0.313642	0.070941	4.421196
8	66.74523	0.376414	0.087572	4.298317
9	67.0894	0.415409	0.097874	4.244331
10	67.02035	0.450074	0.108963	4.130522
11	67.0142	0.488363	0.120887	4.039846
12	66.99178	0.525039	0.134725	3.897126
13	66.90064	0.560215	0.148584	3.770351
14	66.86819	0.599128	0.164956	3.632051
15	67.00865	0.632902	0.181831	3.48071
16	66.83176	0.66656	0.199299	3.344518
17	67.3181	0.70147	0.220004	3.188446
18	67.19826	0.728618	0.241842	3.012786
19	67.00589	0.755696	0.262862	2.874879
20	66.83278	0.780629	0.292921	2.664979
21	66.33924	0.779247	0.334853	2.32713
22	66.01692	0.793914	0.358972	2.211633

Appendix Table E-4: Stability Tunnel Results, Re= 2x106

	FBD with 2.4C, 6.75L			
AOA (º)	U_∞ (m/s)	CL	CD	L/D
-4	67.51623	-0.17501	0.044707	-3.91459
-2	67.62064	-0.06974	0.041017	-1.70036
0	67.65436	0.02319	0.040994	0.56569
2	67.55243	0.124248	0.045505	2.730438
4	67.45347	0.229018	0.056484	4.054593
6	67.40636	0.305303	0.071525	4.268508
8	67.21189	0.37058	0.087801	4.220659
9	67.66113	0.406873	0.097546	4.171107
10	67.59938	0.442749	0.108478	4.081484
11	67.59429	0.48151	0.120512	3.995519
12	67.60626	0.518635	0.134304	3.861657
13	67.62318	0.556743	0.148213	3.756377
14	67.53327	0.594688	0.164055	3.624932
15	67.62268	0.628002	0.179431	3.499969
16	67.55391	0.66131	0.19755	3.347552
17	67.59408	0.696839	0.218862	3.183922
18	67.76531	0.725358	0.241008	3.009684
19	67.55955	0.753694	0.262803	2.867904
20	67.72518	0.773752	0.293847	2.633176
21	67.45348	0.778963	0.335525	2.321622
22	67.77228	0.794411	0.358938	2.213226

Appendix Table E-5: Stability Tunnel Results, Re= 2x106

	FBD with 2.4C, 6.75L			
AOA (º)	U_∞ (m/s)	CL	CD	L/D
-4	67.83213	-0.17421	0.038417	-4.53486
-2	67.864	-0.07308	0.033817	-2.161
0	67.88093	0.023744	0.033622	0.706219
2	67.73996	0.127723	0.039959	3.196325
4	67.85035	0.219983	0.051427	4.27759
6	67.94752	0.288403	0.065254	4.419689
8	67.92329	0.358002	0.085357	4.194192
9	67.82115	0.392533	0.094894	4.136526
10	67.96007	0.42777	0.105016	4.073393
11	67.92942	0.46576	0.11685	3.985979
12	67.90956	0.504258	0.129823	3.884193
13	67.79175	0.541801	0.143896	3.765231
14	68.09066	0.580288	0.159646	3.634837
15	67.93393	0.615878	0.175468	3.50991
16	67.8603	0.653922	0.193707	3.375834
17	67.81691	0.690031	0.214753	3.213131
18	67.74131	0.721936	0.236855	3.048007
19	67.87257	0.749793	0.258237	2.903505
20	67.94895	0.77932	0.284194	2.742211
21	67.53993	0.779633	0.332679	2.343496
22	67.96857	0.77579	0.450935	1.720403

E-2: Open-Jet Force Measurements

The following tables summarize results from experiments performed in the Open-Jet Wind Tunnel. These tests did not consider a fuselage and should be used with caution. For test details, see chapters and appendix related to low Reynolds number tests and/or GA10 Balance. Nevertheless, these results provide information at additional Reynolds numbers not considered during Stability Tunnel Experiments.

Appendix Table E-6: Open-Jet Wind Tunnel Results - Coefficient of Lift

	Lift (1' Disc)					
AOA (º)	**Disc Alone**	**1.5" Chord, 4" Length**	**2" Chord, 3" Length**	**Disc Alone**	**1.5" Chord, 4" Length**	**2" Chord, 3" Length**
V (m/s)	**20**	**20**	**20**	**31.74**	**31.74**	**31.74**
0	-0.02401	-0.0711	0.03351	-0.03929	-0.04451	-0.03874
1	0.010715	-0.0187	0.080546	-0.00334	0.008061	0.01714
2	0.040056	0.030599	0.12252	0.033167	0.062034	0.064924
3	0.068706	0.076669	0.1687	0.062445	0.11416	0.12677
4	0.097232	0.12588	0.21178	0.09204	0.17022	0.18466
5	0.12198	0.16864	0.25679	0.12553	0.22056	0.2378
6	0.15275	0.20571	0.29734	0.15656	0.26409	0.28773
7	0.18486	0.24072	0.33891	0.18789	0.30162	0.32751
8	0.21118	0.27302	0.39434	0.22267	0.33559	0.36976
9	0.24377	0.30295	0.43113	0.2569	0.37017	0.40978
10	0.27388	0.33386	0.46395	0.2919	0.40248	0.46101
11	0.30519	0.3671	0.48912	0.32862	0.46214	0.49078
12	0.33953	0.42289	0.52252	0.36923	0.49483	0.52706
13	0.37469	0.45699	0.55591	0.40312	0.52244	0.55694
14	0.40398	0.48561	0.58292	0.43971	0.55741	0.61917
15	0.43567	0.5171	0.61479	0.47103	0.60662	0.64742
16	0.46936	0.54682	0.63781	0.50218	0.6338	0.6636
17	0.50181	0.57656	0.63118	0.53127	0.65761	0.67307
18	0.53086	0.60045	0.69123	0.56219	0.67561	0.67656
19	0.55457	0.62008	0.68902	0.58495	0.68442	0.68708
20	0.58021	0.63463	0.68843	0.60953	0.70184	0.68691
21	0.60429	0.64178	0.68301	0.62511	0.70852	0.69038
22	0.6297	0.67222	0.68078	0.64812	0.71751	0.69878

Appendix Table E-7: Open-Jet Wind Tunnel Results - Coefficient of Drag

	Drag (1' Disc)					
AOA (º)	**Disc Alone**	**1.5" Chord, 4" Length**	**2" Chord, 3" Length**	**Disc Alone**	**1.5" Chord, 4" Length**	**2" Chord, 3" Length**
V (m/s)	**20**	**20**	**20**	**31.74**	**31.74**	**31.74**
0	0.019532	0.032997	0.039985	0.029785	0.035585	0.029789
1	0.029205	0.038163	0.050638	0.032292	0.041241	0.034266
2	0.039122	0.047393	0.062134	0.037602	0.0467	0.039933
3	0.050035	0.057811	0.076321	0.04319	0.054042	0.049145
4	0.060938	0.070023	0.091132	0.048811	0.062891	0.059275
5	0.072046	0.083453	0.10792	0.056401	0.073591	0.070881
6	0.084837	0.097789	0.12632	0.063985	0.085381	0.084593
7	0.098414	0.11392	0.14689	0.07322	0.098792	0.098932
8	0.1125	0.13084	0.17277	0.084132	0.11305	0.11546
9	0.12858	0.14927	0.19599	0.096845	0.12841	0.13353
10	0.14489	0.16915	0.22007	0.11083	0.14431	0.15716
11	0.16403	0.19055	0.24283	0.12637	0.16914	0.17671
12	0.18528	0.22022	0.26932	0.14484	0.18891	0.20018
13	0.20784	0.24468	0.29763	0.1634	0.20749	0.22303
14	0.2305	0.26954	0.32524	0.18432	0.2313	0.25854
15	0.25511	0.29711	0.35606	0.20523	0.26069	0.2845
16	0.28214	0.32489	0.38546	0.22654	0.28518	0.30722
17	0.30951	0.35442	0.40435	0.2491	0.30955	0.32952
18	0.3367	0.38305	0.45425	0.27374	0.33164	0.3493
19	0.36387	0.41166	0.48025	0.29632	0.35284	0.37125
20	0.39411	0.43959	0.50672	0.32092	0.37861	0.39167
21	0.42379	0.46586	0.531	0.34371	0.39955	0.41141
22	0.45575	0.5065	0.5552	0.36953	0.42171	0.43291

Appendix Table E-8: Open-Jet Wind Tunnel Results - Coefficient of Pitch

	Pitch (1' Disc)					
AOA (º)	**Disc Alone**	**1.5" Chord, 4" Length**	**2" Chord, 3" Length**	**Disc Alone**	**1.5" Chord, 4" Length**	**2" Chord, 3" Length**
V (m/s)	**20**	**20**	**20**	**31.74**	**31.74**	**31.74**
0	0.005743	-0.00404	0.023511	0.002046	7.61E-05	0.00246
1	0.016122	0.007159	0.034708	0.011595	0.0111	0.014945
2	0.024939	0.017955	0.044367	0.021748	0.022444	0.025729
3	0.034159	0.027988	0.054878	0.030606	0.032835	0.039194
4	0.043579	0.038638	0.065125	0.039516	0.044612	0.051778
5	0.051806	0.04828	0.075672	0.049858	0.055814	0.063656
6	0.061967	0.057067	0.085224	0.05914	0.066358	0.0752
7	0.072014	0.065851	0.095971	0.068371	0.075946	0.084655
8	0.080107	0.074799	0.11037	0.078288	0.085055	0.095414
9	0.089395	0.083438	0.12037	0.087491	0.09375	0.10498
10	0.097325	0.091884	0.12815	0.095872	0.10148	0.11691
11	0.10599	0.1014	0.13356	0.10404	0.11463	0.12239
12	0.1147	0.1154	0.13818	0.11202	0.12029	0.12619
13	0.12223	0.12278	0.14071	0.11739	0.12383	0.1267
14	0.12745	0.12799	0.1408	0.12112	0.12511	0.13008
15	0.13152	0.13172	0.13795	0.12162	0.12723	0.1259
16	0.1329	0.13151	0.13324	0.12231	0.12417	0.11895
17	0.13499	0.13003	0.12373	0.11995	0.11844	0.11273
18	0.13592	0.12646	0.12427	0.11776	0.11649	0.10717
19	0.13438	0.12253	0.11647	0.11515	0.11117	0.10592
20	0.13068	0.11935	0.11152	0.11419	0.10683	0.10064
21	0.13121	0.11583	0.10739	0.11002	0.10433	0.099378
22	0.12964	0.11302	0.10671	0.10836	0.10376	0.099822

Appendix F: **Tabulated Data – Hover Force Measurements**

Figures shown in Chapter 4 present curves based upon experimental data of measured forces during hover experiments. The data points are summarized in the following tables for following research and design efforts.

Test Description			Test Parameters							Recorded Test Data				
Test	Description	Date	Collective Pitch Angle, º	Blade Chord, ft	Disc Radius, ft	Blades Length, ft	Tip Radius, ft	Blade T.E.	Ground Dist., in	RPM	Avg. Thrust, lb	Avg. Torque, in-lbs	StDev Thrust	StDev Torque
2a	14º - 108in	16-Jan-08	14	0.2	0.75	0.67	1.42	round	108	1755	16.88	81.22	1.27	0.90
2a	14º - 108in	16-Jan-08	14	0.2	0.75	0.67	1.42	round	108	2486	36.34	159.53	0.67	1.19
2a	14º - 108in	16-Jan-08	14	0.2	0.75	0.67	1.42	round	108	2925	49.31	217.89	1.39	1.33
2a	14º - 108in	16-Jan-08	14	0.2	0.75	0.67	1.42	round	108	3510	70.11	309.78	0.82	0.98
2b	14º - 54in	16-Jan-08	14	0.2	0.75	0.67	1.42	round	54	1755	21.47	84.41	0.57	0.59
2b	14º - 54in	16-Jan-08	14	0.2	0.75	0.67	1.42	round	54	2486	41.13	161.75	0.09	0.63
2b	14º - 54in	16-Jan-08	14	0.2	0.75	0.67	1.42	round	54	2925	55.67	218.29	0.88	0.51
2b	14º - 54in	16-Jan-08	14	0.2	0.75	0.67	1.42	round	54	3510	73.86	310.35	0.58	0.82
2c	14º - 9in	16-Jan-08	14	0.2	0.75	0.67	1.42	round	9	1755	31.53	91.58	0.48	0.91
2c	14º - 9in	16-Jan-08	14	0.2	0.75	0.67	1.42	round	9	2486	61.65	172.50	0.34	0.69
2c	14º - 9in	16-Jan-08	14	0.2	0.75	0.67	1.42	round	9	2925	81.12	234.66	0.92	0.61
2c	14º - 9in	16-Jan-08	14	0.2	0.75	0.67	1.42	round	9	3510	112.15	330.10	0.50	0.71
3a	16º - 108in	18-Jan-08	16	0.2	0.75	0.67	1.42	round	108	1755	22.34	100.02	0.88	1.65
3a	16º - 108in	18-Jan-08	16	0.2	0.75	0.67	1.42	round	108	2486	48.20	199.96	0.53	1.23
3a	16º - 108in	18-Jan-08	16	0.2	0.75	0.67	1.42	round	108	2925	62.49	271.63	1.09	1.56
3a	16º - 108in	18-Jan-08	16	0.2	0.75	0.67	1.42	round	108	3510	87.56	380.61	1.01	1.08
3b	16º - 54in	18-Jan-08	16	0.2	0.75	0.67	1.42	round	54	1755	25.78	102.62	0.53	0.84
3b	16º - 54in	18-Jan-08	16	0.2	0.75	0.67	1.42	round	54	2486	49.63	198.07	0.45	0.83
3b	16º - 54in	18-Jan-08	16	0.2	0.75	0.67	1.42	round	54	2925	66.69	270.32	0.49	0.89
3b	16º - 54in	18-Jan-08	16	0.2	0.75	0.67	1.42	round	54	3510	90.76	380.34	0.94	1.11
3c	16º - 9in	18-Jan-08	16	0.2	0.75	0.67	1.42	round	9	1755	36.77	110.11	0.78	2.32
3c	16º - 9in	18-Jan-08	16	0.2	0.75	0.67	1.42	round	9	2486	72.24	210.80	0.49	0.60
3c	16º - 9in	18-Jan-08	16	0.2	0.75	0.67	1.42	round	9	2925	98.07	288.66	1.52	0.58
3c	16º - 9in	18-Jan-08	16	0.2	0.75	0.67	1.42	round	9	3510	135.14	397.38	0.67	0.10

Test Description			Test Parameters							Recorded Test Data				
Date	Collective Pitch Angle, º	Blade Chord, ft	Date	Collective Pitch Angle, º	Blade Chord, ft	Date	Collective Pitch Angle, º	Blade Chord, ft	Date	Collective Pitch Angle, º	Blade Chord, ft	Date	Collective Pitch Angle, º	StDev Torque
4a	12º - 108in	24-Jan-08	12	0.2	0.75	0.67	1.42	round	108	1755	8.57	48.45	0.46	-1.12
4a	12º - 108in	24-Jan-08	12	0.2	0.75	0.67	1.42	round	108	2486	19.30	100.59	0.92	-0.39
4a	12º - 108in	24-Jan-08	12	0.2	0.75	0.67	1.42	round	108	2925	27.20	139.51	0.51	-0.97
4a	12º - 108in	24-Jan-08	12	0.2	0.75	0.67	1.42	round	108	3510	39.89	203.60	0.50	-1.19
4b	12º - 9in	24-Jan-08	12	0.2	0.75	0.67	1.42	round	9	1755	16.78	50.54	0.33	-0.49
4b	12º - 9in	24-Jan-08	12	0.2	0.75	0.67	1.42	round	9	2486	31.99	106.00	0.26	-0.28
4b	12º - 9in	24-Jan-08	12	0.2	0.75	0.67	1.42	round	9	2925	46.19	148.80	0.77	-0.36
4b	12º - 9in	24-Jan-08	12	0.2	0.75	0.67	1.42	round	9	3510	67.87	218.30	0.39	-0.85
4c	12º - 54in	24-Jan-08	12	0.2	0.75	0.67	1.42	round	54	1755	10.17	50.54	0.80	-0.55
4c	12º - 54in	24-Jan-08	12	0.2	0.75	0.67	1.42	round	54	2486	22.30	101.01	0.24	-2.42
4c	12º - 54in	24-Jan-08	12	0.2	0.75	0.67	1.42	round	54	2925	32.00	140.28	0.71	-0.85
4c	12º - 54in	24-Jan-08	12	0.2	0.75	0.67	1.42	round	54	3510	42.82	205.10	0.45	-0.30
5a	8º - 9in	29-Jan-08	8	0.2	0.75	0.67	1.42	round	9	1462	5.12	18.82	0.47	-0.84
5a	8º - 9in	29-Jan-08	8	0.2	0.75	0.67	1.42	round	9	2486	17.51	61.91	0.21	-0.22
5a	8º - 9in	29-Jan-08	8	0.2	0.75	0.67	1.42	round	9	3071	26.32	97.75	0.13	-0.22
5a	8º - 9in	29-Jan-08	8	0.2	0.75	0.67	1.42	round	9	3217	28.89	107.74	0.13	-0.17
5b	8º - 54in	29-Jan-08	8	0.2	0.75	0.67	1.42	round	54	1462	5.29	17.34	0.19	-0.73
5b	8º - 54in	29-Jan-08	8	0.2	0.75	0.67	1.42	round	54	2486	13.42	58.64	0.23	-0.77
5b	8º - 54in	29-Jan-08	8	0.2	0.75	0.67	1.42	round	54	3071	18.44	94.14	0.18	-0.63
5b	8º - 54in	29-Jan-08	8	0.2	0.75	0.67	1.42	round	54	3217	19.81	104.15	0.27	-0.90
5c	8º -108in	29-Jan-08	8	0.2	0.75	0.67	1.42	round	108	1462	2.07	18.70	0.28	-1.38
5c	8º -108in	29-Jan-08	8	0.2	0.75	0.67	1.42	round	108	2486	9.56	61.02	0.43	-0.50
5c	8º -108in	29-Jan-08	8	0.2	0.75	0.67	1.42	round	108	3071	14.29	97.12	0.26	-0.42
5c	8º -108in	29-Jan-08	8	0.2	0.75	0.67	1.42	round	108	3217	15.50	106.88	0.24	-0.21

Test Description			Calculated Quantities of Interest				Reference Area includes Disc		Reference Area is Disc Removed	
Test	Description	Date	Tip velocity, fps	Total Area, sq ft	Disc Removed Area, sq ft	Solidity	Thrust Coefficient, Ct	Power Coefficient, CP	Thrust Coefficient, Ct	Power Coefficient, CP
2a	14º - 108in	16-Jan-08	260.97	6.335	4.568	1.17E-01	1.68E-02	4.73E-03	2.32E-02	6.56E-03
2a	14º - 108in	16-Jan-08	369.67	6.335	4.568	1.17E-01	1.80E-02	4.63E-03	2.49E-02	6.42E-03
2a	14º - 108in	16-Jan-08	434.95	6.335	4.568	1.17E-01	1.76E-02	4.57E-03	2.44E-02	6.33E-03
2a	14º - 108in	16-Jan-08	521.94	6.335	4.568	1.17E-01	1.74E-02	4.51E-03	2.41E-02	6.25E-03
2b	14º - 54in	16-Jan-08	260.97	6.335	4.568	1.17E-01	2.13E-02	4.91E-03	2.95E-02	6.82E-03
2b	14º - 54in	16-Jan-08	369.67	6.335	4.568	1.17E-01	2.03E-02	4.69E-03	2.82E-02	6.51E-03
2b	14º - 54in	16-Jan-08	434.95	6.335	4.568	1.17E-01	1.99E-02	4.57E-03	2.76E-02	6.34E-03
2b	14º - 54in	16-Jan-08	521.94	6.335	4.568	1.17E-01	1.83E-02	4.52E-03	2.54E-02	6.26E-03
2c	14º - 9in	16-Jan-08	260.97	6.335	4.568	1.17E-01	3.13E-02	5.33E-03	4.34E-02	7.39E-03
2c	14º - 9in	16-Jan-08	369.67	6.335	4.568	1.17E-01	3.05E-02	5.00E-03	4.23E-02	6.94E-03
2c	14º - 9in	16-Jan-08	434.95	6.335	4.568	1.17E-01	2.90E-02	4.92E-03	4.02E-02	6.82E-03
2c	14º - 9in	16-Jan-08	521.94	6.335	4.568	1.17E-01	2.78E-02	4.80E-03	3.86E-02	6.66E-03
3a	16º - 108in	18-Jan-08	260.97	6.335	4.568	1.17E-01	2.22E-02	5.82E-03	3.07E-02	8.08E-03
3a	16º - 108in	18-Jan-08	369.67	6.335	4.568	1.17E-01	2.38E-02	5.80E-03	3.30E-02	8.05E-03
3a	16º - 108in	18-Jan-08	434.95	6.335	4.568	1.17E-01	2.23E-02	5.69E-03	3.09E-02	7.89E-03
3a	16º - 108in	18-Jan-08	521.94	6.335	4.568	1.17E-01	2.17E-02	5.54E-03	3.01E-02	7.68E-03
3b	16º - 54in	18-Jan-08	260.97	6.335	4.568	1.17E-01	2.56E-02	5.97E-03	3.55E-02	8.28E-03
3b	16º - 54in	18-Jan-08	369.67	6.335	4.568	1.17E-01	2.45E-02	5.75E-03	3.40E-02	7.97E-03
3b	16º - 54in	18-Jan-08	434.95	6.335	4.568	1.17E-01	2.38E-02	5.67E-03	3.30E-02	7.86E-03
3b	16º - 54in	18-Jan-08	521.94	6.335	4.568	1.17E-01	2.25E-02	5.54E-03	3.12E-02	7.68E-03
3c	16º - 9in	18-Jan-08	260.97	6.335	4.568	1.17E-01	3.65E-02	6.41E-03	5.06E-02	8.89E-03
3c	16º - 9in	18-Jan-08	369.67	6.335	4.568	1.17E-01	3.57E-02	6.12E-03	4.95E-02	8.48E-03
3c	16º - 9in	18-Jan-08	434.95	6.335	4.568	1.17E-01	3.50E-02	6.05E-03	4.86E-02	8.39E-03
3c	16º - 9in	18-Jan-08	521.94	6.335	4.568	1.17E-01	3.35E-02	5.78E-03	4.65E-02	8.02E-03

Test Description			Calculated Quantities of Interest				Reference Area includes Disc		Reference Area is Disc Removed	
Test	Description	Date	Tip velocity, fps	Total Area, sq ft	Disc Removed Area, sq ft	Solidity	Thrust Coefficient, Ct	Power Coefficient, CP	Thrust Coefficient, Ct	Power Coefficient, CP
4a	12º - 108in	24-Jan-08	260.97	6.335	4.568	1.17E-01	8.50E-03	2.82E-03	1.18E-02	3.91E-03
4a	12º - 108in	24-Jan-08	369.67	6.335	4.568	1.17E-01	9.54E-03	2.92E-03	1.32E-02	4.05E-03
4a	12º - 108in	24-Jan-08	434.95	6.335	4.568	1.17E-01	9.71E-03	2.92E-03	1.35E-02	4.05E-03
4a	12º - 108in	24-Jan-08	521.94	6.335	4.568	1.17E-01	9.89E-03	2.96E-03	1.37E-02	4.11E-03
4b	12º - 9in	24-Jan-08	260.97	6.335	4.568	1.17E-01	1.66E-02	2.94E-03	2.31E-02	4.08E-03
4b	12º - 9in	24-Jan-08	369.67	6.335	4.568	1.17E-01	1.58E-02	3.08E-03	2.19E-02	4.27E-03
4b	12º - 9in	24-Jan-08	434.95	6.335	4.568	1.17E-01	1.65E-02	3.12E-03	2.29E-02	4.32E-03
4b	12º - 9in	24-Jan-08	521.94	6.335	4.568	1.17E-01	1.68E-02	3.18E-03	2.33E-02	4.41E-03
4c	12º - 54in	24-Jan-08	260.97	6.335	4.568	1.17E-01	1.01E-02	2.94E-03	1.40E-02	4.08E-03
4c	12º - 54in	24-Jan-08	369.67	6.335	4.568	1.17E-01	1.10E-02	2.93E-03	1.53E-02	4.06E-03
4c	12º - 54in	24-Jan-08	434.95	6.335	4.568	1.17E-01	1.14E-02	2.94E-03	1.58E-02	4.08E-03
4c	12º - 54in	24-Jan-08	521.94	6.335	4.568	1.17E-01	1.06E-02	2.98E-03	1.47E-02	4.14E-03
5a	8º - 9in	29-Jan-08	217.40	6.335	4.568	1.17E-01	7.32E-03	1.58E-03	1.02E-02	2.19E-03
5a	8º - 9in	29-Jan-08	369.67	6.335	4.568	1.17E-01	8.65E-03	1.80E-03	1.20E-02	2.49E-03
5a	8º - 9in	29-Jan-08	456.66	6.335	4.568	1.17E-01	8.53E-03	1.86E-03	1.18E-02	2.58E-03
5a	8º - 9in	29-Jan-08	478.37	6.335	4.568	1.17E-01	8.53E-03	1.87E-03	1.18E-02	2.59E-03
5b	8º - 54in	29-Jan-08	217.40	6.335	4.568	1.17E-01	7.57E-03	1.45E-03	1.05E-02	2.02E-03
5b	8º - 54in	29-Jan-08	369.67	6.335	4.568	1.17E-01	6.64E-03	1.70E-03	9.20E-03	2.36E-03
5b	8º - 54in	29-Jan-08	456.66	6.335	4.568	1.17E-01	5.97E-03	1.79E-03	8.29E-03	2.48E-03
5b	8º - 54in	29-Jan-08	478.37	6.335	4.568	1.17E-01	5.85E-03	1.80E-03	8.11E-03	2.50E-03
5c	8º -108in	29-Jan-08	217.40	6.335	4.568	1.17E-01	2.95E-03	1.57E-03	4.10E-03	2.18E-03
5c	8º -108in	29-Jan-08	369.67	6.335	4.568	1.17E-01	4.72E-03	1.77E-03	6.55E-03	2.46E-03
5c	8º -108in	29-Jan-08	456.66	6.335	4.568	1.17E-01	4.63E-03	1.85E-03	6.42E-03	2.56E-03
5c	8º -108in	29-Jan-08	478.37	6.335	4.568	1.17E-01	4.57E-03	1.85E-03	6.34E-03	2.57E-03

Appendix G: **Tabulated Data – Wake Velocity Measurements**

Figures shown in Chapter 4 present curves based upon experimental data of measured wind velocities downstream of the rotor during ground independent hover. These velocities were measured for a rotational speed of 2,486 RPM at a collective pitch angle of 14º. Velocities have been reduced (i.e. divided) by the tip velocity. Downstream distance and radial location have been divided by the total rotor diameter. Dimensionless data is listed in the following tables.

	u component of velocity (divided by tip speed)						
Radial Location (y / D)	Non. Dim. Elevation (x / D):						
	0.006948	0.036359	0.095183	0.182955	0.301065	0.448124	0.687124
0.007446	5.486E-03	5.974E-03	2.889E-02	3.408E-02	-1.645E-03	3.165E-02	2.391E-02
0.022338	-1.128E-02	1.654E-02	3.946E-03	-4.348E-03	3.422E-03	-3.033E-02	2.079E-02
0.037230	-1.735E-02	-1.245E-02	1.792E-02	-1.338E-03	1.360E-03	-2.214E-02	-4.109E-03
0.052123	-6.265E-03	-2.910E-04	-1.335E-02	-2.534E-02	-1.756E-02	-3.686E-02	1.875E-02
0.067014	6.187E-04	-2.464E-05	-1.251E-02	-8.930E-03	-3.418E-02	-2.796E-02	3.582E-02
0.081906	-2.982E-04	-9.761E-03	1.632E-03	-1.247E-02	-1.003E-02	-2.167E-02	5.023E-02
0.096798	-5.911E-03	-9.748E-03	-9.180E-03	-2.370E-03	-6.500E-03	9.513E-03	5.746E-02
0.111691	6.651E-03	-8.143E-03	-1.532E-02	1.125E-02	1.616E-02	2.381E-02	6.193E-02
0.126582	-1.240E-02	-1.912E-02	-8.551E-03	-4.427E-04	2.395E-02	1.425E-02	9.468E-02
0.141474	-1.661E-02	5.746E-03	-8.093E-03	8.975E-03	-5.116E-03	3.395E-02	1.093E-01
0.156366	-1.891E-02	4.505E-03	-8.365E-03	1.017E-03	-1.278E-02	5.072E-02	9.141E-02
0.171259	-8.021E-03	-1.516E-02	-1.056E-02	6.662E-03	2.608E-03	7.440E-02	1.092E-01
0.186151	-1.274E-02	-1.219E-05	-9.934E-03	-8.171E-03	1.264E-02	8.190E-02	1.134E-01
0.201042	6.216E-04	-9.626E-03	4.488E-03	-4.788E-03	2.728E-02	9.282E-02	1.377E-01
0.215934	7.802E-03	1.085E-02	2.015E-03	2.794E-03	5.734E-02	1.271E-01	1.342E-01
0.230827	-1.466E-02	-9.043E-03	5.209E-03	1.598E-02	5.744E-02	1.250E-01	1.475E-01
0.245719	1.504E-03	-7.480E-03	-1.752E-02	3.493E-02	8.002E-02	1.369E-01	1.680E-01
0.260610	-7.023E-03	-5.226E-04	5.777E-03	6.567E-02	1.004E-01	1.102E-01	1.759E-01
0.275503	-1.889E-03	3.814E-03	3.503E-02	8.573E-02	1.310E-01	1.615E-01	1.728E-01
0.290395	6.016E-02	4.769E-02	8.849E-02	1.244E-01	1.607E-01	1.824E-01	1.768E-01
0.305287	9.591E-02	1.072E-01	1.217E-01	1.573E-01	1.740E-01	1.781E-01	1.630E-01
0.320178	1.117E-01	1.385E-01	1.523E-01	1.714E-01	1.809E-01	1.818E-01	1.559E-01
0.335071	1.332E-01	1.486E-01	1.714E-01	1.876E-01	1.918E-01	1.698E-01	1.560E-01
0.349963	1.447E-01	1.605E-01	1.839E-01	1.922E-01	1.893E-01	1.639E-01	1.306E-01
0.364855	1.538E-01	1.742E-01	1.950E-01	2.016E-01	1.724E-01	1.537E-01	1.106E-01
0.379746	1.586E-01	1.820E-01	2.031E-01	2.090E-01	1.566E-01	1.164E-01	1.000E-01
0.394639	1.699E-01	1.930E-01	2.087E-01	1.829E-01	1.217E-01	8.913E-02	8.027E-02
0.409531	1.736E-01	1.994E-01	1.904E-01	1.408E-01	1.097E-01	7.383E-02	6.832E-02
0.424423	1.792E-01	1.867E-01	1.288E-01	8.035E-02	7.707E-02	5.618E-02	6.629E-02
0.439314	1.494E-01	1.173E-01	5.405E-02	5.313E-02	4.597E-02	4.471E-02	4.739E-02
0.454207	4.939E-02	5.690E-03	3.789E-02	3.636E-02	1.978E-02	3.482E-02	3.748E-02
0.469099	-2.353E-02	-7.246E-03	4.877E-03	2.784E-02	2.877E-02	2.694E-02	2.586E-02
0.483991	-8.416E-03	-1.146E-02	7.210E-03	1.648E-02	2.043E-02	2.658E-02	2.030E-02
0.498883	8.291E-03	1.815E-02	3.299E-03	1.433E-02	1.574E-02	2.129E-02	1.683E-02
0.513775	9.230E-03	1.208E-02	8.140E-03	1.539E-02	1.416E-02	2.255E-02	2.166E-02
0.528667	1.149E-02	1.041E-02	1.811E-02	1.577E-02	1.916E-02	2.207E-02	1.970E-02
0.543560	1.252E-02	1.282E-02	1.378E-02	1.877E-02	1.693E-02	2.332E-02	1.702E-02
0.558452	1.290E-02	1.728E-02	9.571E-03	1.645E-02	1.641E-02	2.424E-02	1.876E-02
0.573343	1.525E-02	1.363E-02	6.288E-03	1.169E-02	1.995E-02	2.358E-02	2.035E-02
0.588235	1.179E-02	1.399E-02	1.170E-02	1.846E-02	2.160E-02	2.490E-02	2.123E-02

	v component of velocity (divided by tip speed)						
Radial Location (y / D)	**Non. Dim. Elevation (x / D):**						
	0.006948	**0.036359**	**0.095183**	**0.182955**	**0.301065**	**0.448124**	**0.687124**
0.007446	-3.137E-02	-3.076E-02	-3.286E-02	-2.884E-02	7.991E-02	5.495E-02	4.102E-02
0.022338	-2.013E-02	8.494E-03	-3.237E-02	-3.762E-03	2.787E-02	4.983E-02	4.157E-02
0.037230	-1.504E-02	-2.241E-02	5.378E-03	-1.975E-02	2.724E-02	3.197E-02	2.958E-02
0.052123	-1.535E-02	-1.828E-02	-4.496E-03	-2.188E-02	2.377E-02	3.223E-02	3.243E-02
0.067014	-2.362E-02	-2.346E-02	5.038E-02	3.775E-02	3.497E-02	3.631E-02	3.474E-02
0.081906	-2.273E-02	-1.966E-02	-6.804E-03	1.595E-02	2.136E-02	3.228E-02	2.447E-02
0.096798	-1.887E-03	-1.934E-02	-3.465E-03	1.117E-02	2.162E-02	1.466E-03	1.639E-02
0.111691	-2.051E-03	-3.486E-03	-1.467E-02	4.750E-03	1.050E-02	1.478E-02	6.265E-03
0.126582	-5.896E-03	-5.781E-03	-1.689E-02	1.862E-02	8.497E-03	1.027E-04	7.263E-03
0.141474	-7.372E-03	-1.978E-03	-1.677E-02	3.465E-03	-6.383E-03	-1.458E-03	5.566E-03
0.156366	-5.460E-03	-2.632E-03	1.261E-02	-6.476E-03	-1.077E-02	-1.540E-02	5.944E-03
0.171259	-4.843E-03	-3.602E-03	9.422E-03	-2.604E-03	-1.427E-02	-1.686E-02	1.764E-03
0.186151	-5.990E-03	1.068E-02	1.048E-02	-3.702E-03	-2.123E-02	-1.800E-02	3.590E-04
0.201042	2.317E-04	9.665E-03	-6.571E-03	-8.091E-03	-2.721E-02	-1.796E-02	-3.447E-03
0.215934	4.767E-03	1.238E-02	2.133E-02	-1.588E-02	-2.720E-02	-3.085E-02	-6.793E-04
0.230827	1.396E-02	5.651E-03	-1.356E-02	-2.946E-02	-2.648E-02	-5.288E-02	-3.591E-03
0.245719	2.589E-02	3.748E-03	-4.155E-03	-2.969E-02	-3.169E-02	-3.077E-02	-5.771E-03
0.260610	3.550E-02	6.339E-02	-1.100E-02	-3.285E-02	-2.856E-02	-3.672E-02	-1.121E-02
0.275503	4.768E-02	-8.952E-03	-1.701E-02	-3.568E-02	-4.451E-02	-2.997E-02	-4.281E-04
0.290395	1.596E-02	-2.334E-03	-2.621E-02	-4.008E-02	-4.677E-02	-3.001E-02	1.814E-03
0.305287	2.648E-02	-3.029E-03	-2.702E-02	-4.842E-02	-4.738E-02	-2.702E-02	-1.055E-03
0.320178	1.833E-02	-6.539E-03	-3.291E-02	-4.268E-02	-4.080E-02	-2.078E-02	-4.068E-03
0.335071	8.880E-03	-8.316E-03	-3.081E-02	-4.849E-02	-3.886E-02	-1.212E-02	4.463E-03
0.349963	-3.573E-03	-7.975E-03	-3.252E-02	-4.064E-02	-3.412E-02	-1.220E-02	7.165E-03
0.364855	-1.738E-02	-1.792E-02	-3.647E-02	-4.006E-02	-2.854E-02	-3.870E-03	6.260E-03
0.379746	-2.552E-02	-2.961E-02	-3.577E-02	-3.873E-02	-1.419E-02	-8.022E-04	5.213E-03
0.394639	-4.329E-02	-4.127E-02	-3.730E-02	-2.531E-02	-9.051E-03	4.219E-03	8.637E-03
0.409531	-5.204E-02	-4.658E-02	-3.065E-02	-7.392E-03	-2.143E-03	3.119E-03	8.005E-03
0.424423	-6.678E-02	-4.478E-02	-1.186E-02	-1.588E-03	-1.410E-04	5.838E-03	1.293E-02
0.439314	-6.176E-02	-1.451E-02	3.375E-03	7.691E-04	7.071E-04	4.701E-03	6.016E-03
0.454207	-1.232E-02	1.741E-02	5.948E-03	2.520E-03	1.431E-03	3.553E-03	5.969E-03
0.469099	2.595E-02	1.519E-02	8.230E-03	3.241E-04	4.056E-03	3.571E-03	3.290E-03
0.483991	1.837E-02	-3.577E-03	-3.270E-03	-1.454E-02	8.752E-04	-1.068E-02	-1.065E-02
0.498883	-1.539E-02	-1.058E-02	-1.428E-02	-1.242E-02	-1.501E-02	-1.248E-02	-1.135E-02
0.513775	-1.349E-02	-2.848E-03	-1.094E-02	-1.341E-02	-1.376E-02	-1.095E-02	-1.271E-02
0.528667	1.162E-02	-1.033E-02	-1.432E-02	-1.385E-02	-1.368E-02	-1.061E-02	-1.226E-02
0.543560	-1.496E-02	-1.368E-02	-1.276E-02	-1.186E-02	-1.456E-02	-1.212E-02	-1.052E-02
0.558452	-1.699E-02	-1.507E-02	-8.072E-03	-1.388E-02	-1.376E-02	-1.069E-02	-1.011E-02
0.573343	-1.444E-02	-1.207E-02	-1.151E-02	-1.517E-02	-1.454E-02	-1.131E-02	-1.090E-02
0.588235	-1.678E-02	-1.344E-02	-1.188E-02	-1.237E-02	-1.473E-02	-1.289E-02	-1.264E-02

	w component of velocity (divided by tip speed)						
Radial Location (y / D)	**Non. Dim. Elevation (x / D):**						
	0.006948	**0.036359**	**0.095183**	**0.182955**	**0.301065**	**0.448124**	**0.687124**
0.007446	-1.881E-02	-1.207E-02	-1.830E-02	-1.562E-02	4.562E-02	-8.962E-04	-1.029E-02
0.022338	-3.166E-02	-5.211E-02	-2.848E-02	-3.754E-02	-2.050E-02	-1.949E-02	-4.260E-02
0.037230	-4.482E-02	-8.871E-03	-7.063E-02	-4.098E-03	4.160E-03	-1.047E-02	-6.278E-02
0.052123	-3.132E-02	1.120E-02	-4.766E-02	-1.107E-02	-3.505E-02	-3.658E-02	-8.058E-02
0.067014	-6.364E-03	3.499E-04	-4.586E-02	-4.388E-02	-1.654E-02	-7.204E-02	-8.755E-02
0.081906	5.473E-03	-3.098E-02	-4.759E-02	-3.595E-02	-5.369E-02	-7.827E-02	-1.042E-01
0.096798	-4.192E-02	-2.324E-02	-3.794E-02	-4.209E-02	-6.322E-02	-1.262E-01	-1.045E-01
0.111691	-4.464E-02	-4.009E-02	-3.075E-03	-3.893E-02	-6.681E-02	-9.848E-02	-9.985E-02
0.126582	-3.161E-02	-2.508E-02	-1.773E-02	-3.669E-02	5.387E-03	-1.339E-01	-9.648E-02
0.141474	-2.666E-02	-3.729E-02	-1.218E-02	-3.126E-02	-5.992E-02	-9.632E-02	-9.957E-02
0.156366	-2.543E-02	-3.216E-02	-1.452E-02	-2.712E-02	-5.794E-02	-8.865E-02	-8.756E-02
0.171259	-2.711E-02	-1.978E-02	-4.225E-03	-3.433E-02	-6.119E-02	-8.727E-02	-9.089E-02
0.186151	-2.452E-02	-3.381E-02	9.242E-04	-3.042E-02	-6.981E-02	-7.852E-02	-8.708E-02
0.201042	-3.072E-02	-1.732E-02	3.083E-03	-3.515E-02	-6.672E-02	-7.556E-02	-8.949E-02
0.215934	-3.096E-02	1.022E-02	4.531E-03	-4.389E-02	-6.692E-02	-7.907E-02	-7.933E-02
0.230827	-1.062E-02	8.743E-03	5.622E-04	-5.494E-02	-6.059E-02	-6.552E-02	-7.565E-02
0.245719	-9.021E-03	-7.998E-03	-2.434E-02	-5.601E-02	-5.702E-02	-6.073E-02	-8.406E-02
0.260610	-1.322E-02	1.164E-02	-4.212E-02	-5.904E-02	-5.130E-02	-8.827E-02	-7.906E-02
0.275503	-9.529E-03	-4.232E-02	-5.331E-02	-5.133E-02	-5.670E-02	-6.276E-02	-8.684E-02
0.290395	-6.977E-02	-6.187E-02	-6.007E-02	-5.419E-02	-5.701E-02	-7.406E-02	-8.737E-02
0.305287	-7.329E-02	-6.601E-02	-5.848E-02	-5.421E-02	-6.517E-02	-7.463E-02	-8.008E-02
0.320178	-7.280E-02	-6.643E-02	-5.814E-02	-5.190E-02	-6.080E-02	-7.656E-02	-7.463E-02
0.335071	-6.659E-02	-6.859E-02	-5.664E-02	-6.025E-02	-6.779E-02	-8.152E-02	-7.828E-02
0.349963	-5.759E-02	-6.264E-02	-5.337E-02	-6.159E-02	-7.649E-02	-8.403E-02	-7.692E-02
0.364855	-4.966E-02	-4.741E-02	-5.234E-02	-6.876E-02	-7.910E-02	-8.194E-02	-6.766E-02
0.379746	-4.803E-02	-5.159E-02	-5.894E-02	-8.074E-02	-8.460E-02	-7.028E-02	-6.110E-02
0.394639	-4.827E-02	-5.320E-02	-7.186E-02	-8.280E-02	-7.072E-02	-7.263E-02	-5.711E-02
0.409531	-5.503E-02	-6.351E-02	-9.043E-02	-8.260E-02	-7.427E-02	-5.746E-02	-5.298E-02
0.424423	-6.461E-02	-9.003E-02	-9.722E-02	-6.533E-02	-5.617E-02	-4.695E-02	-5.418E-02
0.439314	-1.001E-01	-9.791E-02	-6.645E-02	-4.944E-02	-4.298E-02	-3.740E-02	-3.765E-02
0.454207	-1.119E-01	-6.512E-02	-4.019E-02	-3.638E-02	-2.720E-02	-2.463E-02	-2.431E-02
0.469099	-3.563E-02	-3.085E-02	-2.660E-02	-1.882E-02	-2.638E-02	-1.828E-02	-2.399E-02
0.483991	-8.033E-03	6.048E-03	-2.824E-03	7.207E-03	-1.734E-02	6.805E-03	8.623E-03
0.498883	7.153E-03	1.116E-02	1.090E-02	1.032E-02	1.049E-02	7.179E-03	7.844E-03
0.513775	5.331E-03	1.131E-02	1.102E-02	1.052E-02	8.814E-03	9.740E-03	8.328E-03
0.528667	1.089E-02	1.059E-02	1.173E-02	9.839E-03	1.146E-02	9.500E-03	8.446E-03
0.543560	1.004E-02	1.143E-02	1.146E-02	9.853E-03	9.826E-03	9.806E-03	9.927E-03
0.558452	9.299E-03	1.060E-02	1.676E-02	1.158E-02	9.635E-03	9.768E-03	1.042E-02
0.573343	9.922E-03	1.014E-02	1.436E-02	1.240E-02	1.090E-02	1.010E-02	1.080E-02
0.588235	9.236E-03	1.167E-02	1.174E-02	1.007E-02	1.069E-02	1.077E-02	1.061E-02

	Static Pressure (divided by dynamic pressure from tip velocity)						
Radial Location (y / D)	Non. Dim. Elevation (x / D):						
	0.006948	0.036359	0.095183	0.182955	0.301065	0.448124	0.687124
0.007446	-2.673E-02	-2.444E-02	-2.889E-02	-2.999E-02	-3.535E-02	-2.810E-02	-3.345E-02
0.022338	-2.376E-02	-2.931E-02	-2.833E-02	-2.625E-02	-3.184E-02	-2.672E-02	-2.721E-02
0.037230	-2.207E-02	-1.788E-02	-2.470E-02	-2.664E-02	-2.918E-02	-2.693E-02	-2.220E-02
0.052123	-1.687E-02	-1.230E-02	-1.915E-02	-2.135E-02	-2.006E-02	-2.077E-02	-2.161E-02
0.067014	-1.252E-02	-1.225E-02	-1.758E-02	-1.932E-02	-1.943E-02	-1.641E-02	-1.703E-02
0.081906	-1.029E-02	-1.494E-02	-1.537E-02	-1.493E-02	-1.749E-02	-1.445E-02	-1.367E-02
0.096798	-1.326E-02	-1.257E-02	-1.368E-02	-1.538E-02	-1.649E-02	-1.621E-02	-1.380E-02
0.111691	-1.230E-02	-1.251E-02	-1.247E-02	-1.521E-02	-1.553E-02	-9.524E-03	-8.123E-03
0.126582	-1.129E-02	-1.119E-02	-1.243E-02	-1.464E-02	-1.378E-02	-1.461E-02	-9.391E-03
0.141474	-1.027E-02	-1.208E-02	-1.229E-02	-1.355E-02	-1.054E-02	-6.252E-03	-9.520E-03
0.156366	-1.016E-02	-1.186E-02	-1.278E-02	-1.309E-02	-7.557E-03	-4.211E-03	-6.387E-03
0.171259	-1.032E-02	-1.087E-02	-1.145E-02	-1.218E-02	-7.621E-03	-3.568E-03	-5.367E-03
0.186151	-9.548E-03	-1.114E-02	-1.129E-02	-1.108E-02	-6.335E-03	-3.679E-03	-4.872E-03
0.201042	-9.861E-03	-1.125E-02	-1.131E-02	-9.764E-03	-5.230E-03	-3.297E-03	-4.352E-03
0.215934	-9.626E-03	-9.783E-03	-1.034E-02	-9.983E-03	-5.910E-03	-2.480E-03	-4.768E-03
0.230827	-9.165E-03	-9.438E-03	-1.068E-02	-8.003E-03	-3.847E-03	-1.960E-03	-5.285E-03
0.245719	-1.046E-02	-9.838E-03	-9.694E-03	-7.584E-03	-2.815E-03	-2.327E-03	-3.942E-03
0.260610	-1.160E-02	-1.340E-02	-9.231E-03	-6.685E-03	-3.604E-03	-2.679E-03	-3.131E-03
0.275503	-9.881E-03	-9.685E-03	-8.398E-03	-5.384E-03	-4.011E-03	-3.154E-03	-4.735E-03
0.290395	-8.373E-03	-8.713E-03	-8.923E-03	-7.605E-03	-4.405E-03	-3.304E-03	-5.716E-03
0.305287	-5.462E-03	-9.061E-03	-8.320E-03	-6.801E-03	-4.847E-03	-3.184E-03	-5.086E-03
0.320178	-1.804E-03	-6.918E-03	-7.604E-03	-7.352E-03	-5.050E-03	-3.934E-03	-3.409E-03
0.335071	-5.376E-04	-4.390E-03	-7.549E-03	-6.629E-03	-6.067E-03	-3.128E-03	-4.434E-03
0.349963	2.534E-03	-3.187E-03	-7.213E-03	-5.269E-03	-5.751E-03	-5.153E-03	-3.858E-03
0.364855	4.553E-03	-2.222E-03	-6.021E-03	-5.642E-03	-5.546E-03	-4.320E-03	-2.269E-03
0.379746	6.091E-03	-1.372E-03	-5.750E-03	-7.216E-03	-6.317E-03	-2.197E-03	-3.142E-03
0.394639	6.135E-03	-1.527E-03	-5.552E-03	-5.877E-03	-5.531E-03	-2.809E-03	-2.357E-03
0.409531	6.262E-03	-3.410E-03	-7.700E-03	-7.224E-03	-3.926E-03	-2.469E-03	-2.598E-03
0.424423	-1.917E-04	-8.501E-03	-9.173E-03	-4.384E-03	-3.821E-03	-2.309E-03	-2.281E-03
0.439314	-5.044E-03	-1.351E-02	-5.216E-03	-2.792E-03	-2.505E-03	-2.520E-03	-2.544E-03
0.454207	-1.674E-02	-7.595E-03	-3.955E-03	-2.406E-03	-2.416E-03	-2.153E-03	-2.498E-03
0.469099	-1.121E-02	-4.797E-03	-2.993E-03	-2.178E-03	-2.446E-03	-1.791E-03	-2.152E-03
0.483991	-7.058E-03	-3.773E-03	-2.414E-03	-1.633E-03	-2.261E-03	-1.585E-03	-1.992E-03
0.498883	-3.630E-03	-3.090E-03	-1.777E-03	-1.085E-03	-1.599E-03	-1.126E-03	-1.606E-03
0.513775	-2.875E-03	-2.753E-03	-1.637E-03	-8.260E-04	-1.347E-03	-1.045E-03	-1.567E-03
0.528667	-2.610E-03	-2.406E-03	-1.770E-03	-6.902E-04	-1.346E-03	-9.655E-04	-1.539E-03
0.543560	-1.929E-03	-2.201E-03	-1.603E-03	-7.497E-04	-1.299E-03	-9.571E-04	-1.306E-03
0.558452	-1.724E-03	-2.438E-03	-1.538E-03	-6.741E-04	-1.204E-03	-9.771E-04	-1.224E-03
0.573343	-1.759E-03	-2.277E-03	-1.364E-03	-3.592E-04	-1.276E-03	-9.460E-04	-1.336E-03
0.588235	-1.401E-03	-2.159E-03	-1.554E-03	-7.332E-04	-1.322E-03	-9.323E-04	-1.320E-03

Radial Location (y / D)	Total Pressure (divided by dynamic pressure from tip velocity)						
	Non. Dim. Elevation (x / D):						
	0.006948	**0.036359**	**0.095183**	**0.182955**	**0.301065**	**0.448124**	**0.687124**
0.007446	-2.535E-02	-2.331E-02	-2.663E-02	-2.774E-02	-2.685E-02	-2.406E-02	-3.108E-02
0.022338	-2.199E-02	-2.623E-02	-2.645E-02	-2.480E-02	-3.063E-02	-2.292E-02	-2.322E-02
0.037230	-1.953E-02	-1.657E-02	-1.935E-02	-2.623E-02	-2.842E-02	-2.464E-02	-1.735E-02
0.052123	-1.561E-02	-1.184E-02	-1.667E-02	-2.010E-02	-1.795E-02	-1.566E-02	-1.369E-02
0.067014	-1.192E-02	-1.170E-02	-1.277E-02	-1.588E-02	-1.676E-02	-9.094E-03	-6.835E-03
0.081906	-9.737E-03	-1.349E-02	-1.305E-02	-1.322E-02	-1.404E-02	-6.789E-03	3.555E-04
0.096798	-1.145E-02	-1.156E-02	-1.214E-02	-1.347E-02	-1.197E-02	-1.390E-04	7.397E-04
0.111691	-1.025E-02	-1.082E-02	-1.201E-02	-1.354E-02	-1.068E-02	9.975E-04	5.772E-03
0.126582	-1.010E-02	-1.016E-02	-1.176E-02	-1.294E-02	-9.135E-03	3.577E-03	8.999E-03
0.141474	-9.223E-03	-1.065E-02	-1.180E-02	-1.248E-02	-6.868E-03	4.218E-03	1.246E-02
0.156366	-9.123E-03	-1.079E-02	-1.229E-02	-1.231E-02	-3.907E-03	6.495E-03	9.728E-03
0.171259	-9.493E-03	-1.024E-02	-1.123E-02	-1.095E-02	-3.652E-03	9.916E-03	1.490E-02
0.186151	-8.746E-03	-9.877E-03	-1.105E-02	-1.008E-02	-8.317E-04	9.564E-03	1.566E-02
0.201042	-8.914E-03	-1.076E-02	-1.110E-02	-8.436E-03	7.275E-04	1.140E-02	2.272E-02
0.215934	-8.580E-03	-9.407E-03	-9.862E-03	-7.789E-03	2.627E-03	2.096E-02	1.963E-02
0.230827	-8.640E-03	-9.247E-03	-1.047E-02	-3.847E-03	3.852E-03	2.084E-02	2.230E-02
0.245719	-9.517E-03	-9.569E-03	-8.775E-03	-2.327E-03	7.882E-03	2.112E-02	3.151E-02
0.260610	-1.011E-02	-9.232E-03	-7.296E-03	2.223E-03	9.965E-03	3.189E-02	3.432E-02
0.275503	-7.504E-03	-7.793E-03	-4.024E-03	5.915E-03	1.843E-02	2.786E-02	3.280E-02
0.290395	3.995E-04	-2.584E-03	3.247E-03	1.249E-02	2.698E-02	3.649E-02	3.331E-02
0.305287	9.863E-03	6.860E-03	1.070E-02	2.332E-02	3.207E-02	3.498E-02	2.801E-02
0.320178	1.638E-02	1.682E-02	2.015E-02	2.666E-02	3.317E-02	3.555E-02	2.659E-02
0.335071	2.180E-02	2.256E-02	2.611E-02	3.468E-02	3.699E-02	3.261E-02	2.617E-02
0.349963	2.689E-02	2.665E-02	3.065E-02	3.728E-02	3.724E-02	2.905E-02	1.924E-02
0.364855	3.108E-02	3.082E-02	3.624E-02	4.149E-02	3.138E-02	2.615E-02	1.465E-02
0.379746	3.432E-02	3.543E-02	4.040E-02	4.466E-02	2.566E-02	1.635E-02	1.067E-02
0.394639	3.931E-02	4.042E-02	4.475E-02	3.522E-02	1.445E-02	1.047E-02	7.457E-03
0.409531	4.225E-02	4.270E-02	3.782E-02	1.957E-02	1.369E-02	6.324E-03	4.968E-03
0.424423	4.070E-02	3.663E-02	1.710E-02	6.382E-03	5.307E-03	3.106E-03	5.243E-03
0.439314	3.123E-02	1.014E-02	2.157E-03	2.495E-03	1.471E-03	9.113E-04	1.169E-03
0.454207	-1.574E-03	-3.003E-03	-8.582E-04	2.563E-04	-1.279E-03	-3.149E-04	-4.591E-04
0.469099	-8.700E-03	-3.557E-03	-2.191E-03	-1.045E-03	-8.997E-04	-7.143E-04	-8.929E-04
0.483991	-6.583E-03	-3.591E-03	-2.029E-03	-1.096E-03	-1.539E-03	-7.145E-04	-1.390E-03
0.498883	-3.272E-03	-2.522E-03	-1.442E-03	-6.178E-04	-1.014E-03	-4.628E-04	-1.131E-03
0.513775	-2.579E-03	-2.375E-03	-1.329E-03	-2.969E-04	-8.776E-04	-3.189E-04	-8.647E-04
0.528667	-2.223E-03	-2.077E-03	-1.097E-03	-1.511E-04	-6.580E-04	-2.734E-04	-9.268E-04
0.543560	-1.446E-03	-1.717E-03	-1.118E-03	-1.576E-04	-7.017E-04	-1.675E-04	-8.053E-04
0.558452	-1.181E-03	-1.798E-03	-1.099E-03	-7.458E-05	-6.505E-04	-1.770E-04	-6.595E-04
0.573343	-1.218E-03	-1.841E-03	-9.838E-04	1.632E-04	-5.453E-04	-1.571E-04	-6.844E-04
0.588235	-8.925E-04	-1.645E-03	-1.137E-03	-1.356E-04	-5.217E-04	-2.726E-05	-5.945E-04

	Velocity Magnitude (divided by tip speed)						
Radial Location (y / D)	Non. Dim. Elevation (x / D):						
	0.006948	0.036359	0.095183	0.182955	0.301065	0.448124	0.687124
0.007446	3.699E-02	3.357E-02	4.742E-02	4.730E-02	9.203E-02	6.342E-02	4.858E-02
0.022338	4.104E-02	5.532E-02	4.330E-02	3.798E-02	3.476E-02	6.150E-02	6.305E-02
0.037230	5.036E-02	3.389E-02	7.307E-02	2.021E-02	2.758E-02	4.734E-02	6.952E-02
0.052123	3.544E-02	2.144E-02	4.970E-02	3.526E-02	4.584E-02	6.956E-02	8.886E-02
0.067014	2.447E-02	2.346E-02	6.927E-02	5.857E-02	5.163E-02	8.538E-02	1.008E-01
0.081906	2.338E-02	3.797E-02	4.810E-02	4.126E-02	5.865E-02	8.739E-02	1.182E-01
0.096798	4.237E-02	3.177E-02	3.919E-02	4.361E-02	6.713E-02	1.266E-01	1.204E-01
0.111691	4.518E-02	4.105E-02	2.144E-02	4.080E-02	6.954E-02	1.024E-01	1.177E-01
0.126582	3.446E-02	3.206E-02	2.594E-02	4.115E-02	2.598E-02	1.346E-01	1.354E-01
0.141474	3.227E-02	3.778E-02	2.225E-02	3.271E-02	6.047E-02	1.021E-01	1.480E-01
0.156366	3.215E-02	3.258E-02	2.192E-02	2.790E-02	6.031E-02	1.033E-01	1.267E-01
0.171259	2.868E-02	2.518E-02	1.477E-02	3.506E-02	6.289E-02	1.159E-01	1.421E-01
0.186151	2.827E-02	3.545E-02	1.539E-02	3.171E-02	7.405E-02	1.149E-01	1.430E-01
0.201042	3.073E-02	2.205E-02	8.534E-03	3.638E-02	7.705E-02	1.210E-01	1.642E-01
0.215934	3.228E-02	1.937E-02	2.190E-02	4.676E-02	9.223E-02	1.528E-01	1.559E-01
0.230827	2.286E-02	1.379E-02	1.453E-02	6.435E-02	8.759E-02	1.507E-01	1.658E-01
0.245719	2.913E-02	1.584E-02	3.027E-02	7.238E-02	1.032E-01	1.529E-01	1.879E-01
0.260610	3.852E-02	6.446E-02	4.392E-02	9.422E-02	1.163E-01	1.459E-01	1.932E-01
0.275503	4.866E-02	4.342E-02	6.602E-02	1.061E-01	1.495E-01	1.758E-01	1.934E-01
0.290395	9.350E-02	7.815E-02	1.101E-01	1.415E-01	1.768E-01	1.991E-01	1.972E-01
0.305287	1.236E-01	1.260E-01	1.377E-01	1.732E-01	1.918E-01	1.950E-01	1.816E-01
0.320178	1.346E-01	1.538E-01	1.663E-01	1.841E-01	1.952E-01	1.984E-01	1.729E-01
0.335071	1.492E-01	1.639E-01	1.832E-01	2.029E-01	2.071E-01	1.887E-01	1.746E-01
0.349963	1.558E-01	1.724E-01	1.942E-01	2.059E-01	2.070E-01	1.846E-01	1.517E-01
0.364855	1.626E-01	1.814E-01	2.052E-01	2.167E-01	1.918E-01	1.742E-01	1.298E-01
0.379746	1.677E-01	1.915E-01	2.144E-01	2.274E-01	1.785E-01	1.360E-01	1.173E-01
0.394639	1.818E-01	2.044E-01	2.239E-01	2.024E-01	1.411E-01	1.151E-01	9.889E-02
0.409531	1.894E-01	2.144E-01	2.130E-01	1.634E-01	1.325E-01	9.360E-02	8.683E-02
0.424423	2.019E-01	2.121E-01	1.618E-01	1.036E-01	9.537E-02	7.345E-02	8.659E-02
0.439314	1.901E-01	1.535E-01	8.572E-02	7.258E-02	6.294E-02	5.848E-02	6.083E-02
0.454207	1.229E-01	6.765E-02	5.555E-02	5.150E-02	3.366E-02	4.280E-02	4.507E-02
0.469099	4.997E-02	3.514E-02	2.827E-02	3.360E-02	3.925E-02	3.276E-02	3.542E-02
0.483991	2.175E-02	1.344E-02	1.955E-02	2.313E-02	2.681E-02	2.944E-02	2.450E-02
0.498883	1.889E-02	2.378E-02	1.827E-02	2.159E-02	2.415E-02	2.570E-02	2.176E-02
0.513775	1.719E-02	1.893E-02	1.754E-02	2.296E-02	2.162E-02	2.689E-02	2.646E-02
0.528667	1.964E-02	1.809E-02	2.590E-02	2.318E-02	2.619E-02	2.626E-02	2.469E-02
0.543560	2.194E-02	2.196E-02	2.200E-02	2.429E-02	2.440E-02	2.805E-02	2.233E-02
0.558452	2.327E-02	2.526E-02	2.092E-02	2.444E-02	2.348E-02	2.824E-02	2.372E-02
0.573343	2.323E-02	2.084E-02	1.945E-02	2.282E-02	2.698E-02	2.804E-02	2.549E-02
0.588235	2.250E-02	2.264E-02	2.040E-02	2.440E-02	2.824E-02	3.003E-02	2.688E-02

	Theta Angle (angle of flow with probe axis), radians						
Radial Location (y / D)	Non. Dim. Elevation (x / D):						
	0.006948	0.036359	0.095183	0.182955	0.301065	0.448124	0.687124
0.007446	1.422E+00	1.392E+00	9.159E-01	7.662E-01	1.589E+00	1.048E+00	1.056E+00
0.022338	1.923E+00	1.267E+00	1.480E+00	1.686E+00	1.472E+00	2.086E+00	1.235E+00
0.037230	1.749E+00	1.584E+00	1.830E+00	1.891E+00	1.964E+00	2.590E+00	1.630E+00
0.052123	1.815E+00	1.572E+00	2.044E+00	1.710E+00	2.294E+00	1.903E+00	1.358E+00
0.067014	1.738E+00	1.831E+00	1.591E+00	1.445E+00	1.743E+00	1.588E+00	1.207E+00
0.081906	1.912E+00	1.883E+00	1.565E+00	1.296E+00	1.668E+00	1.619E+00	1.132E+00
0.096798	1.727E+00	1.770E+00	1.516E+00	1.860E+00	1.336E+00	1.390E+00	1.073E+00
0.111691	2.026E+00	2.210E+00	1.586E+00	1.579E+00	3.977E-01	1.249E+00	1.016E+00
0.126582	1.741E+00	1.418E+00	1.585E+00	1.640E+00	1.656E+00	1.177E+00	7.962E-01
0.141474	1.709E+00	1.432E+00	1.913E+00	1.416E+00	1.784E+00	1.163E+00	7.395E-01
0.156366	1.743E+00	2.217E+00	2.367E+00	1.241E+00	1.529E+00	8.543E-01	7.651E-01
0.171259	1.677E+00	1.571E+00	1.017E+00	1.699E+00	1.399E+00	8.044E-01	6.942E-01
0.186151	1.745E+00	2.023E+00	1.479E+00	1.956E+00	1.209E+00	6.320E-01	6.547E-01
0.201042	2.134E+00	9.766E-01	1.585E+00	1.749E+00	8.999E-01	4.746E-01	5.768E-01
0.215934	1.037E+00	2.286E+00	1.816E+00	1.374E+00	8.555E-01	5.937E-01	5.337E-01
0.230827	1.692E+00	2.340E+00	1.157E+00	1.254E+00	6.840E-01	4.359E-01	4.744E-01
0.245719	1.189E+00	1.939E+00	8.616E-01	9.558E-01	5.293E-01	4.709E-01	4.649E-01
0.260610	7.678E-01	1.212E+00	5.904E-01	6.960E-01	5.030E-01	4.418E-01	4.261E-01
0.275503	6.429E-01	6.895E-01	4.265E-01	5.573E-01	4.301E-01	4.286E-01	4.657E-01
0.290395	5.893E-01	4.628E-01	3.298E-01	5.019E-01	4.336E-01	4.089E-01	4.591E-01
0.305287	4.108E-01	4.459E-01	3.534E-01	4.211E-01	3.846E-01	4.259E-01	4.567E-01
0.320178	3.112E-01	4.190E-01	3.039E-01	4.479E-01	3.868E-01	4.277E-01	4.470E-01
0.335071	3.424E-01	3.146E-01	2.951E-01	4.105E-01	4.166E-01	4.577E-01	4.656E-01
0.349963	3.131E-01	3.087E-01	3.649E-01	3.596E-01	4.538E-01	5.956E-01	5.343E-01
0.364855	3.971E-01	3.303E-01	3.852E-01	3.782E-01	5.012E-01	6.028E-01	5.507E-01
0.379746	4.092E-01	3.606E-01	5.282E-01	4.293E-01	5.298E-01	6.214E-01	5.500E-01
0.394639	5.314E-01	3.819E-01	7.096E-01	5.614E-01	5.954E-01	7.118E-01	6.238E-01
0.409531	8.160E-01	5.351E-01	9.303E-01	5.963E-01	6.298E-01	6.675E-01	6.365E-01
0.424423	2.050E+00	1.087E+00	1.082E+00	7.154E-01	7.518E-01	6.612E-01	6.769E-01
0.439314	1.478E+00	1.857E+00	1.145E+00	7.520E-01	9.427E-01	7.311E-01	7.107E-01
0.454207	1.116E+00	2.591E+00	1.389E+00	8.441E-01	7.479E-01	7.299E-01	6.878E-01
0.469099	1.004E+00	7.030E-01	1.088E+00	5.316E-01	7.046E-01	4.880E-01	6.478E-01
0.483991	9.457E-01	7.892E-01	7.963E-01	6.760E-01	8.609E-01	5.389E-01	4.973E-01
0.498883	9.634E-01	8.674E-01	8.941E-01	7.239E-01	8.569E-01	6.495E-01	4.929E-01
0.513775	9.834E-01	7.593E-01	1.096E+00	7.869E-01	7.498E-01	4.416E-01	6.163E-01
0.528667	8.545E-01	8.549E-01	1.242E+00	7.420E-01	8.039E-01	5.375E-01	5.130E-01
0.543560	1.019E+00	9.974E-01	9.597E-01	7.565E-01	7.971E-01	8.258E-01	6.507E-01
0.558452	4.566E-02	4.956E-02	4.105E-02	8.584E-01	7.387E-01	5.411E-01	6.643E-01
0.573343	4.557E-02	4.089E-02	3.817E-02	8.344E-01	7.001E-01	5.501E-02	6.722E-01
0.588235	4.414E-02	4.442E-02	4.002E-02	4.787E-02	5.541E-02	5.892E-02	5.275E-02